RIGA TECHNICAL UNIVERSITY

Faculty of Power and Electrical Engineering

Institute of Industrial Electronics and Electrical Engineering

Alexander SUZDALENKO

Doctoral student of program "Computerised control of electrical technologies"

Research and Development of Control Means for Intelligent Household Electrical Grids

Doctoral thesis

Scientific supervisor
Dr.sc.ing., professor
Ilya GALKIN

RTU Press

Riga 2013

UDK 621.311(043)
Su 980 r

Suzdalenko A. Research and development of control means for intelligent household electrical grids. Doctoral thesis.–R.: RTU Press, 2013. - 128. pp.

Printed according to the decision of IEE institute on 19 June 2013. Protocol Nr.71.

This work has been supported by the European Social Fund within the project «Support for the implementation of doctoral studies at Riga Technical University».

ISBN 978-9934-507-40-3

Annotation

This doctoral thesis is dedicated to development of control means for intelligent distribution grids, such as contemporary households with installed renewable energy sources. Integration of energy management system allows implementing better functionality, higher efficiency of energy utilization and stability for the end-user.

The main contribution has been made in the field of energy management systems introducing multifunctional interconnection switch with integrated nonintrusive load monitoring algorithm, for which multiple solutions were proposed in order to enable disaggregation of energy generated from renewable energy sources. The algorithm of electrical energy price estimation in an intelligent distribution grid based on load categorization has been described. This algorithm enables long-term power balancing, when local grid operates autonomously, and demand-side management, when it is connected to utility grid. Introduction of DC subgrid has been discussed in order to improve energy efficiency, where bidirectional AC/DC converter based on double half-bridge topology with common neutral point has been proposed as a common point interface converter between AC and DC subgrids. The current sensorless control algorithm with constant switching frequency has been described and tested for rectification, grid-tied and stand-alone inverter modes both for discontinuous and continuous current modes, also defining current limits that could be used for adaptive hysteresis current control algorithm operating at nearly constant switching frequency if the current sensor is used.

The thesis is written in English language on 114 pages, and consists of an introduction, 4 chapters and conclusions, and 8 appendices. 88 figures, 124 formulas, 11 tables, and 91 references are included in the thesis.

Anotācija

Šis darbs ir veltīts viedo tīklu vadības elementu izstrādei, kuras ir domātas, piemēram, modernām mājsaimniecībām, kurās izmanto atjaunojamus enerģijas resursus (AER) . Enerģijas vadības sistēma ļauj sasniegt labāku funkcionalitāti, augstāku enerģijas izmantošanas efektivitāti, elektroenerģijas padeves stabilitāti galalietotājam, kā arī nodrošinās patēriņa pārvaldi tīkla operatoram.

Darba rezultāti ir izmantojami enerģijas vadības sistēmā, piedāvājot izstrādāto daudzfunkcionālo ievadkomutatoru ar integrētu netiešo slodzes monitoringa funkciju, kas tika uzlabota, lai spētu uzskaitīt arī tās enerģijas daudzumu, kas ir iegūta ar AER. Darbā ir piedāvāts ilgtermiņa jaudas balansēšanas algoritms, kura pamatā ir slodžu kategorizācija, ļaujot ieplānot slodžu darbību ar elektroenerģijas cenas regulēšanu. Darbā analizēts līdzstrāvas apakštīkla ieviešanas izdevīgums, lai paaugstinātu energoefektivitāti, tādēļ reversīvais taisngriezis uz dubultā pustilta shēmas bāzes ar kopējo neitrāli ir piedāvāts kā salāgošanas pārveidotājs starp maiņstrāvas un līdzstrāvas apakštīkliem. Darbā tika piedāvāts pustilta shēmas strāvas vadības algoritms bez strāvas mērpārveidotāja, kas ir definēts darbībai taisngrieža, tīklam piesaistītā un autonomā invertora režīmā. Turklāt, ir definēti strāvas līmeņi adaptīvas histerēzes strāvas kontrolei, kas nodrošina gandrīz konstanto pārslēgšanas frekvence, gadījumā ja vadības sistēmā tiek izmantots strāvas mērpārveidotājs.

Promocijas darbs ir uzrakstīts angļu valodā, satur 88 attēlus un ilustrācijas, 11 tabulas, 124 formulas, 8 pielikumus, un tajā ir izmantots 91 informācijas avots. Darba kopējais apjoms ir 114 lappuses.

Acknowledgements

I thank all colleagues from the Institute of Industrial Electronics of RTU for their support during all period of my doctoral studies, especially, my scientific supervisor professor Ilya Galkin, who inspired me in everything that I have done.

Development of this thesis was promoted by an internship opportunity provided by principal research fellow Dmitri Vinnikov from Tallinn University of Technology, where I met good friends of mine Oleksandr Husev, Andrii Chub, and Vasco Miguel Delgado Gomes, to whom I am very thankful for their comments and suggestions. I also appreciate the friendly atmosphere held in TTU that could not be possible without Irena Milashevski, Anna Andrijanovich, Janis Zakis, Anton Rassylkin, Victor Beldjajev, and Serhii Stepenko.

I express sincere appreciation to my parents, who provided me with an opportunity to study for such a long period, taking care of household on their own, when various deadlines approached, and who also financially supported me at some moments.

My deepest love and heartfelt gratitude are devoted to my wife Vera and daughter Vasilisa – two lovely girls, who make my mood elated whenever I think about them. I admire Vera's time planning talent that allowed me spending whole days developing present thesis, while she was taking care of the child and writing her own thesis.

Contents

INTRODUCTION

In this chapter the background and the motivation of the work are explained, starting with the current status of intelligent distribution grids, covering European policies concerning the use of renewable energy sources. The main hypothesis and objectives of present thesis are outlined and scientific and practical novelties are stated at the end of the present chapter.

Background

Energy is a key resource that allows humanity to evolve successfully during centuries, generating power or being transformed to another form of energy used in everyday life activities. On the other hand, existing energy delivery process causes global changes - mining activities change the landscapes, refining of crude oil produces pollutants released into the atmosphere, water and land, and combustion of fossil fuel impacts Earth climate due to CO_2 emissions.

Technological development enabled utilisation of new energy forms – Solar energy was the first, which was used indirectly by growing plants and heating, before magnifying glasses were first used in the 3rd century B.C. to light up torches, while Photovoltaic effect that transformed solar energy directly into electricity was discovered only in 1917th. Biomass combustion was widely used as a heat energy source before the steam engine was patented by James Watt. This technology provided a possibility for continuous rotative motion from heat energy in the middle of 1700's, which initiated the industrial revolution in the 18th century. The rotating motion was used as traction force for locomotives and ships. Also steam engine was used at the first electric power plant after Michal Faraday defined the fundamental principles of electricity generation in 1820's. In 1821, Thomas Johan Seebeck discovered thermoelectrical effect producing electric current when dissimilar metals were exposed to a temperature gradient, and transforming heat energy into electricity. Wind power allowed passing long distances over the seas being applied as traction force for ships, however, it was also widely used on-shore for transforming wind energy into rotating motion in water pumping or milling. The first electric wind turbine was designed in 1887 by James Blyth in Marykirk, Scotland. Electrical energy is valuable form of energy due its simple transmission and

distribution principles as well as easy transformation into any other forms of energy, which promoted its worldwide utilization.

The world's electrical energy demand is growing at a rate of 2.4% annually, while developing countries have 4% increase of demand [1] due to increasing population [2] and standards of living, forcing countries to install new generation facilities on a regular base. While the consumption of fossil resources remains reasonable, countries invest finances into development of renewable energy sector. The total investment volume is estimated was 257 billions of USA dollars in 2011[3]. The result of these investments is a growing number of installed solar and wind energy capacities per annum (see Fig.I.1), promoting significant reduction of technology costs. For instance, energy producing costs in Germany is 0.138-0.163€/kWh for photo-voltaics (PV) plants [4]. New hydropower plants are also introduced yearly, especially in Africa and Asia, where a lot of undeveloped resources are still available [5].

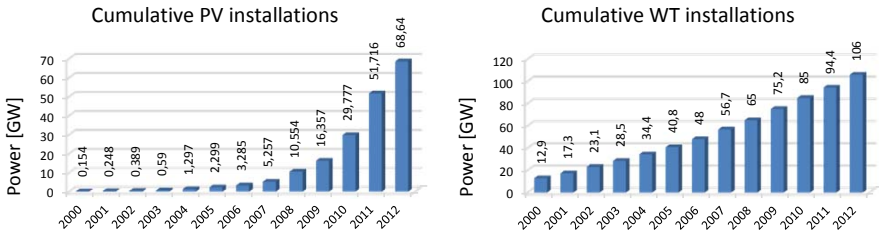

Fig. I.1. European cumulative PV and WT installations [6][7]

In order to promote RES utilization in residential sector countries might need to adapt their legislation concerning connection of small energy sources to the utility grids, so that the owners of the RES become prosumers (producer and consumer). Denmark shows a spectacular example of this approach, where 36 MW of PV panels are connected monthly to a grid in the residential sector, after it became allowed to "store" energy in public grid surplus consumption, thus helping to reach the 20-20-20 governmental goal of 200 MW PV capacity by the end of 2012 [8].

Various concepts are developed for modernization of electricity distribution grids. Smart-grid [9] is focused on enabling communication between all participants of electrical energy delivery and consumption process. A control function would allow controlling demand and generation curves, utilizing renewable energy sources, and would provide operation at most optimum point.

Microgrid concept (a local grid, with total power up to several hundreds of kW) [10] also provides superior operation for end-users. It is focused on utilization of distributed energy sources (mostly renewable like solar plants, wind parks, but also fossil fuels, like microturbines) proposing utilization of higher efficiency energy (electrical and thermal) in the delivery process, as it eliminates use of long transmission lines from the electrical plant to the end-user. It also delivers the idea of islanded operation, as by controlling locally available energy sources it is possible to disconnect from outer (utility) grid either due to its unacceptable quality or to too high price of electrical energy.

Another concept is smaller by scale and proposes the idea of controlling contemporary household appliances (up to several tens of kW) [11]. It is mentioned in [12] that such a system should consist of mixture of RESs capable to supply at least net required energy, storage elements for energy balancing, and should have a capability to operate in islanded mode. Consequently, such a system could eliminate most of the outer grid's problems.

Project motivations

Electrical energy consumed in residential sector accounts for about a fourth part of global electricity market in worldwide scale. European households consume 28.6% of totally generated electricity [13]. The demand curve of this sector is highly uneven due to people absence from home during working hours and inactivity during night period. Two basic load peaks during morning and evening hours overlap with demand curves of industrial and commercial sectors, the result of which compiles the peak load of the day [14]. This problem leads to under-utilization of generation capacities, for instance, 20% of USA generation plants operate during 5% of the total time [15], which leads to rise of operation cost.

Demand-side management [16]-[17] is one of the solutions that helps to form residential demand curve. It is based either on electricity tariffs, agreements, real-time electricity price information delivery to the end-user, or in some cases – on government policies that mitigate peak demand. Features of intelligent distribution grid (IDG) allow implementation of even more flexible demand management, as IDG behaves as controllable load by using internal energy resources, shedding loads, or generating energy to the utility grid.

Considering Denmark experience on popularity of PV panel installation at the end-user side it can be assumed that other countries could take over Danish practice on integration of RES application in residential sector into the power grid, thus increasing the installed RES capacity in worldwide scale. On the other hand, high penetration of renewable energy sources raised discussions about grid stability issues, advising to implement virtual inertia for grid-tied inverters and small energy storages for smoothing energy generation [18].

The prevalence of small renewable energy sources and energy storages in households has opened discussions on DC subgrid installation[19], [20], [21], [22] as most of the loads, renewable energy sources, and storages are in fact DC elements that accordingly to [23] allow saving up to 15% by reduction the number of unnecessary energy conversions.

Moreover, energy efficiency issues can be promoted by providing detailed energy consumption data to the end-user. Pilot projects described in[24][25], and [26]show that energy reduction by 5-15% is achievable due to provided so-called "real time plus" information about user's consumption pattern, with energy data divided according to consumption by separate electrical appliances. As a result, the various changes in energy saving behaviour could develop: 1) changes in habits and daily routines; 2) low-cost stackholding (inefficient lamps replacement); 3) money investment in more efficient electrical devices, materials, etc.

Proposed ideas raise the necessity for energy management system capable of controlling local electrical appliances and located in each household. Thus, the demand-side management is realized by changing the consumption pattern upon the request from utility grid operator or when operated in islanded mode, where the power balance between sources and loads should be kept. The detailed feedback on consumed energy would promote energy efficiency.

Main hypothesis and objectives

Hypothesis

1. Non-intrusive load monitoring function can be implemented by means of proposed interconnection switch.

2. Use of load surface, which represents load categorization based on time-triggering, price triggering, and price-responsive load scheduling, enables predictive control of long-term energy management.
3. Single-phase half-bridge based bidirectional AC/DC converter driven by special current control algorithms allows eliminating instantaneous measurement of inductor current.

Objectives

1. To develop a multifunctional interconnection switch with integrated non-intrusive load monitoring functionality, which enables RES generated energy disaggregation.
2. To develop a communication node capable to control electrical appliances of the intelligent distribution grid.
3. To analyse the existing instantaneous, short-term, and long-term power balancing algorithms and to improve them, enabling superior operation of intelligent distribution grid.
4. To define the current control algorithms for bidirectional AC/DC converter that would allow its operation in rectification, grid-tied, and stand-alone inverter modes.

Means and methods of research

Mathcad software was used in order to accelerate mathematical calculations and to visualise the obtained functions. The simulations of power electronic schemes were carried out in PSIM software, where verification of the obtained analytical control functions for proposed bidirectional converter was made. LabVIEW software was used to verify electric price estimation algorithm, as well as to control Lambda DC laboratory power supply block in order to implement automated tests. Quartus Web Edition and Code Composer Studio were used to develop application firmware for FPGA and DSP based control boards correspondingly, and appropriate built-in debugging tools were used during optimization processes. PCB design was made using OrCAD software pack.

Electrical circuit theory was applied in order to obtain mathematical model of power electronic converter. Bisection method was used as a numerical approach for transcendental equation root estimation.

Scientific novelties

1. Algorithm for electrical energy price estimation in intelligent grid applications based on load categorization, which provides the result in two steps, is developed.
2. The constant switching current control technique is defined for active rectifier based on half-bridge topology for rectification, grid-tied, and stand-alone inverter modes operating in discontinuous and continuous input of inductor current modes.
3. The current limits for adaptive hysteresis current control are defined in order to provide nearly constant switching frequency operating in rectification and grid-tied inverter modes.

Practical novelties

1. The multifunctional interconnection switch with non-intrusive load monitoring functionality is developed for intelligent grid applications.
2. Transformerless bidirectional AC/DC converter based on double half-bridge topology with common neutral point is proposed as a common point interface converter.
3. The FPGA control board is developed that is pin-to-pin compatible with Piccolo LaunchPad development board from TI, which can be used in advanced course of Digital Electronics for electrical engineers.

Practical application of the work

Proposed bidirectional interface converter together with multifunctional interconnection switch can be redesigned for market-ready solutions targeted for unsaturated niche of energy management means. Small-scale intelligent grids such as contemporary households with installed renewable energy sources can be considered as a typical application for the mentioned devices.

1 FUNCTIONAL DESCRIPTION OF IDG

Intelligent distribution grid (IDG) consists of various home appliances connected to the electricity grid, which are controlled by means of communication hardware, enabling remote control or data transfer to the Energy Management System (EMS). This configuration enables superior functionality of household grid by interacting with network operator as controllable load.

1.1 IDG supply scheme

These grids can be divided into three types depending on supply scheme topology: AC-based, DC-based or hybrid IDG.

- AC-based IDG can be implemented by using a simple AC network, integrating AC loads into a single controllable intelligent grid by enabling communication functions between the grid elements. This grid is connected to the utility grid through an interconnection switch, which is controlled by EMS, choosing either to work in an islanded or a grid-connected mode depending on the grid's energy quality, electricity price, and other factors.
- DC-based intelligent distribution grid. Implementation of DC power supply has many advantages considering the rapidly increasing number of installed privately owned renewable energy sources, as all of RES are DC sources or have a DC link inside the converter. Also, many loads are in fact DC [19]. Thus, DC power supply scheme allows reaching higher efficiency by eliminating unnecessary power conversions. The mentioned DC grid is connected to the utility grid through a bidirectional AC/DC converter and acts as an interconnection switch. It controls energy import or export depending on energy lack or excess in the local grid. Such a topology provides an easy operation as AC/DC converter can operate in a dynamic way, switching from energy export to energy import. It does not need to be resynchronized after disconnection from the utility grid, as it just catches the grid's frequency.
- Hybrid intelligent distribution grid combines the benefits of both previous topologies as it allows utilizing traditional AC loads, as well as provides

simple connection of RES and energy storages to DC distribution system, eliminating unnecessary energy conversions. This IDG contains separate interconnection switch and bidirectional AC/DC converter, which regulates the power flow in case of grid-connected mode, but in case of islanding it operates as an uninterruptable power supply (UPS), supplying energy for AC loads in the local grid. Thus, this topology provides the most sustainable power supply scheme for contemporary households. However, resynchronization procedure is necessary to be implemented in such a topology, as in case of islanded operation, when AC-load is supplied by bidirectional rectifier, the interconnection switch should provide data for internal inverters to catch the utility grid's frequency.

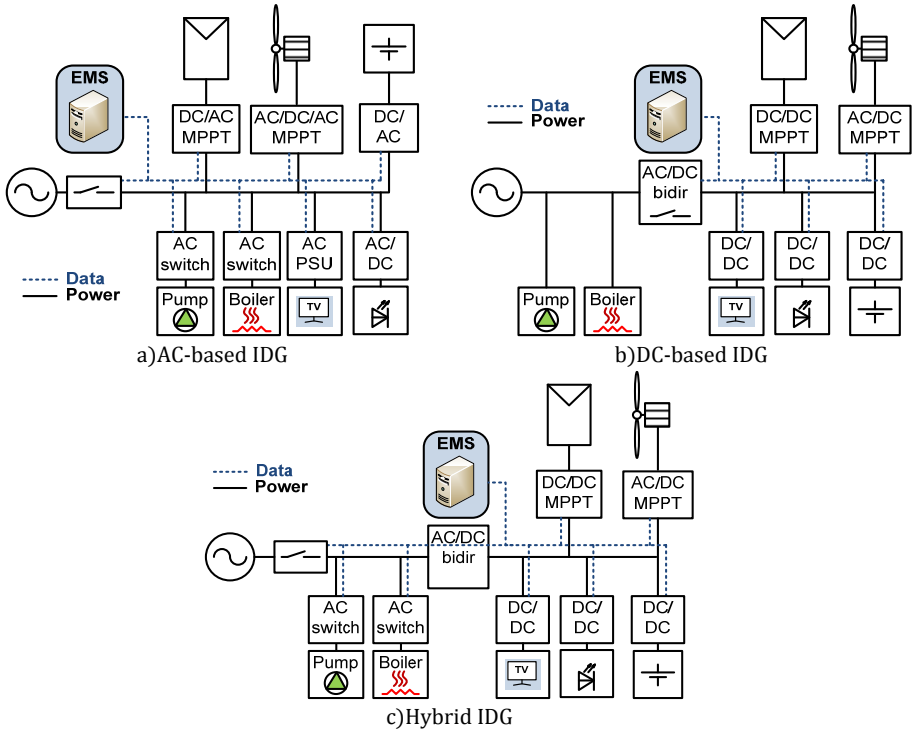

Fig. 1.1. IDG supply topologies

As it is shown in the Fig. 1.1, the IDG consists of intelligent loads, non-intelligent loads that are controlled by means of AC switch or a module for connection of non-intelligent loads, controllable sources and storages, interconnection switch, which determines the border of intelligent grid, and EMS that controls the operation of intelligent grid.

1.2 EMS control topology

Energy management system is responsible for short-term and long-term energy management procedures. It provides data for the local grid about the electricity price and weather forecast and predicts the amount of power generated by RES for the nearest future (hours, days) [27]. It also should be able to aggregate data from intelligent loads. This data is used to find the optimal price for electricity when operating in islanded mode and keeping power balance in short-term perspective.

In [28] various control topologies of EMS are described. The first one is a centralized topology, which is based on a single controller, which controls operation of each source and load in real time. This is not a widely utilized approach as it has some major drawbacks like a weak reliability due to malfunction of either controller or communication link that can cause malfunction of the whole grid. Separate controllers for each grid element are used in the decentralised approach. The control function is static and it is based on local measurements of DC bus voltage or AC grid voltage and frequency. Since there is no communication between grid elements, it is not possible to implement any dynamic system with load scheduling, shedding, and prioritizing.

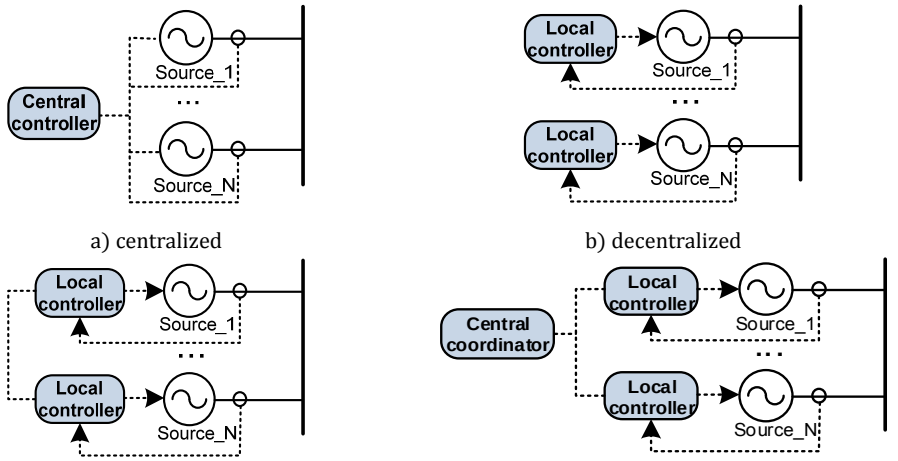

Fig. 1.2. EMS control topologies

Distributed control approach is based on local controllers for each element as in the previous case, but with enabled communication between them. Thus, the coordination of operation modes of different grid elements is possible, for example, storage element can start to discharge in case if RES controller works at MPPT for

stabilizing the output power. However, this approach is limited by static control function, which is embedded into controllers of each of the sources, limiting flexibility of the system.

The last two approaches are combined into hybrid control topologies. First of them, called hybrid central control topology uses local controllers for instantaneous power balancing and utilizes central controller, which is connected to each grid element, via communication link. In such a way the central controller operates as a coordinator, which allows updating reference points of each of the sources

The last of the defined control topologies is a hybrid distributed control approach based on local controllers. It is the most reliable control approach for sources and communication and is carried over power lines. Such an approach eliminates the need for additional communication media and operates without central EMS controller. It was advised in [28] to use either PLC communication or DC bus signalling (as DC bus supposed to be central core of a nano-grid) for coordination of the grid element functions.

Table 1.1

Comparison of control topologies

Topology	Advantages	Disadvantages
Centralized	Best control	Hard to enlarge grid, poor reliability
Decentralized	Simple, no communication link	No possibility of configuration
Distributed	Improved reliability	Limited to communication infrastructure capabilities
Hybrid Centralized	Good performance at reduced cost	Depends on central coordinator and communication link

Although multiple topologies are presented here, hardly any of them suits for control of intelligent grid (see Table 1.1). Besides, some previously not considered remarks should be made to the above described topologies. The authors in [28] have not mentioned a protection system regarding hybrid distributed control topology, which may disconnect the source from the main DC bus, disabling the communication. Such a situation is unacceptable since the source controller will not have a possibility to communicate with other grid elements in order to notify about the type of malfunction. Another clarification should be made regarding the communication link. The two

topologies (distributed and hybrid distributed) differ only with the communication link, which in case of distributed control is external, but in the second case is a power line carrier, which is another form of communication media, but not an absence of communication link as it was mentioned in [28].

The author supposes that the communication infrastructure should also be considered when the distributed energy management systems are built. In most cases communication infrastructure utilizes a central node (router in Ethernet network [29], coordinator in ZigBee network [30] and in power line communication network based on Y-Net protocol [31]), which holds the routing table or provides other nodes with addresses for successful communication. In other words, distributed control systems in most cases are based on centralized communication infrastructure. Consequently, malfunction of the central node of the communication infrastructure will disable distributed functionality of energy management system.

1.3 Contribution to control means

The author's contribution in the field of control means is stated below:

- Definition of pure distributed control topology, which eliminates the use of central unit in the communication infrastructure.
- Development of versatile interconnection switch that provides disconnection and reconnection functionality and allows solving single-phase problems on utility grid side by supplying critical loads from healthy phases, as well as combining multiple local single-phase sources to supply load, which is higher than the nominal power of a separate source.
- Development of module for connection of non-intelligent load that provides remote control of non-intelligent electrical appliance.

1.3.1 Control topology

Basically, there are two main topologies for implementation an energy management system – a centralized one (like the hybrid central topology described in [28] or in [32]), which utilizes local controllers for instantaneous power balancing, and a central controller, which coordinates operation of all grid elements over a

communication link (wireless or wired). The distributed energy management system does not use a central controller. Instead, each grid element communicates with the others either by broadcasting information over a communication media or communicating peer to peer by using physical addresses of the other nodes. Development of distributed control system also influences the choice of the communication infrastructure, which should be able to communicate without a central node, for instance, MAC addresses can be used to communicate in Ethernet local network or a Serial Number in Y-Net based network.

Centralized EMS

Central controller of such a control topology holds the following functionality:

- Acquires primary data from remote nodes and defines their operation schedule of based on the history of operation for a certain node;
- Defines the price function based on difference between load predicted patterns and generation patterns (weather forecast is used for RES);
- Controls operation of loads – shifting, shedding, and scheduling;
- Sets variable set points for interface converters;

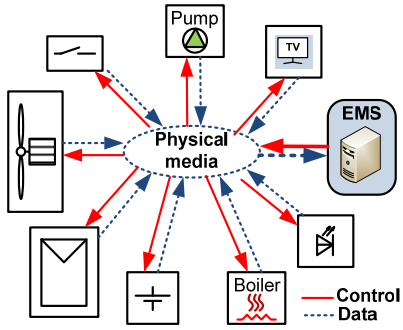

Fig. 1.3. Data and control command flow directions in centralized EMS

After connection to the grid each node provides information to the EMS, which registers the end-device and controls it in the future.

Distributed EMS

In this case the functionality of the intelligent grid is divided between its elements.

- Each intelligent load provides its own schedule of operation, based on history of operation stored in the local memory;
- Sheddable loads are controlled by the other higher priority loads, which are going to connect to the grid;

Proposed distributed system still has a central node, which holds functionality of SCADA system, which, in turn, monitors and stores parameters and provides information to the grid, for instance, weather forecast. By default, the central node defines electrical energy price function for the local grid, but this function is also realized on the other grid nodes (energy source nodes are best suited for this) as the distributed system should not rely on one node only.

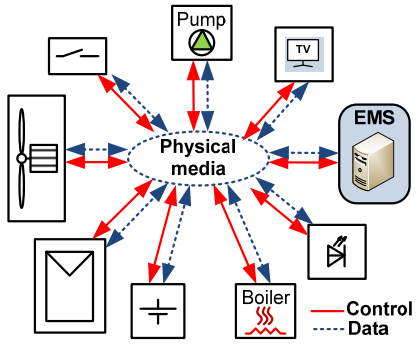

Fig. 1.4. Data and control command flow directions in distributed EMS

At the moment of first connection, each node provides short information about itself by broadcasting information into the network. Each node holds a local copy of unique address of the other nodes to communicate with, implementing distributed communication capability.

Choice of communication hardware

There are various proposals for using communication devices of different vendors to create an intelligent grid. Echelon company proposes Smart Transceivers [33] to build control system over power lines. The nodes provide the highest functionality layer of OSI reference model using so called network variables. The grid is configured by a special software tool, in which various nodes are interrelated for exchanging the information by means of network variables. Then the system operates in autonomous way, however, connection of an additional node will require configuration of the actual

node. Although, company offers PL3170 with a self-initializing function, it has restrictions on a number of self-configuring nodes, consequently, missing Plug'n Play characteristics[34].

HomePlug C&C standard is specially delivered for energy management in smart homes with communication link over power lines [35]. Yitran's powerline transceiver IT800 was selected for this standard as a baseline technology due to its reliable communication and high functionality. This integrated circuit by default is used as a modem, which holds functionality of 4 layers of OSI reference model, meaning that it is responsible for delivery of the information to other network nodes, while host microcontroller is holds the application firmware. Another operation mode of this transceiver is transparent bridge, when data transmitted to the modem are directly transmitted to power line and vice versa. This can be used in some special applications at a price of reduced functionality – the transport and network layers are disabled. Finally, Yitran provides so called open architecture – whole documentation for this chip, which can be reprogrammed and used as a single device, as basically it is a microcontroller with special peripheral modules.

This modem implements centralized communication networking as in default configuration it implements communication link with the coordinator node. The author proposes using the same transceiver to create a distributed control system as it also allows communicating by using Intrernetworking Unicast service delivering data packets to the destination node by its serial number – unique for each node, providing a possibility to communicate without involving the coordinator.

Choice of EMS platform

Personal computer (PC) is chosen as a central node of EMS. It is connected to Jace2 device using it as interface converter. Jace is communicates with touchpad panel implementing human machine interface. PLC modem based on Yitran's IT800 chip is used to communicate with other network nodes [36].

The control board, which is designed for tests of both control topologies, is shown in the picture below.

Fig. 1.5. EMS control board for IDG

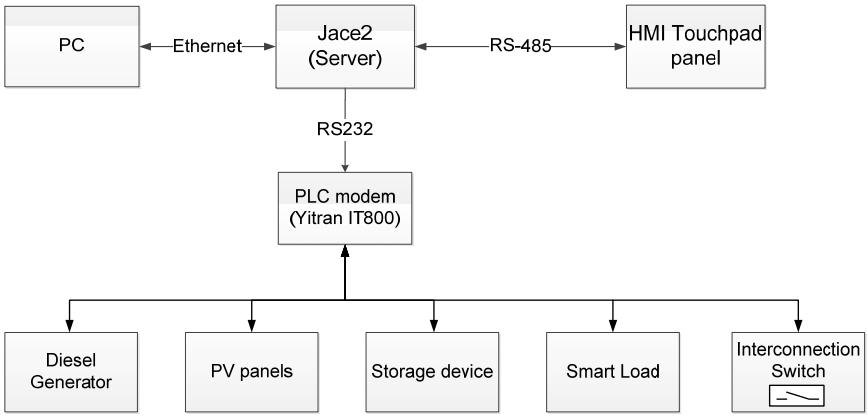

Fig. 1.6. Communication topology of EMS control board

The corresponding functionality of the intelligent grid is realized in SCADA (Supervisor Control and Data Acquisition System) running on PC. It is responsible for data storage, analysis, and forecasting load operation and control in case of centralised EMS topology. In case of distributed EMS topology SCADA implements only data storage and visualization, as the load scheduling is provided by the nodes themselves, but the control function is distributed between intelligent grid elements.

1.3.2 Multifunctional Interconnection Switch

In case of 4 or 5 wire power supply systems, which are typical for rural households, the loads are spread between 3 phases, but RES may be connected via single-phase inverters to separate phases. Considering that in case of an islanded mode RES would only be able to supply loads on the same phase loosing opportunity to interact in conjunction to supply the load, which is greater than single RES maximal output power. Thus, special equipment should be utilized to solve this problem.

Analysis of the market

The simplest solution of implementing an interconnection switch is to use a power contactor, which is rather reliable, low cost, and with nearly zero power consumption. On the other hand, it inherits delays due to its moving parts, which disables accurate control, for instance, reconnection at a zero-voltage crossing point; another disadvantage is that it is not able to control the contacts separately.

The semiconductor based interconnection switch is described in [37], consisted of 3 switches and voltage sensors on both sides, and a communication module for controlling local energy sources by providing voltage and frequency deviation data, in other words, controlling the resynchronization procedure. However, the idea of individual switch control, which would allow separate phase disconnection , for example in case of a single phase problems, enabling to supply critical loads connected to healthy phases, is not discussed there.

ABB company has announced a new family of circuit breakers with power monitoring functionality [38], which eliminates the usage of additional measuring devices, however, they are rated for high power grid management and are not directly suitable for household applications.

In order to promote effective energy utilization the non-intrusive load monitoring (NILM) device is used. It was first mentioned by Gearge W. Hart in 1983 [39]. His idea was based on monitoring of active and reactive power changes from the point of common coupling to enable energy disaggregation by separate electrical appliances. This approach allows creating reports on consumed energy data. Obtained feedback influences owner's behaviour, motivating him to use more energy efficient devices. As a result 5-15% of energy efficiency increase is achievable [24][25].

Functionality of hardware used for connection with utility grid is listed below:

- measurement of outer and local grid voltages and frequencies, providing these data to local power sources that control the resynchronization procedure.
- Phase commutation according to voltage, phase, and frequency deviation limits.
- Phase interconnection in a local grid, which is used for solving one or two phase problems in the outer grid, as well as combination of local single-phase inverters connected to different phases in order to supply higher load.
- Non-intrusive load monitoring (NILM) that allows creating reports with consumed energy disaggregated by electrical appliances.

It is possible to implement the above described functionality with the three devices available on the market: contactor with voltage measurements from both sides, phase selector, and NILM device. The connection scheme is shown in the figure below (Fig. 1.7).

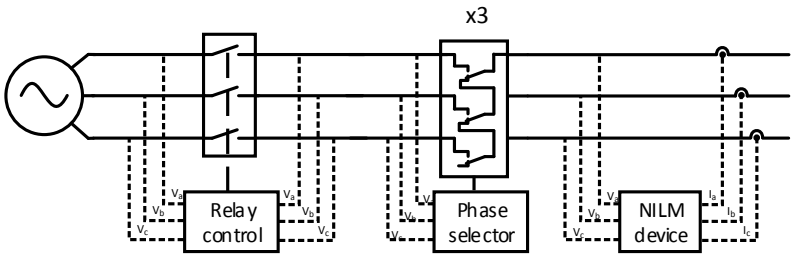

Fig. 1.7 Simplified scheme of devices needed for required functionality

Proposed multifunctional interconnection switch

The author proposes to use multifunctional interconnection switch (IS)[40], which consists of additional phase interconnection switches based on combined semiconductor and mechanical switches. The separate control of all switches enables solution of single phase problems from the utility grid side by disconnecting only one faulty phase and continuing to supply loads by connecting them to healthy phases. Additionally, phase interconnection switches allow combining single phase inverters connected to different phases during islanding or phase-interconnection mode in order to provide supply of critical loads (such as water supply, heating, lighting, etc.)

connected to different phases. The hardware used in the proposed multifunctional IS also allows implementation of non-intrusive load monitoring, as a result the three market devices are replaced by one.

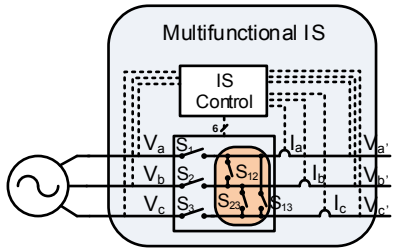

Fig. 1.8. Simplified scheme of proposed multifunctional IS

Problem definition and possible solutions

The load disaggregation algorithms have been developed since the first cluster approach implementing more detailed current and voltage sampling realizing harmonic analysis [41][42][43], current transients analysis [44]. Modern programming approaches were also used for data analysis, for example fuzzy logic [45], integer programming [46], dynamic programming [47], and genetic algorithms [48].

Considering the modern trends, many households are getting equipped with local electrical energy generators producing energy mainly from renewable energy sources – wind and solar energy, some also have energy storage devices installed. The load disaggregation process in such conditions is difficult as loads and sources make action and counter action, disabling proper identification of consumed amount of energy. For this reason additional equipment and special analysis are considered to be used:

1. Use of meteorological sensors;
2. Use of an additional current sensor;
3. An analysis based on spectral pattern changes.

In the first solution additional sensors may be installed to monitor solar radiation and wind velocity. In this case it is possible to use the NILM controller to correlate electrical energy consumption changes with the data provided from the sensor and to extract generated energy from loads, which are variable in time. In this case special firmware should be used for the NILM device and additional inputs are required for connection of meteorological sensors.

The next approach is based on the assumption that electrical energy distribution boxes are localized where all appliances are divided in groups and connected to different circuit breakers, and different energy sources may be connected through separate circuit breakers that allow sensing generated current separately from consumption current. In this case an additional current sensor is to be used and as a result load variable in time could be identified more precisely.

In the third solution it is considered that the RES is always interfaced with a power electronic converter, which has a specific "spectral envelope" - a special content of information about active and reactive power and a harmonic content of an appliance. By using this method the NILM device could identify the amount of energy generated by the RES by analysing total consumption and harmonic pattern changes in time. If the harmonic pattern of a power converter is known, then the amount of generated energy could be disaggregated from the total consumption, thus the load variable in time should not be mismatched. This solution, however, requires significant computational resources, as it requires not only calculation and analysis of active power, but also spectrum analysis of measured waveforms.

Description of proposed interconnection switch

Multifunctional interconnection switch (IS), which consists of 3 phase commutation and 3 phase interconnection combined (mechanical and semiconductor) switches, is proposed for intelligent grid applications (IGA) that implement NILM functionality (see Appendix D). The voltage and current sensing is implemented by means of MAX1032 and ACS712ELCTR-20A integrated circuits (IC), correspondingly. The ADC from Maxim Integrated allows bipolar sensing from single power supply, provides voltage level translation for digital interface and sampling up to 115 ksps. The current sensing IC uses Hall effect providing galvanic isolation up to 2.1 kVrms with 50 kHz bandwidth. The application algorithm is implemented on Stellaris LaunchPad provided by Texas Instruments. Additional sensors are connected either by using RS232 ports or using free digital inputs on Stellaris Launchpad.

Table 1.2

Comparison of hardware used in multifunctional IS and market devices

	Input contactor	Phase selector	NILM device	Proposed IS
Switching performance	0,2 s	-	-	0,01 s
Switching performance	-	0,2 s	-	0,01 s
Relay number	3	3x3	-	6
Voltage sensors	6	3x3	3	6
Current sensors	-	-	3	3

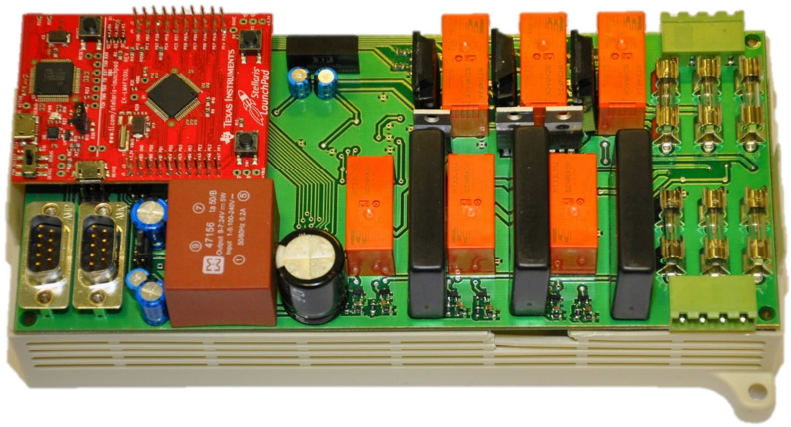

Fig. 1.9. A photo of the proposed interconnection switch

1.3.3 Module for connection of non-intelligent load

Many of household appliances are automated by means of a local sensor, which monitors working parameters (temperature, pressure, illumination level) and controls it with hysteresis loop at a desired level. Thus, it is necessary to develop a special module for connection of non-intelligent load (controllable AC switch), which allows communicating with and controlling the non-intelligent appliance, enabling such functions for EMS as load shedding and scheduling. It consists of two switches – normally closed for disabling of switching on of electrical appliance, S_2 – for switching on. It also uses a communication modem for data transfer; ADC for performance of measurements, and microcontroller for running the application code.

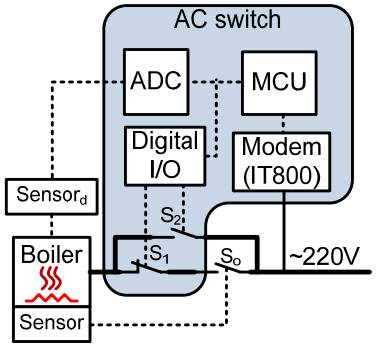

Fig. 1.10. Configuration of AC switch.

Description of proposed communication node

In order to manage IDG using Yitran communication modules two types of devices should be used: interface and protocol bridge between the end device and Yitran communication module, and second device, which would control non-intelligent end device by means of relays and digital inputs and outputs.

The first prototype was build in order to develop the communication node for controlling the non-intelligent end-device and enabled data transfer via Yitran module (see Fig. 1.11), containing MSP430F2132 microcontroller, 4 digital inputs and 8 outputs, electronic relay output and RS232 communication interface that is optimized for minimal energy consumption [49].

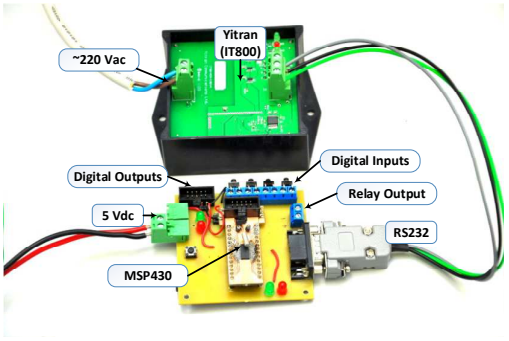

Fig. 1.11. Prototype of communication node

The proposed versatile communication node combines functionality of both IDG controlling devices as it has two communication ports that enable its operation as an interface converter (see Fig. 1.12 and Appendix E). In order to control various non-intelligent end-devices the following is considered: 4 relays with NO/NC contacts, 16 digital configurable inputs/outputs , 8 analogue inputs, 2 analogue outputs, an isolated power supply.

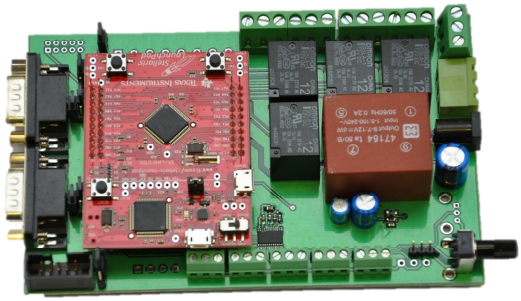

Fig. 1.12. A photo of the developed communication node

1.4 Summary

In this chapter the following has been obtained:

1. It is reasonable to implement DC subgrid inside the IDG as many of RES by fact are DC sources or contain DC link, as well as many of loads operate from DC current, thus, introduction of DC subgrid leads to increased energy efficiency as it reduces energy conversion count.
2. Described communication topology of EMS is versatile and Plug'n'Play type for simplification of IDG expansion, where the hybrid centralized control topology is considered to be the best one, since it provides a versatile operation of the whole grid as local controllers provide stable control of end-devices, while central coordinator is used only for long-term scheduling.
3. Proposed interconnection switch is responsible for grid voltage monitoring, disconnection, and resynchronization procedure providing voltage and frequency deviation data to the local energy sources and phase interconnection in order to supply critical loads if one phase problems occur in the utility grid. It also implements NILM functionality or energy data disaggregation by electrical appliances that accordingly to researches has potential to impact the end-user's day-to-day behaviour, which leads to energy consumption reduction from 5 till 15%.
4. Versatile communication node implements functionality of interface and protocol converter between the end-device and EMS and is capable of controlling non-intelligent loads by means of integrated relay outputs, digital and analogue inputs and outputs.

2 POWER BALANCING IN IDG

Currently a major effort is focused on solutions that keep an energy balance in small-scale networks, such as nanogrids[28][12] and microgrids[50]. The following chapter discusses the energy balancing approaches and contributes to their improvement.

2.1 Overview of power balancing techniques

Energy management approaches are divided into groups, which differ by the period of management: instantaneous (real-time) energy management, where balance is kept in a period of milliseconds or seconds, short-term energy management, with periods of seconds or minutes, and long-term energy management, which defines energy management strategy to fulfil objectives for longer periods such as hours, weeks, or months.

2.1.1 Instantaneous power balancing approach

Operation in an islanded mode requires special control technique for energy generation units, which ensures balance between output power of generator and a demand of the local grid. For this reason the droop control approach is mostly applied both in AC and in DC power distribution grids, where it defines the method of power sharing between various energy sources by means of definition of different droops accordingly to their nominal power [51].

The droop control differs between AC and DC grids, because in a DC grid only supply bus voltage should be regulated, but in an AC grid – both voltage and frequency.

Droop control in AC grid

The droop control method for AC grid is described by two equations below:

$$E_{AC} = E_{AC}^{*} - k_E \cdot (Q - Q^{*}), \quad (2.1)$$

$$\omega_{AC} = \omega_{AC}^{*} - k_\omega \cdot (P - P^{*}), \quad (2.2)$$

where

E_{AC}, ω_{AC} – reference values for converter;

$_{-}^{*}$ - nominal values;

k_E, k_ω – coefficients;

P, Q – measured active and reactive values.

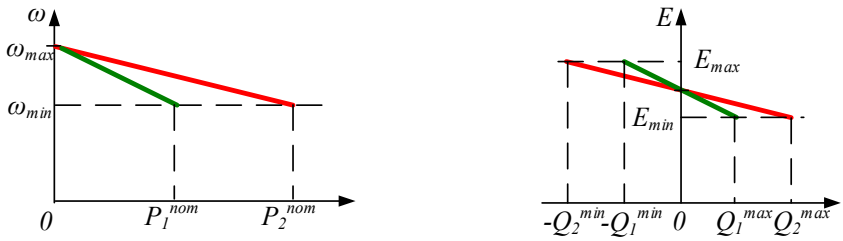

Fig. 2.1. E/ω-droop control for AC grid

P_k^{nom} – nominal active power of source k,ω_{max}, ω_{min} - maximal/minimal reference angular speed,Q_k^{max}, Q_k^{min} – maximal/minimal reactive power of source k, E_{max}, E_{min} - maximal/minimal reference voltage

AC droop control is performed in the following way – the amount of active power is associated to the frequency, but reactive power with voltage reference (see Fig. 2.1). When a generator's output power becomes more capacitive, it increases the voltage reference, which, in turn, increases the output power of the generator decreasing the output frequency at the same time, thus sharing power with the other generators.

Droop control in DC grid

In case of DC grid the control is simpler as only DC bus voltage needs to be controlled, where DC voltage is associated to converter's nominal power. Mathematically it is described as follows:

$$V_{DC} = V_{DC}^* - R_{virt} \cdot I_{DC}, \tag{2.3}$$

where

V_{DC} – reference value for converter;

$_{-}^{*}$ - nominal values;

$R_{virt} = \frac{V_{DC}^* - V_{min}}{I_{max}}$ – virtual impedance;

I_{DC} – measured current value.

Graphical representation of droop control for DC grids is shown in the Fig. 2.2.

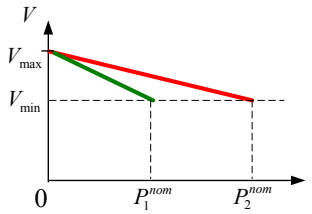

Fig. 2.2. V-droop for DC grids

V_{max}, V_{min} - maximal/minimal reference voltage of DC grid, P_k^{nom} – nominal active power of source k

From the energy management point of view, DC distribution grids deliver less problems as the only single parameter should be regulated within the defined levels. In contrast, energy management in an AC grid requires more attention due to inherent problems of reactive power fluctuations, harmonics, and unbalances, as well as certain difficulties for generators to operate in no load conditions. Control challenges of AC and DC grids are compared in the table below.

Table 2.1

Comparison of challenges for instantaneous power balancing control in AC and DC grids

Problem	AC grid	DC grid
P – active power balance	●	●
Q – reactive power balance	●	
F – frequency control; synchronization;	●	
Harmonics, 3-phase unbalance	●	
R=∞ – no load condition	●	
Imax - Inrush currents	●	●

Summing up the comparison of control challenges mentioned above, it should be mentioned that the DC power supply system is simple to control and it is expected to be more efficient due to elimination of additional power conversion stages; however, DC supply system requires more specific precautions because of short-circuit detection problems. In case of AC supply system the control task is more complicated; nevertheless, AC grid is more short circuit fault-tolerant.

2.1.2 Short-term power balancing

Instantaneous power balancing provides power sharing approach between various of sources. However, it does not provide information about the resources of the grid, for instance, islanded DC grid consisted of 1 kW source and 500 W load will operate at the same voltage level as the second islanded DC grid, which consists of 10 kW source

and 5 kW load. It means that in one case there is no possibility to supply an additional 1 kW load, but in other grid – there is such a possibility. Thus, special control approach is needed to overcome this issue.

In [52] the DC bus signalling (DBS) approach is applicable to this problem. The control technique is based on different disconnection delays for different priority loads when DC bus undervoltage condition occurs, thus enabling the lowest priority loads with shorter delays to disconnect faster, releasing power for higher-priority loads. Still, there are drawbacks that have to be mentioned. Firstly, the delays are set constantly, meaning that controllability of such an approach is limited. Secondly, there is always a trade-off between the delay periods (with longer periods it is possible to define more steps of load prioritization) and the quality of DC bus voltage: the longer are delays, the deeper voltage dips are.

2.1.3 Long-term power balancing

According to literature sources [27], with proper control of microgrids it is possible to implement long-term objectives, such as reduction of CO_2 emissions by a certain percentage or export a defined amount of energy to the grid during some period (week, month, or even year), which could be required by contract statements or transmission network operator tasks.

It is recommended to solve this problem with artificial neural networks, which successfully predict the amount of power generated by RESs[53]. Another solution is to use genetic algorithms [54] that help to choose an optimized operation schedule for energy storage components providing reliable power supply and keeping lifetime of energy storages longer due to full charge and discharge cycles. An additional solution is provided by a pricing approach [55] based on changing the price of electrical energy, so that different loads and sources behave according to an internal logic – how to operate under certain price limits. This solution results in an additional load when the price is low and, vice versa, in load shedding when the price is high. However, it is not possible to predict amount of switched on or off load with this solution.

2.2 Contribution to power balancing approaches

The author's contribution to the topics discussed above is the following:

- Improved reconnection algorithm that takes three times less time to obtain reference values in comparison with commonly used proportional-integral regulator that allows spending less power for reconnection procedure, which can be crucial in a local grid with limited energy resources;
- Improved instantaneous and short-term power balancing techniques due to enabled communication between intelligent grid elements that provides flexibility changing reference values and eliminates voltage dips, used in mentioned prioritized power supply approaches;
- Definition of a new long-term predictive power balancing approach that is based on load categorization and enables demand-side management for households.

2.2.1 Reconnection issues

The point of common coupling of two (local and utility) grids is implemented by means of an interconnection switch (IS), which is able to measure voltages from both sides, providing these data to the local energy sources. It is also responsible for disconnection from utility grid if the quality of the electrical energy is unacceptable.

In case of single-phase problems IS disconnects the problematic phase and connects phase interconnection switch at the zero-crossing moment. The reconnection procedure is opposite – the phase interconnection switch is disconnected and then the phase switch is switched on.

In case of phase reconnection, to which the local energy source is connected, another procedure takes place, which would resynchronize both sides. As the data packet transmission time is several hundreds of milliseconds, it is not possible to control the local source in real-time. Thus, it should be implemented in a different way with one of the solutions proposed below.

Reconnection with delay

When IS is ready to reconnect, it sends a notification command to the local source, which stops operating at zero-voltage; when IS detects constant zero voltage in the local grid during safety period of 2 ms, it connects the phase to the utility grid. The reconnection to the utility grid can be made at any point, however, the maximal phase angle to enable the reconnection is chosen to be $\delta = \frac{\pi}{18}$ or 55 V of mains.

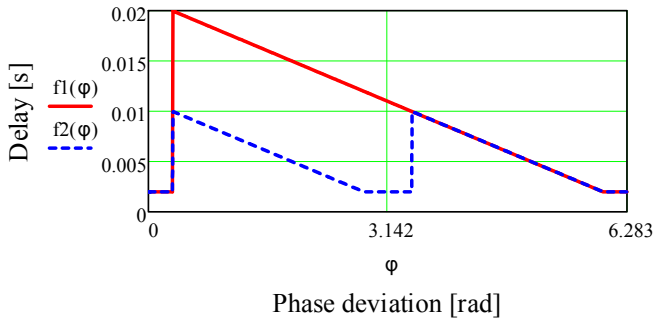

Fig. 2.3. Delay as function of the phase deviation: f1 (solid) – repeated half-periods are not allowed; f2 (dashed) – repeated half-periods are allowed

This procedure should be adopted when there are multiple sources connected to a single phase. Concerning the described method, the synchronous termination of converter operation can hardly be achieved. Thus, after receiving a notification from IS, converters should either disconnect on their own, or disconnect when the output current has increased discretely.

Reconnection by controlling frequency and voltage deviation

This approach considers that IS sends a command to the source providing parameters of reference values of voltage and frequency. When the phase and voltage deviation are neglectable, the IS reconnects to the utility grid.

Concerning multiple source connections to a single phase, the corresponding converters should synchronously raise the frequency and output voltage values; however, this is not a trivial task. In [51] it is advised to use PI regulator to implement the resynchronization procedure. The mathematical formulae of the mentioned resynchronization procedure are provided below, where (2.4)(2.5) are general

equations of AC grid operation in an islanding mode, and equations (2.6)(2.7) describe the process of reaching reference values with PI regulator.

$$f_{LG} = f_{LG}^{*} + \delta f - k_f \cdot \left(P - P^{*}\right), \tag{2.4}$$

$$E_{LG} = E_{LG}^{*} + \delta E - k_E \cdot \left(Q - Q^{*}\right), \tag{2.5}$$

$$\delta f = k_{pf} \cdot \left(f_{UG}^{*} - f_{LG}\right) + k_{if} \int \left(f_{UG}^{*} - f_{LG}\right) dt, \tag{2.6}$$

$$\delta E = k_{pE} \cdot \left(E_{UG}^{*} - E_{LG}\right) + k_{iE} \int \left(E_{UG}^{*} - E_{LG}\right) dt, \tag{2.7}$$

where

f - frequency;

E - voltage;

k_f, k_E - virtual output impedance parameters;

P, Q - active and reactive power;

δf, δE - delta values for resynchronization

k_{pf}, k_{if}, k_{pE}, k_{iE} - coefficients of PI regulator;

$\ldots^{*}$ - reference values;

$\ldots_{UG}$, $\ldots_{LG}$ -utility and local grid parameters.

In case of multiple sources this algorithm will result in reactive energy fluctuations due to the fact that PI regulators operate at different converters and could not be synchronized. Besides, this procedure takes a long time to obtain the resynchronization criteria.

The author proposes to use an integral regulator to control frequency and voltage in the local grid, limiting reactive and active power deviations during the resynchronization procedure, described by the equations below:

$$\delta f = \int k_f \cdot \left(1 + \frac{Q}{Q_{synch}}\right) \cdot \theta(f_{UG}^{*} - f_{LG}) dt, \tag{2.8}$$

$$\delta E = \int k_E \cdot \left(1 - \frac{1}{P_{synch}} \cdot \frac{dP}{dt}\right) \cdot \theta(E_{UG}^{*} - E_{LG}) dt, \tag{2.9}$$

where

P_{synch}, Q_{synch} - maximum active and reactive energy difference between sources during synchronization process;

k_f - frequency raise speed [Hz/s]

k_E - voltage raise speed [V/s]

$\theta(x) = \begin{cases} 0, & x < 0; \\ 1, & x \geq 0; \end{cases}$ - Heaviside function.

The frequency raise speed is dependent on the reactive power, so this is the source, which runs ahead another source, generates capacitive reactive energy, which results in frequency raise speed decrease (see Fig. 2.4) and vice versa, so that realising regulator's synchronization running on different converters.

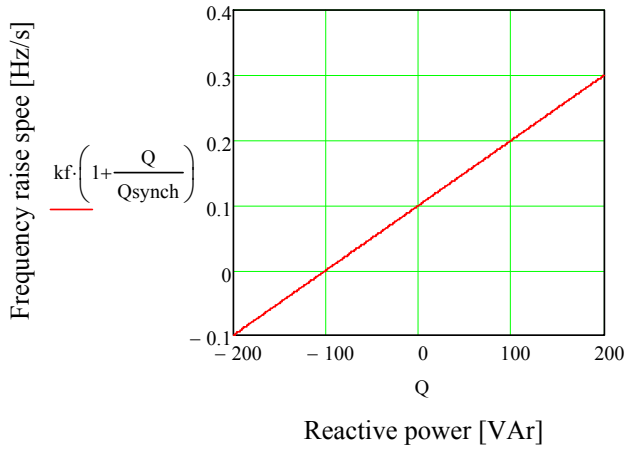

Fig. 2.4. Frequency raise speed as a function of reactive power (Q_{synch}=100 VAr, k_f =0.1 Hz/s)

The DC grid operation in islanding mode and reconnection procedure are described by equations (2.10) and (2.11).

$$V_{out} = V^* + \delta V - \frac{V^* - V_{\min}}{I_{\max}} \cdot I_{out} \tag{2.10}$$

$$\delta V = k_{pV} \cdot \left(V_{UG}^* - V_{LG}\right) + k_{iV} \int \left(V_{UG}^* - V_{LG}\right) dt \tag{2.11}$$

where

V_{out}, I_{out} - converter's output voltage and current;

V^* - voltage reference

$V_{\min}$ - minimal DC voltage at maximal output power;

$I_{\max}$ - maximal output current;

k_{pV}, k_{iV} - proportional and integral coefficient of PI regulator.

In this case the power sharing also could deviate as PI controllers run on different converters, which may cause overloading of one of the converters, which has faster PI regulator.

The author proposes to use the following algorithm of resynchronization of DC grids that is described by the equation below.

$$\delta V = \int k_V \cdot \left(1 - \frac{1}{P_{synch}} \cdot \frac{dP}{dt}\right) \cdot \theta(V_{UG}^* - V_{LG}) dt \tag{2.12}$$

where

k_V - maximal voltage raise speed [V/s];

P_{synch} - maximal allowed active power deviation during resynchronization [W];

V_{UG}^* - utility grid voltage, that is used as reference [V];

V_{LG} - local grid voltage [V].

Simulation results

The simulation result for AC grid resynchronization procedure is presented below, where the maximal frequency raise is chosen as equal for both solutions.

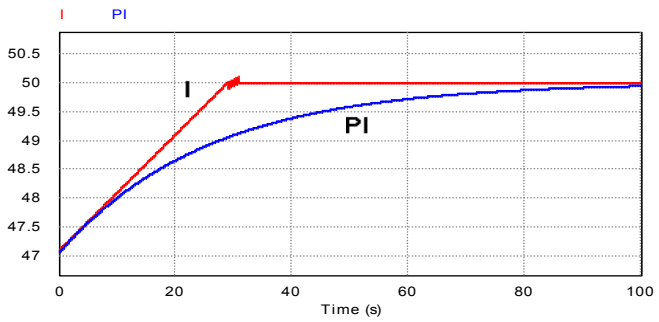

Fig. 2.5. Simulation of AC grid resynchronization with two solutions (df/dt = 0.1 Hz/s)

As it can be concluded from the figure (Fig. 2.5), the resynchronization time taken by the proposed solution is 3 times faster than with a conventional PI regulator. Besides, the phase deviation between local and utility grid sinusoid should be within the allowed limits. The phase rapidly changes if the frequency is not precisely matched, providing delays between moments of allowed reconnection, which can be seen on Fig. 2.6.

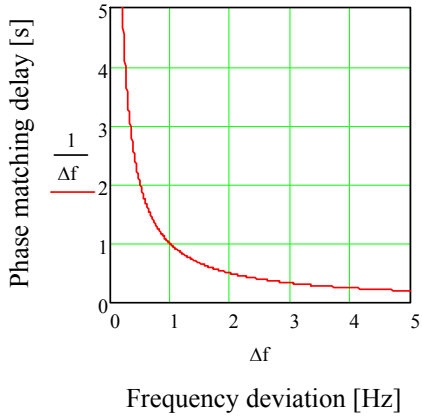

Fig. 2.6. Phase matching delay as a function of frequency deviation

According to [56] allowed frequency, voltage, and phase deviations are 0.3 Hz, 10%, and 20° respectively for power generators within 0-500 kVA range. Thus, assuming mentioned allowances, the estimated maximal delay is 2.96 s at allowed 0.3 Hz constant frequency deviation.

2.2.2 Improved instantaneous power balancing approach

The author proposes to use droop control method for keeping power balance in the grid and improving it by introducing variable reference values of a common point interface (CPI) converter. It is especially suitable for DC supply grids that always operate under the droop control method, as those are not connected to the utility grid directly, but through an AC/DC interface converter, which imports or exports energy to or from the grid, depending on the DC bus voltage. It is reasonable to use variable reference value of the DC voltage grid for an interface converter that will influence operation of local grid elements. For instance, by decreasing DC bus voltage reference value by few per-cents below the nominal value, the low priority loads will not operate or will

operate at the highest energy saving mode and, as a result, more energy will be exported to the grid.

Droop control in hybrid IDG

Two control algorithms are defined regarding grid-connected and islanded modes, as in case of grid-connected operation the AC part is supplied from the utility grid, while in the islanded mode the bidirectional converter forms a local AC grid sharing power with the local DC grid.

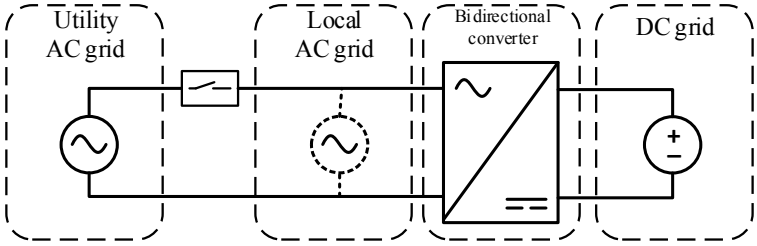

Fig. 2.7. AC and DC subgrids interlinked by bidirectional converter

Grid-connected droop control

The figure below (see Fig. 2.8.) represents the droop control method for hybrid IDG operating in a grid-connected mode. The DC grid voltage defines the power flow for common point interface converter. If the voltage is below the nominal value, the energy is consumed from AC grid operating at the grid frequency. If the DC grid voltage is above the nominal value, the bidirectional converter operates in inverter mode injecting power into AC grid, where current reference is connected to DC bus voltage.

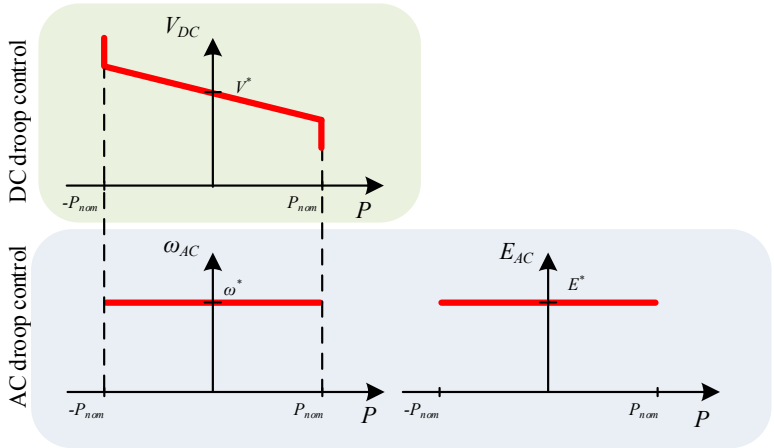

Fig. 2.8. Droop control of grid-connected hybrid IDG

The reference current for front-end active rectifier can be calculated using the equation below:

$$I_{AC} = \frac{V_{DC}^{*} - V_{DC}}{R_{virt}}. \tag{2.13}$$

Stand-alone droop control

Assuming that all energy sources are connected to the DC grid, then the DC bus voltage defines the direction of power flow as it was used in grid-connected mode. The DC grid supports the AC grid if the DC bus voltage is above the nominal value, using droop control characteristic for the AC grid reference values of frequency and voltage (see Fig. 2.9). In case if the AC source supports the DC grid, the converter operates at grid voltage and frequency without influencing them.

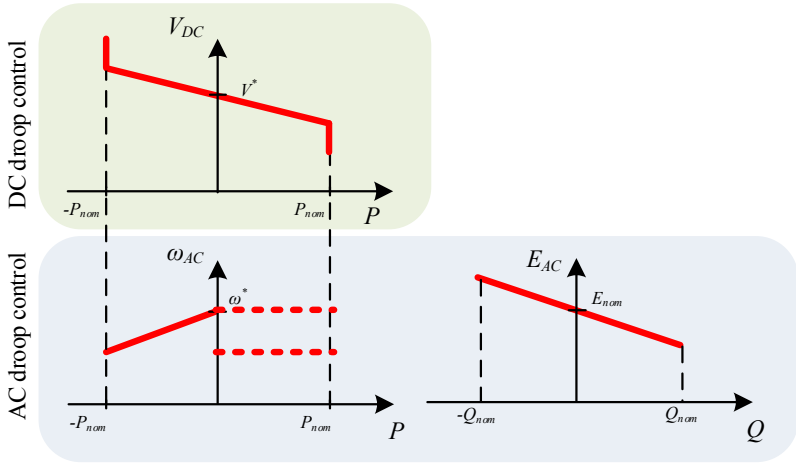

Fig. 2.9. Droop control of stand-alone hybrid IDG

2.2.3 Improved short-term power balancing approach

In order to overcome the described problem in short-term energy management, the author proposes to use communication hardware that could be applied for prioritized load power supply and shedding. then the EMS is able to receive a request from the load before the beginning of the operation, so that it allows disconnecting lower-priority loads without producing voltage dips as it was proposed to use in [52].

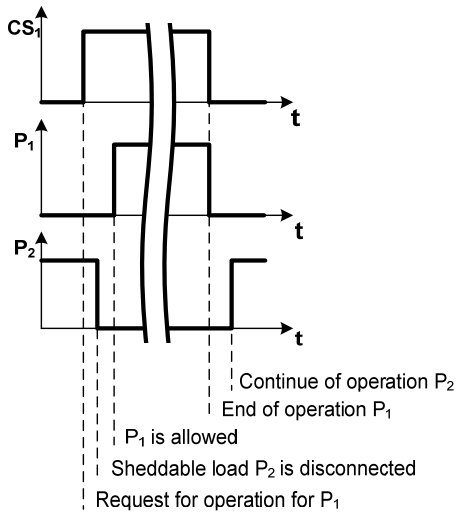

Fig. 2.10. Load shedding diagram

2.2.4 Proposed long-term power balancing technique

The author proposes to define categories of household appliances, which switch and operate at different conditions (see Fig. 2.11):

1. Time-triggered load – pumps, general lighting, etc. – the load basically switches at a nearly defined time;
2. Price-triggered load – energy storage elements [57], washing machines, etc. – the load turns on when the price lays within an acceptable level;
3. Hybrid-triggered load – heaters, boilers, refrigerators, etc.– the load operates according to a daily schedule (depending on consumption), but it can also switch on a little earlier when the price per electricity is economically profitable;
4. Price-responsive load - controllable lighting [58] – the load changes the consumed power depending on the price of electricity.

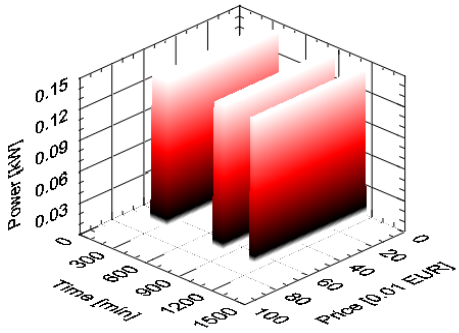

a) Time-triggered load

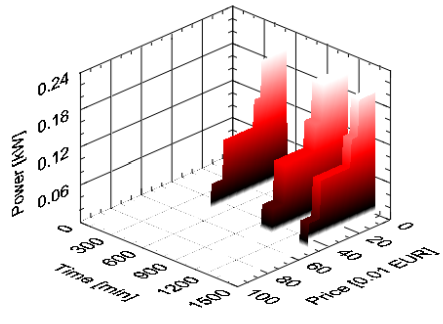

b) Price-responsive time-triggered load

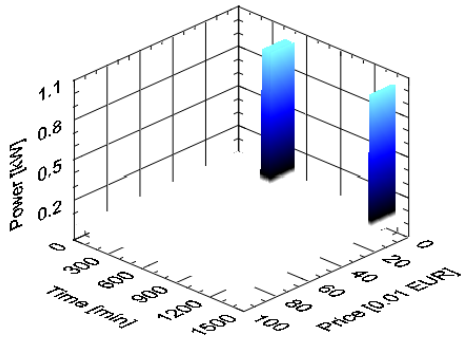

c) Price-triggered loads

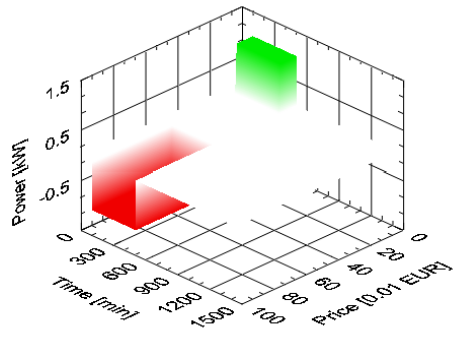

d) Price-triggered storage element

Fig. 2.11. Different load patterns

The proposed algorithm is implemented in the following way. Each load based on the statistics of use and on the changes of electrical price provides an energy management system (EMS) with a schedule of operation (for time-triggered and hybrid-triggered loads) and condition of operation (for price-triggered and hybrid-triggered loads):

$$\Psi_{load}^{(1)}(C,t) = \sum_i \left(P_{T-trig}^i\left(C_{\max},t\right)\right) + \sum_j \left(P_{C-resp}^j\left(C,t\right)\right) \tag{2.14}$$

$$\Psi_{source}(C,t) = \sum_i \left(P_{source}^i(C,t)\right) \tag{2.15}$$

After having aggregated all the data from the loads, EMS subtracts the 3D surface of demand $\Psi_{load}^{(1)}(C,t)$ (to which the power reserve is added $\Psi_{delta}(C,t)$), from the 3D

surface of generation $\Psi_{source}(C,t)$ (see Fig. 3a) to extract the interconnection line, the projection of which to Time-Cost axes is used to find the price function $C^{(1)}(t)$ (see Fig. 2.12).

$$\Psi_{source}(C,t) - \Psi^{(1)}_{load}(C,t) \geq \Psi_{delta}(C,t) \tag{2.16}$$

$$C^{(1)}(t) = \Psi_{source}(C,t) \cap \left(\Psi^{(1)}_{load}(C,t) + \Psi_{delta}(C,t)\right) \tag{2.17}$$

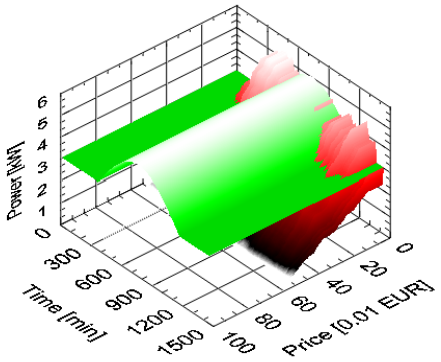

a) Primary energy balancing with time-triggered and price-responsive loads (green – generation; red – consumption)

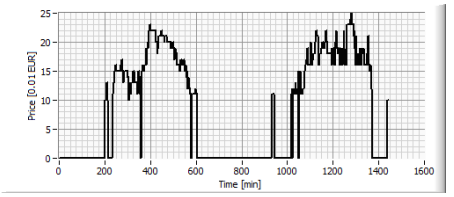

b) Price function

Fig. 2.12. Primary equalization of price function

The scheduling of price-triggered loads is also used to estimate the price function. EMS combines the price-triggered loads in accordance to energy excess, which is calculated using (2.18)

$$\Psi_{excess}(C,t) = \Psi_{source}(C,t) - \left(\Psi^{(1)}_{load}(C,t) + \Psi_{delta}(C,t)\right) \tag{2.18}$$

$$\Psi_{excess}(C,t) \geq \sum_i P^i_{C-trig}\left(C^i, t^i \middle| \begin{matrix} t_{end} \\ t_{start} \end{matrix}\right) \begin{cases} C^i < C^{i-1} \\ t^i_{satrt} \geq t^{i-1}_{start} \\ t^i_{start} + t^i_{\min} \leq t^i_{end} \leq t^i_{start} + t^i_{\max} \end{cases} \tag{2.19}$$

As a result, the price function $C^{(1)}(t)$ is changed in accordance to the switching schedule of price-triggered loads, keeping the price at a desirable level, to regulate the amount of switched price-triggered loads and the power balance.

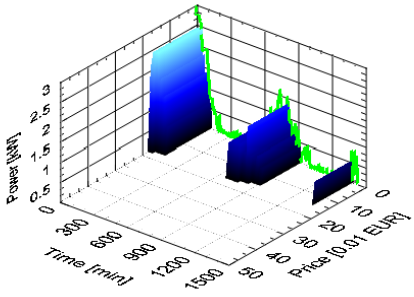

a) Secondary balancing (green – projection of energy excess; blue – scheduled price-triggered loads)

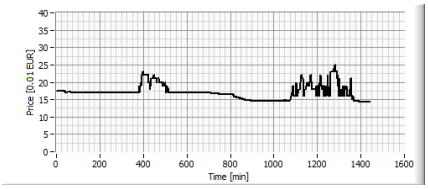

b) Resulting price per electrical energy

Fig. 2.13. Secondary equalization of price function

Thus, the proposed algorithm based on the load categorization allows load scheduling, shedding by regulating the price function, and enabling utility grid operator to implement the demand-side management.

2.3 Summary

In this chapter the following has been obtained:

1. The power balancing approaches can be divided by the period in which each approach performs the controls function (summary is observed in Table 2.2), having more advantages if communication link is used;
2. It is possible to fulfil long-term objectives with a CPI converter, which regulates its reference value for the regulation of a local grid operation mode, as other grid elements choose their operation mode in accordance with the grid voltage – the parameter available for all elements of the grid;
3. Communication provides better functionality as it allows eliminating voltage dips used in DC bus signaling for prioritized load supply, while communication prevents it. It also enables long-term energy balancing that allows implementing demand side management measures and, scheduling energy storage devices;
4. Proposed categorization of loads allows implementing predictive long-term power balancing technique that is based on pricing approach, where the price graph is obtained in two steps. The first step consists of aggregation of time-

triggered loads into 3D (price, time, power) surface and first estimation of price graph by extracting interconnection line with forecasted generation data also organized in 3D surface. Second price estimation step schedules the price-triggered loads by planning price per electricity changes in time;

5. It is proposed to use an integral regulator for reconnection purposes as it allows reaching the voltage and frequency reference values three times faster than when a standard PI regulator is used, if frequency and voltage rising speeds are considered to be equal.

Table 2.2

Overview of power balancing techniques [59]

Period of power balancing [time range]	Power balancing approach		Functionality
	Communication unavailable	Communication available	
Instantaneous [ms ... s]	Droop-control	-	Voltage and frequency control
Short-term [s ... min]	Bus signalling	Request-respond commands	Prioritized load supply
Long-term [min ... h]	-	Variable references; Dynamic pricing	Demand-side management; Energy storage scheduling; generator scheduling;

3 CONTROL OF BIDIRECTIONAL AC/DC INTERFACE CONVERTER

The key element of connecting AC grid to the local DC grid is a bidirectional AC/DC converter, responsible for efficient conversion of electrical energy in both directions, capable of supporting both sides by implementing energy balancing algorithms both in a grid-tied and in a stand-alone mode. For this reason, the forthcoming sections are dedicated to the choice of converter's topology and definition of control techniques for proposed topology, operating in different modes.

3.1 Choice of the topology

The double active bridge topology with galvanic isolation has commonly been used as AC/DC converter with a bidirectional power flow. Disadvantages of this scheme are high number of semiconductor elements in the current path, high number of switches and a necessity for a transformer, which is the heaviest component in the converter and reduces its power density. The CLLC topology allows reducing semiconductor switches[60], however it inherits resonant topology drawbacks, for instance, reduced input voltage range and a need for variable switching frequency.

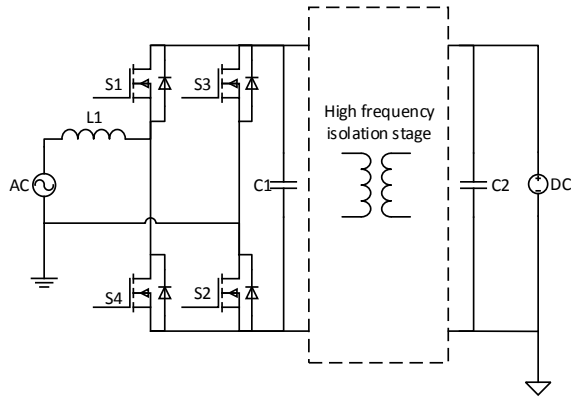

Fig. 3.1. Full bridge front-end bidirectional AC/DC converter with isolation stage

The author proposes to use common neutral point dual half-bridge topology [61], which has less switching devices and eliminates the use of transformer, as the neutral wire is not commutating during the operation of the proposed converter.

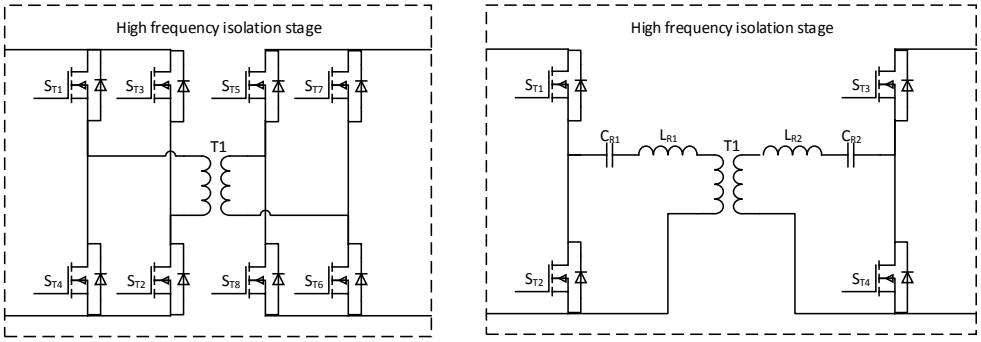

a) Dual active bridge b) CLLC isolation stage

Fig. 3.2. Two topologies of high frequency isolation stage

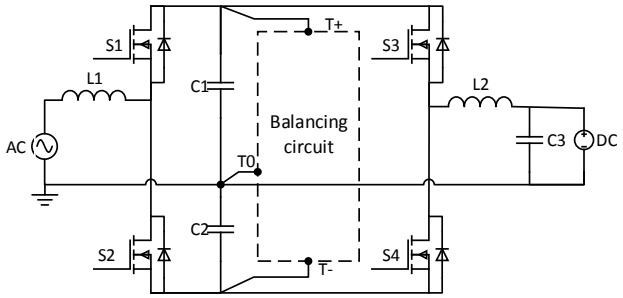

Fig. 3.3. Dual half-bridge bidirectional AC/DC converter with common neutral point

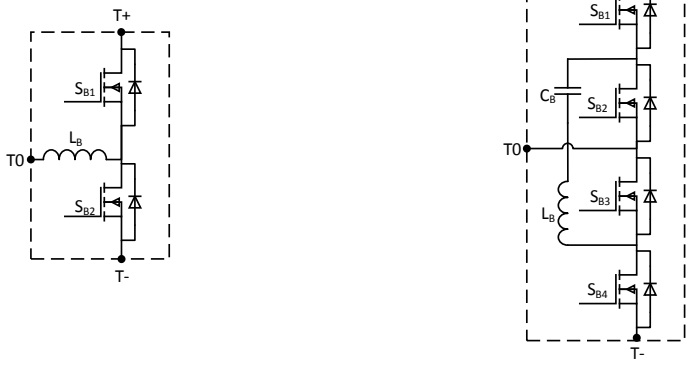

a) Hard-switched balancing circuit b) Soft-switched balancing circuit

Fig. 3.4. Capacitor balancing circuit topologies

Taking into account that the DC circuit mostly charges or discharges only upper capacitor *C1* the capacitors' voltage balancing circuit is required, which should provide half of the output power. Two solutions are considered for implementation – hard switched and resonant soft switched capacitor voltage balancing circuits (see Fig. 3.4.).

3.2 Choice of switching technique

Multiple current control techniques are known from the literature [62], [63], [64], [65], [66]: hysteresis, delta modulation, boundary switching, which relate on current measurement and all are relevant in some specific applications. On the other hand, input inductor current sensing in high frequency switched mode power supplies (SMPS) is the most challenging task, which also significantly increase the cost and size of control system as it was mentioned in various articles [67][68][69]. The current sensorless control techniques are then proposed. They eliminate instantaneous current measurement, but use other approaches for estimation of input current. In [70] it is proposed to use a slower load current measurement to estimate current of input inductor. It is advised by authors from [71] to use an average inductor current sensor that is suitable for digital control systems. In [72] the single-loop current sensorless control is being proposed, which is based on digital current rebuilding approach and uses input and output voltage values as well as predefined circuit parameters (inductor and capacitor precise values) to estimate instantaneous inductor current value. The fixed and variable switching frequencies are used in the above mentioned articles, however, according to [73], the constant frequency (see Fig. 3.5) reduces switching losses in comparison with variable frequency control, as well as reduces high-frequency components.

The following sections describe average current sensorless control technique featuring constant switching frequency, which is applicable to the proposed converter operated in grid-tied and stand-alone modes.

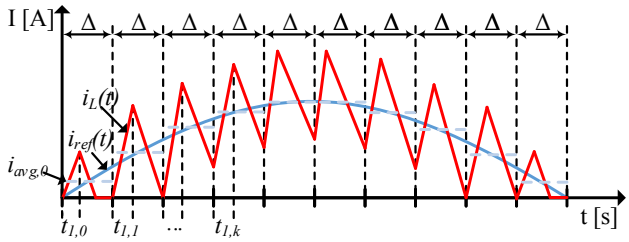

Fig. 3.5. Simplified current forms at constant frequency switching technique

3.3 Analysis of capacitors' voltages changes

The control law of the converter operation depends on instantaneous values of input voltage and capacitors' *C1* and *C2* voltages, as these parameters influence the current rising and falling slopes, which, in turn, influence the transistor conduction times to keep the average inductor current equal with the reference sinusoidal value. Thus, it is important for control system to know the functions describing changes of the capacitors voltages.

The direction of power flow depends on control of the transistors, commutating *S2* during positive period of input voltage for rectification, while *S1* is used as a diode (see Fig. 3.6.); and during negative half-period –*S1* commutates, but *S2* is represented by its diode. Inverter mode is implemented by controlling switches vice versa. As both modes are symmetrical, the positive half-period of rectification mode will be analysed further.

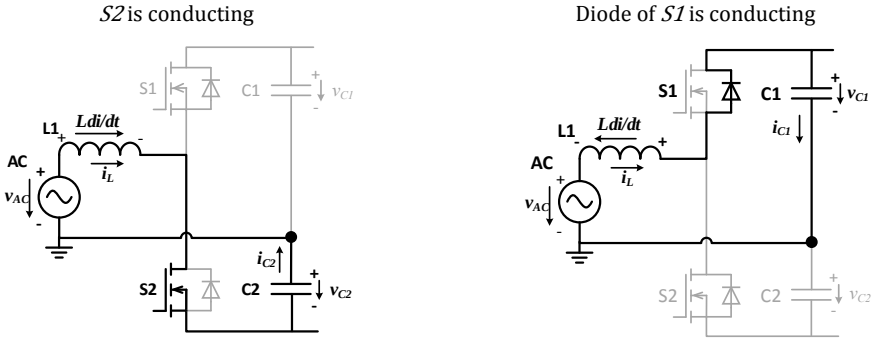

Fig. 3.6. Commutated current paths during positive half-period of input voltage

The *C2* capacitor discharges during positive half-period of input voltage, but *C1* charges. The diagram below (see Fig. 3.7) shows the timings of analysed capacitors charging and discharging periods – the *C2* is being discharged during transistor's *S2* conduction state, then the current is flowing into capacitor *C1*.

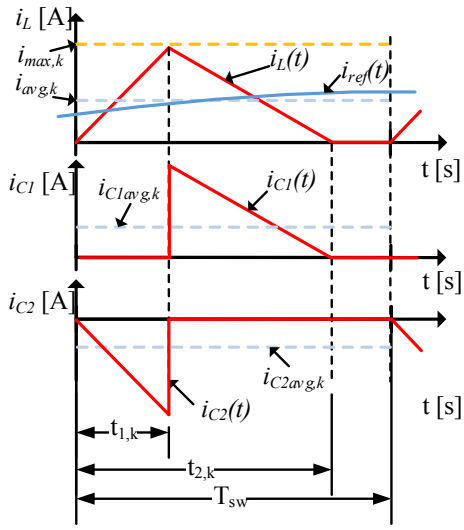

Fig. 3.7. Capacitors' *C1* and *C2* charging and discharging timings during one switching period operating at discontinuous conduction mode

The overall equation of capacitors' voltages are defined as follows:

$$v_{C1}(t) = \frac{1}{C}\int i_{C1}(t)dt + C_{C1}, \tag{3.1}$$

$$v_{C2}(t) = \frac{1}{C}\int i_{C2}(t)dt + C_{C2}, \tag{3.2}$$

and the derivatives are expressed as:

$$dv_{C1}(t) = \frac{1}{C}\cdot i_{C1}(t)\cdot dt, \tag{3.3}$$

$$dv_{C2}(t) = \frac{1}{C}\cdot i_{C2}(t)\cdot dt. \tag{3.4}$$

However, the switching mode power supply (SMPS) converter operates at a defined frequency that requires discrete analysis of the separate switching processes. Taking into account that switching frequency usually is much higher than grid frequency, it allows assuming that input voltage and capacitor voltages remain constant during one switching period, identifying values of parameters at different switching periods with an index. The pulsed capacitor currents can be replaced with average values in order to simplify the discrete analysis. Thus, the changes of capacitor's voltages can be described as follows:

$$\Delta v_{C1,k} = \frac{1}{C} \cdot T_{sw} \cdot i_{C1\_avg,k}, \tag{3.5}$$

$$\Delta v_{C2,k} = \frac{1}{C} \cdot T_{sw} \cdot i_{C2\_avg,k}. \tag{3.6}$$

The average current values can be defined in relation with maximal current of the inductor during discontinuous conduction mode (DCM):

$$i_{C1\_avg,k} = \frac{i_{max,k} \cdot \left(t_{2,k} - t_{1,k}\right)}{2 \cdot T_{sw}}, \tag{3.7}$$

$$i_{C2\_avg,k} = -\frac{i_{max,k} \cdot t_{1,k}}{2 \cdot T_{sw}}. \tag{3.8}$$

Taking into account that the average current of the inductor's *L1* is following the average reference current value, then the relation of these parameters can be described as:

$$i_{avg,k} = \frac{i_{max,k} \cdot t_{2,k}}{2 \cdot T_{sw}}. \tag{3.9}$$

Considering definitions in (3.8) and (3.9), the equation (3.7) can be rewritten as:

$$i_{avg,k} = i_{C1\_avg,k} - i_{C2\_avg,k}. \tag{3.10}$$

The equation (3.10) makes sense, as both *C2* discharging current and the input current are boosting the energy stored in the inductor, which then is released to the capacitor *C1*. Another feature of this equation is that the relation between the discrete parameters is valid for various values of discretisation periods. Thus, it is possible to multiply both parts of the equation (3.10) with infinitely small Δt, which gives the following result:

$$i_{C1\_avg,k} \cdot \Delta t = i_{avg,k} \cdot \Delta t + i_{C2\_avg,k} \cdot \Delta t, \tag{3.11}$$

making sense of derivatives of uninterruptable functions, as definition of the derivative is:

$$f'(t) = \lim_{\Delta t \to 0} \frac{\Delta f}{\Delta t}. \tag{3.12}$$

Thus, the equation (3.11)can be rewritten by using appropriate uninterruptable functions according to the following transformations:

$$\lim_{\Delta t \to 0} \left(i_{avg,k} \cdot \Delta t\right) = I_m \cdot sin(\omega t) dt, \tag{3.13}$$

$$\lim_{\Delta t \to 0} \left(i_{C1\_avg,k} \cdot \Delta t\right) = dv_{C1}(t) \cdot C, \tag{3.14}$$

$$\lim_{\Delta t \to 0} \left(i_{C2\_avg,k} \cdot \Delta t\right) = dv_{C2}(t) \cdot C, \tag{3.15}$$

resulting in following definition:

$$dv_{C1}(t) - dv_{C2}(t) = \frac{I_m \cdot sin(\omega t)dt}{C}. \tag{3.16}$$

Inserting both parts of the equation (3.11) under summation sign, the following expression is obtained:

$$\sum_{k=1}^{T/\Delta t} i_{C1\_avg,k} \cdot \Delta t = \sum_{k=1}^{T/\Delta t} i_{avg,k} \cdot \Delta t + \sum_{k=1}^{T/\Delta t} i_{C2\_avg,k} \cdot \Delta t. \tag{3.17}$$

Considering that Δt tends to zero, the limits of all series in the (3.17) make sense of integrals of uninterruptable functions, as the definition of the integral is:

$$\int_a^b f(t)dt = \lim_{\Delta t \to 0} \sum_{k=1}^{\infty} f(t_k) \cdot \Delta t, \tag{3.18}$$

thus, the equation (3.17) can be redefined as interrelation of uninterruptable functions according to following transformations:

$$\lim_{\Delta t \to 0} \sum_{k=1}^{T/\Delta t} i_{C1\_avg,k} \cdot \Delta t = \int_0^T i_{C1}(t)dt + C_{C1\_0} = v_{C1}(t)\Big|_0^T \cdot C + C_{C1\_0}, \tag{3.19}$$

$$\lim_{\Delta t \to 0} \sum_{k=1}^{T/\Delta t} i_{C2\_avg,k} \cdot \Delta t = \int_0^T i_{C2}(t)dt + C_{C1\_0} = v_{C2}(t)\Big|_0^T \cdot C + C_{C1\_0}, \tag{3.20}$$

$$\lim_{\Delta t \to 0} \sum_{k=1}^{T/\Delta t} i_{avg,k} \cdot \Delta t = \int_0^T I_m \cdot sin(\omega t)dt = \frac{I_m}{\omega} \cdot (-cos(\omega t))\Big|_0^T, \tag{3.21}$$

resulting in final definition with uninterruptable functions:

$$v_{C1}(t) - v_{C2}(t) = \frac{I_m}{C \cdot \omega} \cdot (1 - cos(\omega t)) + C_d, \tag{3.22}$$

where C_d is the constant, which describes the difference between capacitors' voltages at the time $t=0$.

As the relations between capacitors' voltages and derivatives are known, one of the equation variables should be defined by additional equation, which would allow creating a system of equations. For example, the average current of capacitor *C2* can be defined by using the equations of the inductor's raising and falling current, which are defined as an integral of the voltage applied to the inductor:

$$i_L(t) = \frac{1}{L}\int_0^{t_{1,k}} \big(v_{in}(t) + v_{C2}(t)\big)dt, \tag{3.23}$$

$$i_L(t) = \frac{1}{L}\int_{t_{1,k}}^{t_{2,k}} \big(v_{in}(t) - v_{C1}(t)\big)dt + i_L\big(t_{1,k}\big). \tag{3.24}$$

However, in the discrete analysis the equations above can be rewritten as follows:

$$i_{max,k} = \frac{v_{in\_avg,k} + v_{C2,k}}{L} \cdot t_{1,k}, \tag{3.25}$$

$$-i_{max,k} = \frac{v_{in\_avg,k} - v_{C1,k}}{L} \cdot \big(t_{2,k} - t_{1,k}\big), \tag{3.26}$$

from where the $\frac{t_{1,k}}{t_{2,k}}$ ratio is defined as:

$$\frac{t_{1,k}}{t_{2,k}} = \frac{v_{C1,k} - v_{in\_avg,k}}{v_{C1,k} + v_{C2,k}}. \tag{3.27}$$

The equation (3.8) can then be rewritten using (3.9) and (3.27) as:

$$i_{C2\_avg,k} = -\frac{i_{avg,k} \cdot \big(v_{C1,k} - v_{in\_avg,k}\big)}{\big(v_{C1,k} + v_{C2,k}\big)}. \tag{3.28}$$

Again, the equation above makes sense of interrelation of currents without dependency on the period value. Thus, multiplying both parts of the equation by the infinitely small Δt gives the following expression:

$$i_{C2\_avg,k} \cdot \Delta t = -\frac{i_{avg,k} \cdot \big(v_{C1,k} - v_{in\_avg,k}\big)}{\big(v_{C1,k} + v_{C2,k}\big)} \cdot \Delta t, \tag{3.29}$$

where both parts can be transformed by using the definition of derivative of an uninterruptable function:

$$\lim_{\Delta t \to 0}\big(i_{C2\_avg,k} \cdot \Delta t\big) = dv_{C2}(t) \cdot C, \tag{3.30}$$

$$\lim_{\Delta t \to 0}\left(\frac{i_{avg,k} \cdot v_{C1,k} - i_{avg,k} \cdot v_{in\_avg,k}}{\big(v_{C1,k} + v_{C2,k}\big)} \cdot \Delta t\right) = \frac{I_m \cdot sin(\omega t)dt \cdot v_{C1}(t) - I_m \cdot V_m \cdot sin^2(\omega t)dt}{\big(v_{C1}(t) + v_{C2}(t)\big)}. \tag{3.31}$$

As a result, the equation (3.29) can be rewritten as the differential equation shown below:

$$dv_{C2}(t) = -\frac{I_m \cdot sin(\omega t)dt \cdot v_{C1}(t) - I_m \cdot V_m \cdot sin^2(\omega t)dt}{C \cdot \big(v_{C1}(t) + v_{C2}(t)\big)}. \tag{3.32}$$

Now the system of the differential equations (built with (3.16) and (3.32)) contains two unknown functions of the capacitors' voltage and their derivatives:

$$\begin{cases} dv_{C1}(t) - dv_{C2}(t) = \dfrac{I_m \cdot sin(\omega t)dt}{C} \\ dv_{C2}(t) = -\dfrac{I_m \cdot sin(\omega t)dt \cdot v_{C1}(t) - I_m \cdot V_m \cdot sin^2(\omega t)dt}{C \cdot \left(v_{C1}(t) + v_{C2}(t)\right)} \end{cases} \tag{3.33}$$

Substituting the definition of $\left(\frac{I_m \cdot sin(\omega t)dt}{C}\right)$ as with a difference of derivatives $\left(dv_{C1}(t) - dv_{C2}(t)\right)$ in the second equation and rearranging variables will provide the obtained differential equation as follows:

$$v_{C2}(t)dv_{C2}(t) + v_{C1}(t)dv_{C1}(t) = \frac{I_m \cdot V_m \cdot sin^2(\omega t)dt}{C}, \tag{3.34}$$

which can be simply integrated and provide the following result:

$$\frac{{v_{C1}}^2(t)}{2} + \frac{{v_{C2}}^2(t)}{2} = \frac{I_m \cdot V_m}{4 \cdot C \cdot \omega} \cdot (2\omega t - sin(2\omega t)) + C_0. \tag{3.35}$$

The constant C_0 can be found by solving the equation above at the time $t = 0$, which provides the following result:

$$C_0 = \frac{{v_{C1}}^2(0)}{2} + \frac{{v_{C2}}^2(0)}{2}. \tag{3.36}$$

Replacing $v_{C1}(t)$ using definition (3.22), the capacitor's C_2 voltage function is defined as:

$$\begin{aligned} {v_{C2}}^2(t) + v_{C2}(t) \cdot \left(\frac{I_m}{C \cdot \omega} \cdot (1 - cos(\omega t)) + C_d\right) + \frac{\left(\frac{I_m}{C \cdot \omega} \cdot (1 - cos(\omega t)) + C_d\right)^2}{2} \\ = \frac{I_m \cdot V_m}{4 \cdot C \cdot \omega} \cdot (2\omega t - sin(2\omega t)) + C_0, \end{aligned} \tag{3.37}$$

which can be solved as a simple square equation ($ay^2 + by + c = 0$), where:

$$a(t) = 1,$$

$$b(t) = \frac{I_m}{C \cdot \omega} \cdot (1 - cos(\omega t)) + C_d,$$

$$c(t) = \frac{\left(\frac{I_m}{C \cdot \omega} \cdot (1 - cos(\omega t)) + C_d\right)^2}{2} - \frac{I_m \cdot V_m}{4 \cdot C \cdot \omega} \cdot (2\omega t - sin(2\omega t)) - C_0.$$

The roots of this equation are presented below:

$$y_1(t) = \frac{-b(t) + \sqrt{b^2(t) - 4 \cdot a(t) \cdot c(t)}}{2 \cdot a(t)}, \tag{3.38}$$

$$y_2(t) = \frac{-b(t) - \sqrt{b^2(t) - 4 \cdot a(t) \cdot c(t)}}{2 \cdot a(t)}. \tag{3.39}$$

The first root of this equation provides voltage function of the capacitor *C2*, which depends on initial capacitors' voltages and its capacitance, input voltage, and reference current amplitude values (it will be checked in the simulation later in section3.4., where control law is obtained).

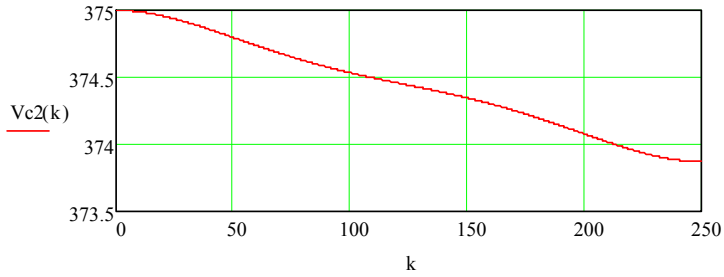

Fig. 3.8. The voltage function of capacitor C2 (C=1 mF, $V_{C1}(0)=V_{C2}(0)=375$ V, $I_m=1$ A, $V_m=311$ V, $f_{AC}=50$ Hz, $f_{sw}=25$ kHz, k – index of switching period)

The function of capacitor *C1* can be found using equation (3.22), however, the second root (3.39) provides the same result with a negative value that can be used for digital control system, as it eliminates calculation of additional trigonometric function, reducing computational time.

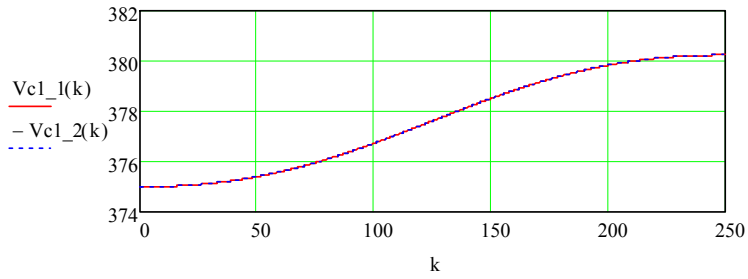

Fig. 3.9. The voltage function of capacitor *C1* obtained with two approaches

3.4 Analysis of rectification mode

To estimate the duty cycle for controlling the half-bridge at fixed frequency a certain control law should be estimated, which controls the average inductor's current at one switching period equal to the average value of reference current signal.

3.4.1 Discontinuous conduction mode

At small current values the input inductor operates at discontinuous conduction mode (DCM) (see Fig. 3.10).

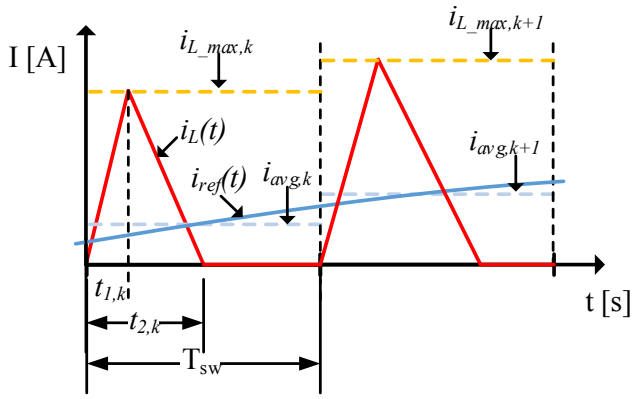

Fig. 3.10. Theoretical forms of input inductor's current at DCM

For simplicity of calculation both capacitor voltages assumed constant during one switching period, but input voltage is averaged during the switching period. Then the average current through the inductor can be described by:

$$i_{avg,k} = \frac{\frac{i_{max,k} \cdot t_{1,k}}{2} + \frac{i_{max,k} \cdot (t_{2,k} - t_{1,k})}{2}}{T_{sw}} = \frac{i_{max,k} \cdot t_{2,k}}{2 \cdot T_{sw}}. \tag{3.40}$$

Maximal current is equal to the integral of applied voltage to the inductor that was already defined previously by the equations (3.25) and (3.26), from where the t_2 is defined as:

$$t_{2,k} = \frac{v_{C1,k} + v_{C2,k}}{v_{C1,k} - v_{in\_avg,k}} \cdot t_{1,k}. \tag{3.41}$$

Then replacing unknowns $i_{max,k}$ and $t_{2,k}$ in (3.40) with definitions in (3.25) and (3.41) the average current is defined as:

$$i_{avg,k} = \frac{\frac{v_{in\_avg,k} + v_{C2,k}}{L} \cdot t_{1,k}}{2 \cdot T_{sw}} \cdot \frac{v_{C1,k} + v_{C2,k}}{v_{C1,k} - v_{in\_avg,k}} \cdot t_{1,k}, \tag{3.42}$$

from where the discrete function of transistor's conduction time is defined as:

$$t_{1,k} = \sqrt{\frac{|i_{avg,k}| \cdot 2 \cdot L \cdot T_{sw} \cdot (v_{C1,k} - v_{in\_avg,k})}{(v_{in\_avg,k} + v_{C2,k}) \cdot (v_{C1,k} + v_{C2,k})}}. \tag{3.43}$$

Considering *C1* and *C2* capacitors' voltages change in accordance to the previously obtained equations ((3.37) and (3.22)), the following control law is analytically obtained (parameters of calculation I_m=1 A, V_m=311 V, $V_{C1}(0)=V_{C2}(0)$=375 V, L=1 mH, C=1 mF, f_{sw}=25kHz).

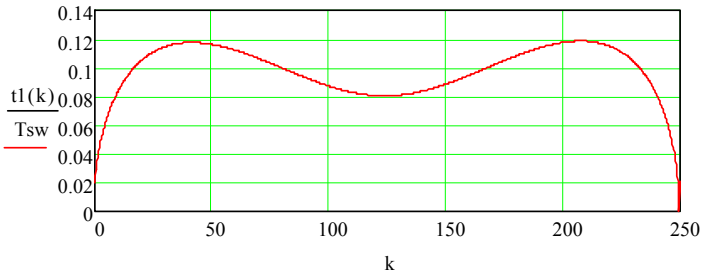

Fig. 3.11. Rectification control law for half-bridge operating in DCM

3.4.2 Boundary conduction mode

It is obvious that the boundary conduction mode (BCM) occurs when t_2 is equal to T_{sw}.

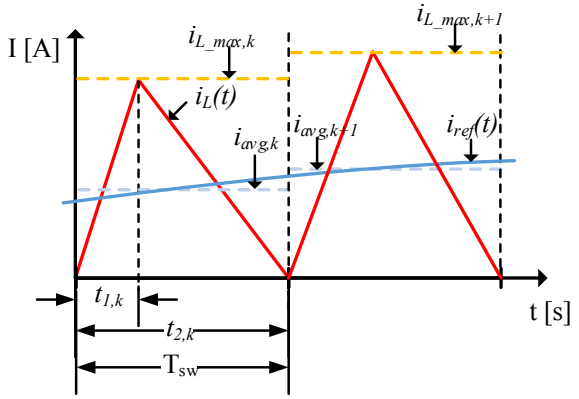

Fig. 3.12. Theoretical forms of input inductor's current at the boundary conduction mode

It is possible to define the critical value of t_1 using equation (3.41), where $t_2$can be substituted with T_{sw}, resulting in the following definition:

$$t_{1cr,k} = \frac{v_{C1,k} - v_{in\_avg,k}}{v_{C2,k} + v_{C1,k}} \cdot T_{sw}. \tag{3.44}$$

Consequently, the average input inductor's current also has a critical value, above which the continuous conduction mode (CCM) occurs. The critical value of the average

current is defined by using equations (3.43) and (3.44), which results in the following equation:

$$i_{avg\_cr,k} = \frac{t_{1cr,k}^2 \cdot \left(v_{in\_avg,k} + v_{C2,k}\right) \cdot \left(v_{C2,k} + v_{C1,k}\right)}{T_{sw} \cdot 2 \cdot L \cdot \left(v_{C1,k} - v_{in\_avg,k}\right)}. \tag{3.45}$$

The minimal point of I_{avg_cr} defines maximal amplitude of a reference signal that should be used in the control system avoiding transition to CCM of input inductor's current. In case of infinite capacitance of *C1* and *C2*, the voltages of which are assumed to be 375 V, the critical value of average current is 1.171 A, which can be observed in the diagram below.

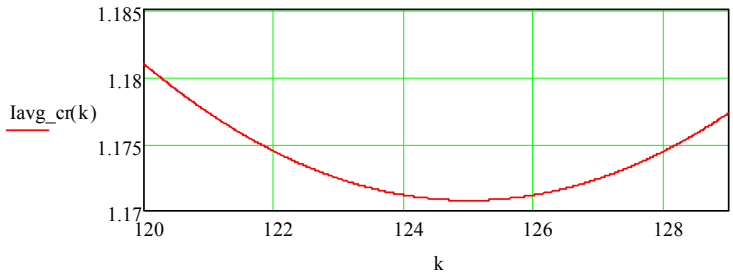

Fig. 3.13. Critical value of average input inductor's current ($C = \infty\ mF$)

However, taking into account the functions of capacitors' voltages obtained by the equations (3.22) and (3.37), the amplitude value of critical reference current for the inductor is now 1.214 A as it can be seen from the diagram below.

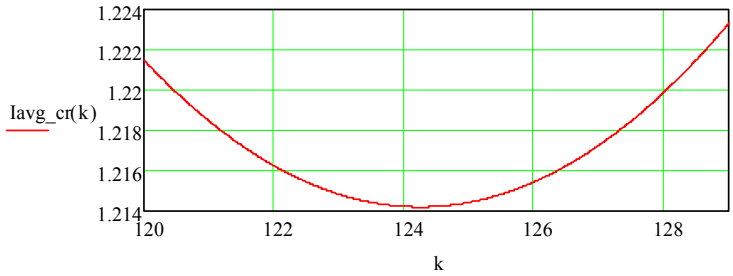

Fig. 3.14. Critical value of average input inductor's current (considering capacitors' voltages changes *C=1 mF*)

Graphically the border of DCM is observed from the diagram below, where t_1 is approaching t_{1cr}, but t_2 is approaching the switching period.

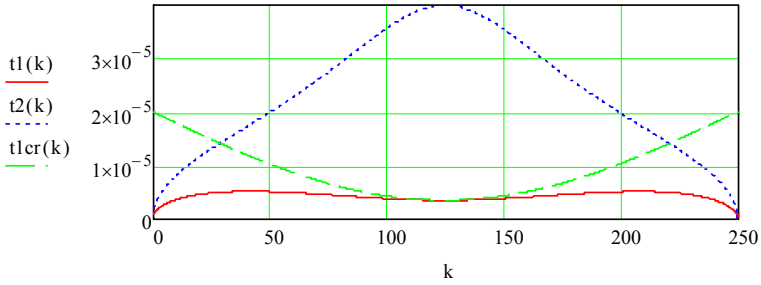

Fig. 3.15. Graphical representation of timings' critical values identifying boundary conduction mode

Concerning capacitor voltage changes the control law of half-bridge rectifier is also changed to compensate decreasing voltage on capacitor *C2* and increasing voltage on capacitor *C1*. There are two control laws shown in the diagram below, representing differences of infinite and finite capacitances.

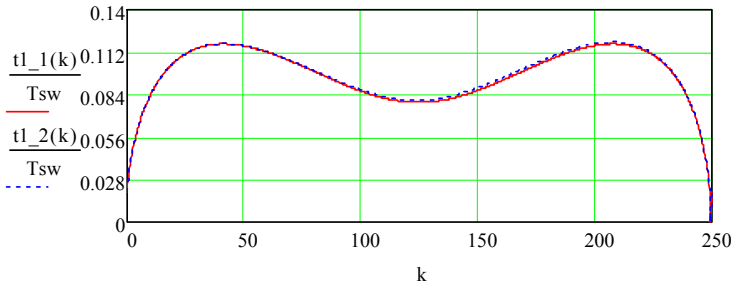

Fig. 3.16. Two control laws for half bridge rectifier representing infinite capacitance (t_{1_1}) and 1 mF (t_{1_2}) of *C1* and *C2* capacitors

Analytical values of peak and average inductor's current obtained by using the equations (3.25)and (3.40) correspondingly, as well as the reference signal are shown in the diagram below.

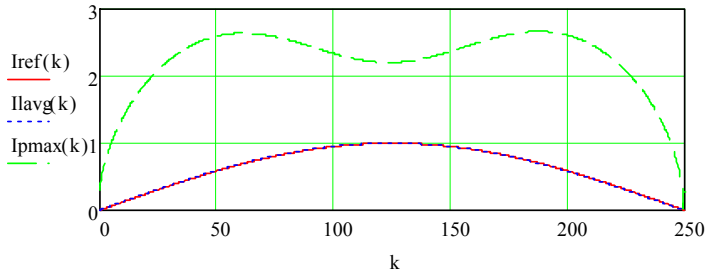

Fig. 3.17. Maximum and average inductor's currents and reference signal for DCM mode

3.4.3 Simulation of rectification at DCM

The PSIM software was used to verify the control law defined with the equation (3.43), where “Simplified C Block” was used to define the function of the duty cycle (listed in Appendix A).

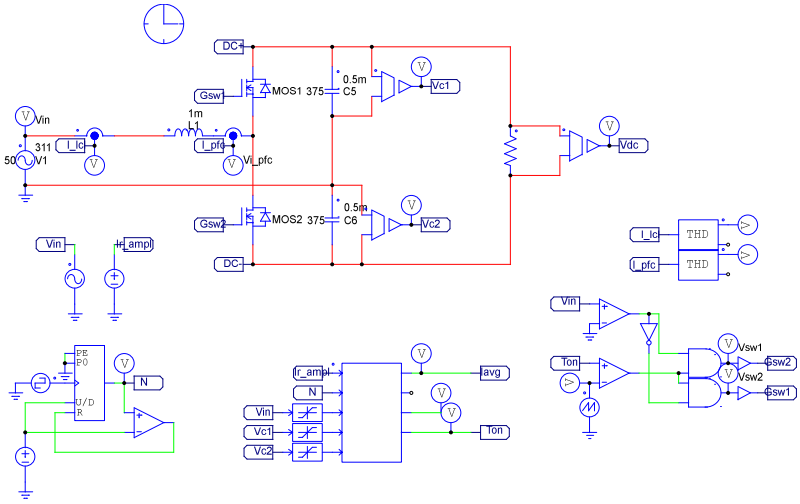

Fig. 3.18. PSIM model for testing DCM mode of half-bridge rectifier.

The simulation results are presented below (see Fig. 3.19) showing perfect match with the analytical model. The upper graph shows inductor’s current, which peak values are following the control law shown previously (see Fig. 3.17). The average current is calculated in PSIM with AVGX function showing perfect match with sinusoidal reference signal. The second diagram represents the transistor’s *S2* duty cycle that matches with analytical waveform presented before (see Fig. 3.11.). The last two diagrams represent capacitors’ voltages confirming analytically obtained results (see Fig. 3.8. and Fig. 3.9.).

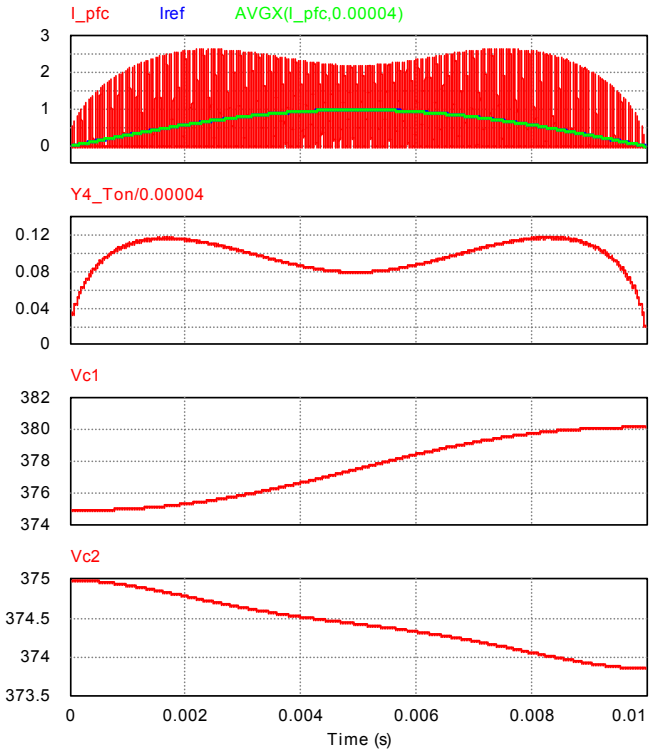

Fig. 3.19. Simulation results of rectification in DCM ($V_{C1}(0)=V_{C2}(0)=375$ V, $I_m=1$ A, $V_m=311$ V)

3.4.4 Continuous conduction mode

The control of input inductor during continuous conduction mode (CCM) requires different approach than in DCM, as average current through the input inductor depends also on the current value at the end of previous switching period (see Fig. 3.20).

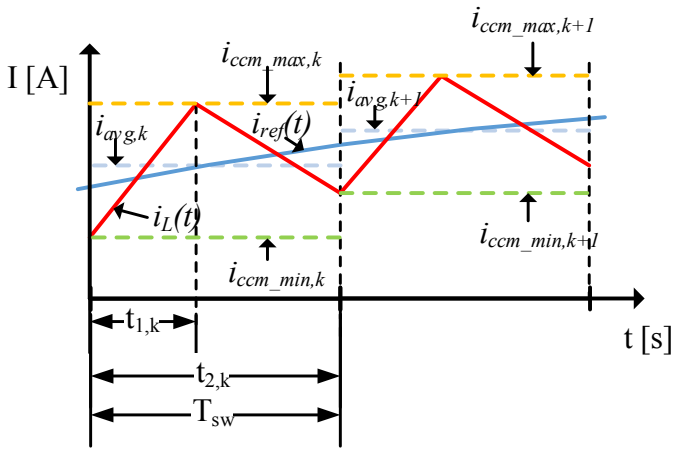

Fig. 3.20. Theoretical forms of input inductor's current at CCM

It is possible to define a relationship between rise and fall current values in order to obtain sinusoidal average inductor's current using the equation below:

$$\frac{v_{in\_avg,k} + v_{C2,k}}{L} \cdot t_{1\_ccm,k} + \frac{v_{in\_avg,k} - v_{C1,k}}{L} \cdot \left(T_{sw} - t_{1\_ccm,k}\right) = \Delta i_{ref,k}. \tag{3.46}$$

From the (3.46)the t_1 is defined as:

$$t_{1\_ccm,k} = \frac{\Delta i_{ref,k} \cdot L + \left(v_{C1,k} - v_{in\_avg,k}\right) \cdot T_{sw}}{v_{C2,k} + v_{C1,k}}. \tag{3.47}$$

The function obtained in the result is similar to the t_{1cr} defined by (3.44), however, the additional operator $\Delta I_{ref} \cdot L$ provides the average current to follow sinusoidal reference signal. The diagram below (see Fig. 3.21) demonstrates the differences between two control function (t_{1_ccm} corresponds to 2.5 A current reference ,$t_{1_ccm_2}$is 8.5 A) and critical time function.

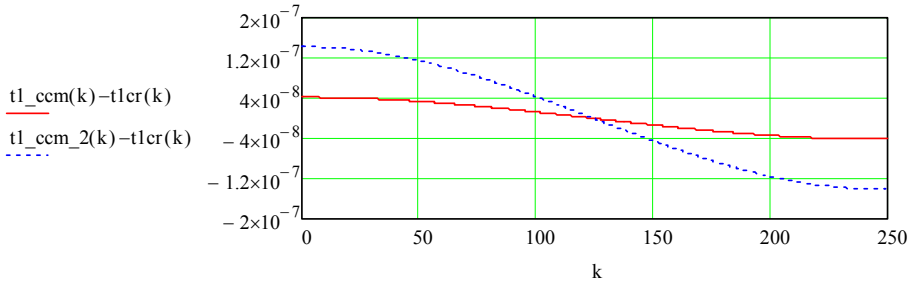

Fig. 3.21. Differences between CCM and BCM control functions

The resulted control laws for half-period operation at DCM and CCM are presented in the diagrams below (see Fig. 3.22). The CCM control function crosses DCM control function at the point, when inductor's conduction time (t_{2_dcm}) is equal to the switching period, identifying transition between DCM and CCM.

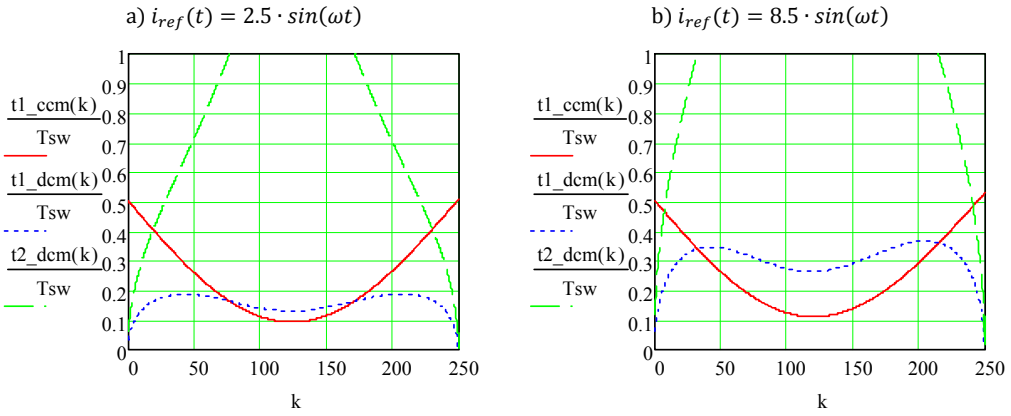

Fig. 3.22. Timing waveforms of rectification control law at CCM at different current reference values

3.4.5 Simulation of CCM control law

The simulation of CCM control law described by the equation (3.47) was tested in PSIM software. The control function switches between DCM and CCM control laws by choosing minimal value of them. The results of simulation are presented below (see Fig. 3.23).

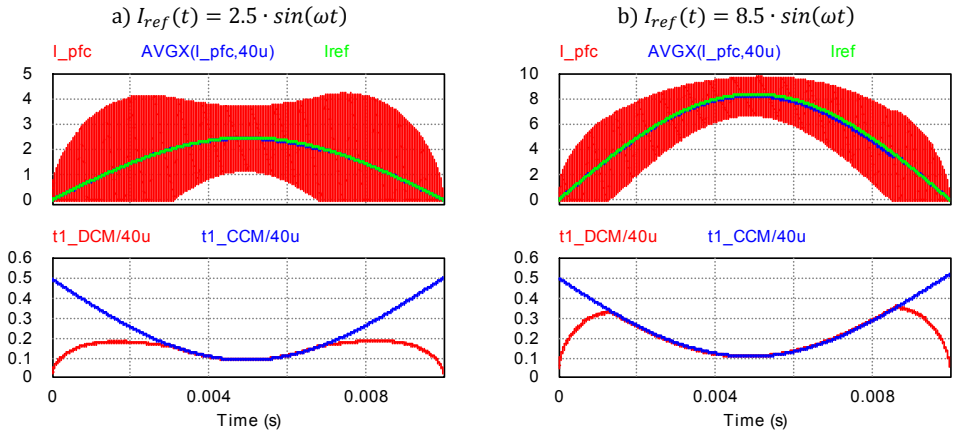

Fig. 3.23. Simulation result of rectification with CCM period

The duty cycle function is seen on the bottom side (t_{1_DCM} and t_{1_CCM}), which is divided by switching period in order to get a value in range from 0 to 1. It follows the analytical graphs (see Fig. 3.22.) choosing minimal between t_{1_DCM} and t_{1_CCM}.

3.4.6 Hysteresis control for CCM

Although current sensorless control is defined, it is difficult to build a mathematical model of the real converter operation at CCM due to non-linear passive components. For instance, inductor's inductance decreases at higher current levels, moreover, it also depends on temperature[74]. Thus, the current sensor can be used to build an adaptive hysteresis control in order to control the average current through input inductor in CCM, keeping the switching frequency nearly constant.

Hysteresis control requires two functions – the upper (I_{ccm_max}) and the lower (I_{ccm_min}) levels of inductor's current. The first one can be extracted from the formula of average current, which is defined as a summation of areas S_1 to S_4, shown in the figure below (see Fig. 3.24).

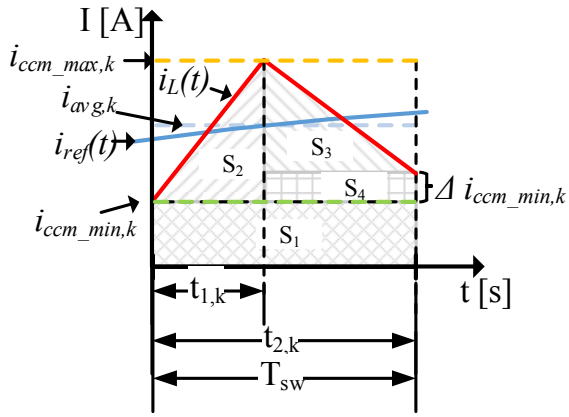

Fig. 3.24. Graphical representation of average current value

The corresponding formula of the average current during one switching period then is defined as:

$$i_{avg,k} \cdot T_{sw} = i_{ccm\_min,k} \cdot T_{sw} + \frac{v_{in\_avg,k} + v_{C2,k}}{L} \cdot \frac{t_{1\_ccm,k}^2}{2} + \frac{v_{C1,k} - v_{in\_avg,k}}{L} \cdot \frac{\left(T_{sw} - t_{1\_ccm,k}\right)^2}{2} + \Delta i_{ccm\_min,k} \cdot \left(T_{sw} - t_{1\_ccm,k}\right), \quad (3.48)$$

where $\Delta i_{ccm\_min,k}$ is defined as a difference between rising and falling inductor's current values:

$$\Delta i_{ccm\_min,k} = \frac{v_{in\_avg,k} + v_{C2,k}}{L} \cdot t_{1\_ccm,k} + \frac{v_{in\_avg,k} - v_{C1,k}}{L} \cdot \left(T_{sw} - t_{1\_ccm,k}\right). \quad (3.49)$$

Consequently, the $I_{ccm\_min}(t)$ function is defined with the equation below:

$$i_{ccm\_min,k} = i_{avg,k} - \frac{v_{in\_avg,k} + v_{C2,k}}{2L} \cdot \frac{t_{1\_ccm,k}^2}{T_{sw}} - \frac{v_{C1,k} - v_{in\_avg,k}}{2L} \cdot \frac{\left(T_{sw} - t_{1\_ccm,k}\right)^2}{T_{sw}} - \Delta i_{ccm\_min,k} \cdot \frac{\left(T_{sw} - t_{1\_ccm,k}\right)}{T_{sw}}. \quad (3.50)$$

The upper limit of inductor's current for hysteresis control is based on lower current limit and inductor's peak current amplitude, which is defined as:

$$i_{ccm\_max,k} = i_{ccm\_min,k} + \frac{v_{in\_avg,k} + v_{C2,k}}{L} \cdot t_{1\_ccm,k}. \quad (3.51)$$

The same current limits of adaptive hysteresis control can be defined as a deviation from the reference value. Assuming that reference current signal crosses inductors current at the middle of the transistor conduction time, then the I_{ccm_min} and I_{ccm_max} functions can be also described by two equations presented below:

$$i_{ccm\_min,k} = i_{ref}(t_k) - \left(\frac{v_{in\_avg,k} + v_{C2,k}}{L} - \frac{\Delta i_{ref,k}}{T_{sw}}\right) \cdot \frac{t_{1\_ccm,k}}{2}, \quad (3.52)$$

$$i_{ccm\_max,k} = i_{ref}(t_k) + \left(\frac{v_{in\_avg,k} + v_{C2,k}}{L} + \frac{\Delta i_{ref,k}}{T_{sw}}\right) \cdot \frac{t_{1\_ccm,k}}{2}. \quad (3.53)$$

The differences between the two calculation approaches are neglectable (see Fig. 3.25.), thus, the second approach is preferable for a digital control system due to its lower computational requirements.

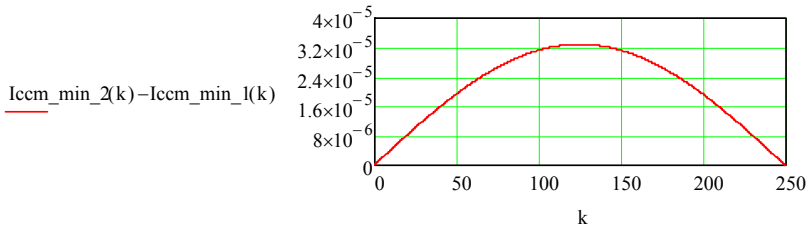

Fig. 3.25. Comparison of hysteresis control limits estimation with two approaches (I_M=8.5 A)

Analytical waveforms of current waveforms of adaptive hysteresis control are presented below (see Fig. 3.26) for different values of reference current (peak values

2.5 A and 8.5 A). The I_{CCM_min} function is negative at DCM and positive at CCM, crossing zero line at the same point, when t_2 becomes equal to the switching period (see Fig. 3.22), but t_1 becomes higher than t_{1_cr} identifying transition to CCM. The I_{CCM_max}function matches the graph of DCM peak current at the point of boundary conduction mode, meaning that the amplitude of current peaks will fluently change after transition to CCM. The I_{CCM_max} function changes its form depending on the reference current amplitude, having multiple extremum during half-period at smaller reference current values, with extremum at quarter of the period smaller than other extremum points. The function has one extremum point at higher reference current values, which can be seen in the diagrams below.

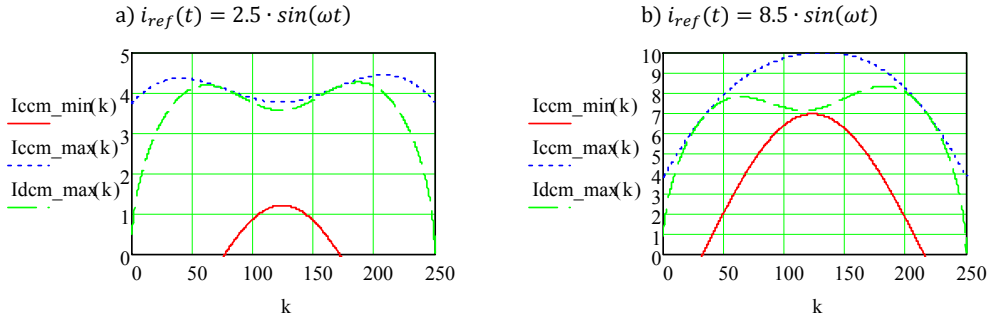

Fig. 3.26. Current waveforms of rectification with hysteresis control at different current reference values

3.4.7 Simulation of hysteresis control for CCM

Simulation of hysteresis control algorithm in PSIM software revealed similar results to the analytical model. The simulation model differs from the previous, as the control block now generates the switch on pulse, but outside circuitry switches the transistor off, when inductor's current is greater than the upper limit. After CCM mode the saw-tooth signal starts from initial condition, which prevents transition disturbances. The corresponding control algorithm is listed in Appendix B.

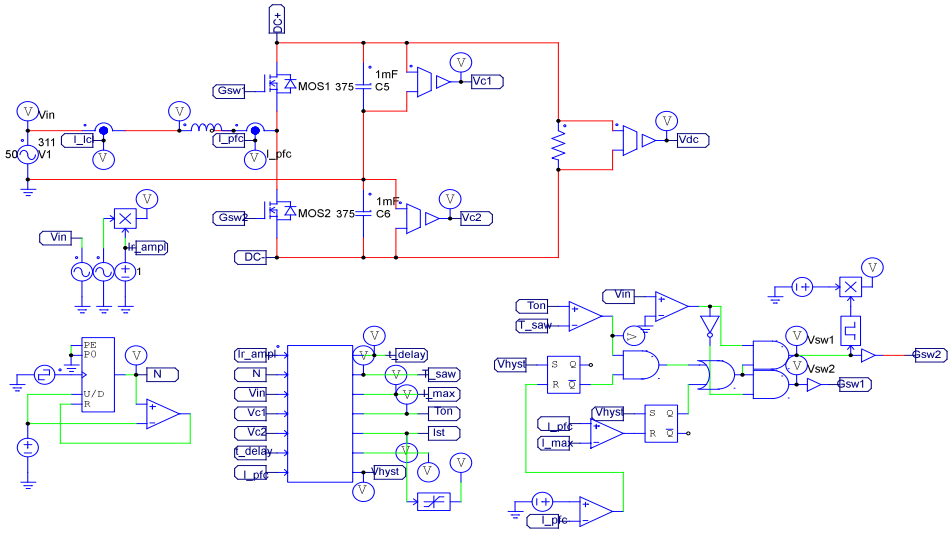

Fig. 3.27. PSIM model of hysteresis control scheme

The average inductor's current follows precisely the reference signal (see Fig. 3.28. bottom images) by applying two functions ($I_{ccm_max}$and I_{ccm_min}) for hysteresis control during CCM.

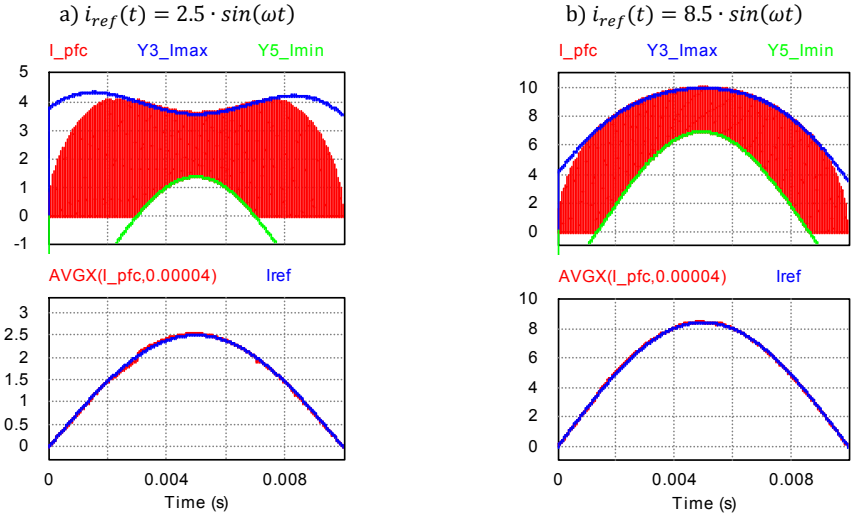

Fig. 3.28. PSIM simulation results of rectification with hysteresis control

3.5 Analysis of grid-tied inverter mode

The analysis of converter operating in inverter mode is similar to the analysis of the rectification mode, thus, some steps of the analysis will not be discussed in details.

The capacitors' voltages describe the same equations ((3.37)-(3.39) and (3.22)) that were defined for the rectification mode, modifying only sign of the reference current amplitude value that identifies reversed direction of power flow.

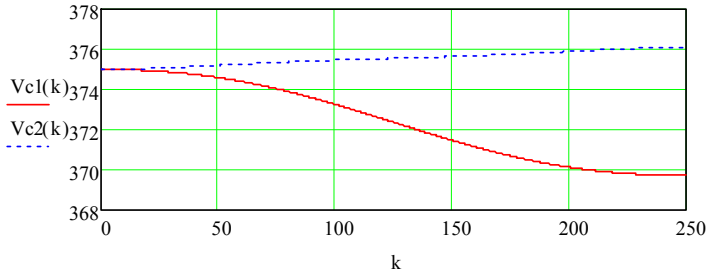

Fig. 3.29. Capacitor's voltages changes in inverter mode ($v_{C1}(0) = v_{C2}(0) = 375\ V$, I_m=-1 A)

3.5.1 Discontinuous conduction mode

During DCM operation, the maximal inductor's peak current is described by the following equations:

$$i_{L1}(t) = \frac{1}{L}\int_{0}^{t_1}\left(-v_{C1}(t) + v_{in}(t)\right)dt, \tag{3.54}$$

$$i_{L2}(t) = \frac{1}{L}\int_{t_1}^{t_2}\left(v_{C2}(t) + v_{in}(t)\right)dt + i_{L1}(t_1). \tag{3.55}$$

The following expressions are obtained by transforming the equations presented above accordingly to the discrete analysis:

$$-i_{max,k} = \frac{-v_{C1,k} + v_{in\_avg,k}}{L} \cdot t_{1,k}, \tag{3.56}$$

$$i_{max,k} = \frac{v_{C2,k} + v_{in\_avg,k}}{L} \cdot \left(t_{2,k} - t_{1,k}\right), \tag{3.57}$$

from where the time function $t_{2,k}$ can be defined in respect to $t_{1,k}$ as:

$$t_{2,k} = \frac{v_{C1,k} + v_{C2,k}}{v_{C2,k} + v_{in\_avg,k}} \cdot t_{1,k}. \tag{3.58}$$

The time function $t_{1,k}$is estimated by using equation (3.40), where unknowns $t_{2,k}$ and $i_{max,k}$ are replaced with definitions (3.58) and (3.56) correspondingly, which results in the following control law:

$$t_{1,k} = \sqrt{\frac{|i_{avg,k}| \cdot 2 \cdot L \cdot T_{sw} \cdot (v_{C2,k} + v_{in\_avg,k})}{(v_{C1,k} - v_{in\_avg,k}) \cdot (v_{C1,k} + v_{C2,k})}}. \tag{3.59}$$

The graphical representation of the mentioned timing functions for the reference current value I_m=*-1 A* are presented below (see Fig. 3.30).

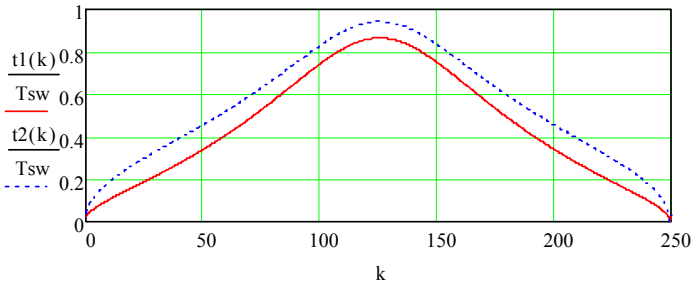

Fig. 3.30. Control law for grid-tied inverter mode operating in DCM (I_m=*-1 A*)

The critical time $t_{1cr,k}$, which identifies the boundary conduction mode, is defined as:

$$t_{1cr,k} = \frac{v_{C2,k} + v_{in\_avg,k}}{v_{C1,k} + v_{C2,k}} \cdot T_{sw}. \tag{3.60}$$

It is possible to obtain critical amplitude value of reference current signal from equation (3.59) by using critical time ($t_{1cr,k}$) definition. The lowest point of the critical current graph will determine the highest amplitude of reference signal for operation at DCM. For the inverter mode the mentioned critical amplitude has been estimated as 1.119 A.

The control law of transistor's conduction time was evaluated in PSIM that confirmed correctness of the capacitors' voltages and current waveform equations (see Fig. 3.31.).

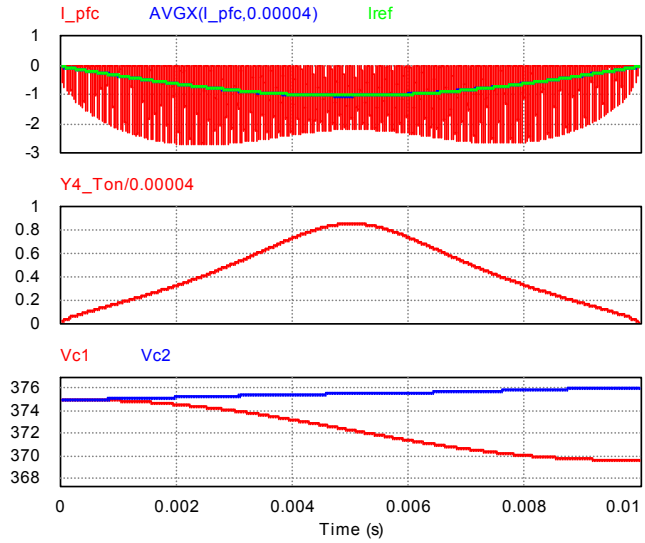

Fig. 3.31. Simulation results for inverter mode operating at DCM (I_m=*-1 A*)

3.5.2 Continuous conduction mode

In order to obtain control law for CCM period of inductor's current during reversed power flow, the inductors voltage integral ($i_L\big|_0^{T_{sw}}$) is equalised with derivative of reference current, as it is defined with the equation below:

$$-\frac{v_{C1,k}-v_{in\_avg,k}}{L}\cdot t_{1\_ccm,k}+\frac{v_{C2,k}+v_{in\_avg,k}}{L}\cdot\left(T_{sw}-t_{1\_ccm,k}\right)=\Delta i_{ref,k}, \tag{3.61}$$

which is used to define the transistor's conduction time during CCM:

$$t_{1\_ccm,k}=\frac{-\Delta i_{ref,k}\cdot L+\left(v_{C2,k}+v_{in\_avg,k}\right)\cdot T_{sw}}{v_{C2,k}+v_{C1,k}}. \tag{3.62}$$

The timing function $t_{1_ccm,k}$is also used to describe maximal and minimal waveforms of inductor's current, which, in turn, can be used for adaptive hysteresis control during CCM. The equations that describe theoretical current waveforms are presented below:

$$i_{ccm\_min,k}=i_{ref}(t_k)-\left(\frac{v_{C1,k}-v_{in\_avg,k}}{L}-\frac{\Delta i_{ref,k}}{T_{sw}}\right)\cdot\frac{t_{1\_ccm,k}}{2}, \tag{3.63}$$

$$i_{ccm\_max,k}=i_{ref}(t_k)+\left(\frac{v_{C1,k}-v_{in\_avg,k}}{L}+\frac{\Delta i_{ref,k}}{T_{sw}}\right)\cdot\frac{t_{1\_ccm,k}}{2}. \tag{3.64}$$

Graphical representation of these equations is presented below, demonstrating current waveforms for two amplitudes of reference signal.

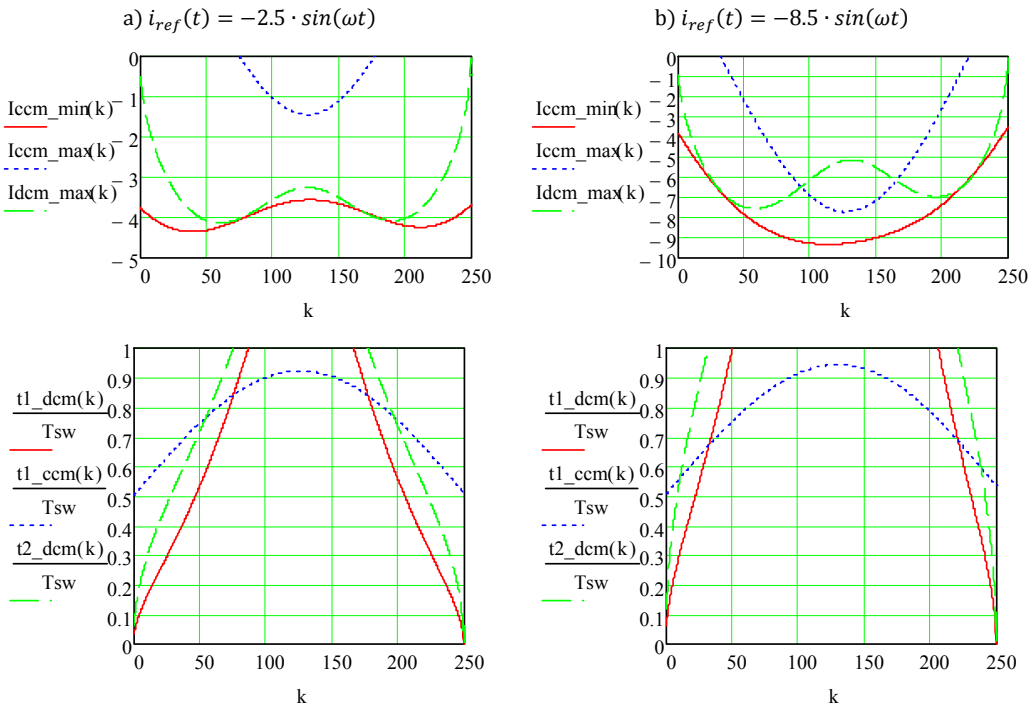

Fig. 3.32. Timing and current functions for operation in grid-tied inverter mode

The analytical model was approved with the simulation results presented below.

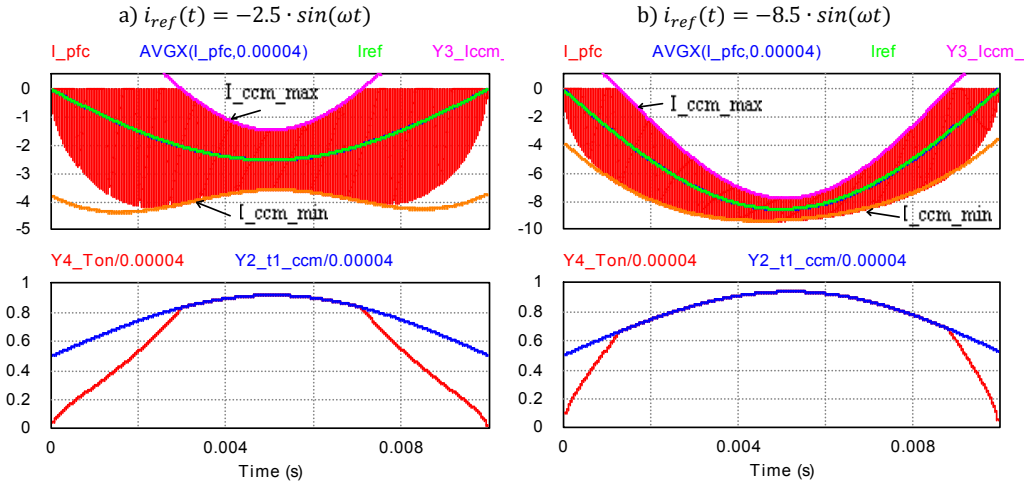

Fig. 3.33. Simulation result of grid-tied inverter mode with CCM period

3.6 Analysis of stand-alone inverter mode

Converter's operation in a stand-alone inverter mode differs from the grid-tied inverter mode, as inductor's current in not rising and falling linearly. Instead, it follows an exponential function because of the high resistance of the grid, which limits the inductor's current.

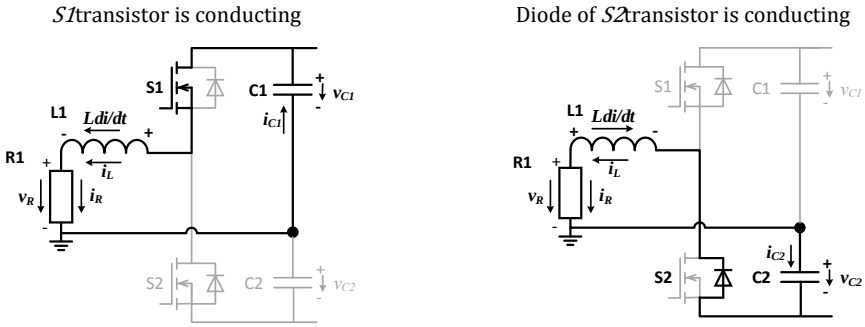

Fig. 3.34. Current paths during positive half-period of generated voltage for stand-alone inverter mode

The theoretical maximal of inductor's current can be described as:

$$I_{max} = \frac{V_c}{R}, \tag{3.65}$$

where

V_c – capacitor's voltage [V],

R – active resistance [Ω].

The theoretical waveform of inductor's current is presented in the figure below. The absolute value of the current is starting to rise when transistor *S1* is switched on and capacitor *C1* is connected to the AC side. The current derivative in first moment is equal to $-\frac{v_{C1,k}}{L}$ with following exponential decay till the theoretical current maximum $-\frac{v_{C1,k}}{R}$. After the transistor is switched off, the current is decreasing at a high rate, as both voltage drop on the load and capacitor's *C2* voltages are applied in reversed direction in respect to inductor's electromotive force.

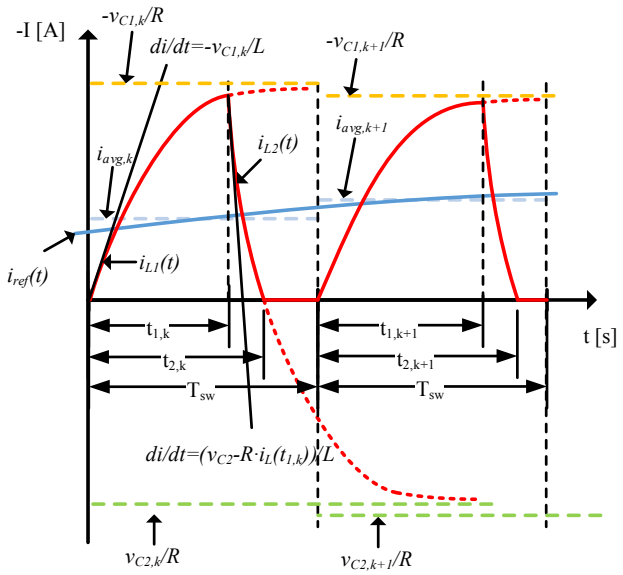

Fig. 3.35. Theoretical forms of input inductor's current at DCM operating in stand-alone inverter mode

Consequently, special control law is to be developed in order to control average current flowing through the input inductor.

3.6.1 Discontinuous conduction mode

Mathematically, the current form can be described with two equations shown below, concerning transistor's *T1* conduction time (from 0 till $t_{1,k}$) and current fall (from $t_{1,k}$ till $t_{2,k}$):

$$i_L(t) = \frac{1}{L}\int_0^{t_{1,k}} (-v_{c1}(t) - i_L(t)\cdot R)dt\,, t \in [0, t_{1,k}], \tag{3.66}$$

$$i_L(t) = \frac{1}{L}\int_{t_{1,k}}^{t_{2,k}} (v_{c2}(t) - i_L(t)\cdot R)dt + i_L(t_1), t \in [t_{1,k}, t_{2,k}]. \tag{3.67}$$

Taking into account that absolute values of both equations provide equal results during DCM, concerning previously defined assumptions, it is possible to rewrite them as follows:

$$\frac{v_{c1,k}\cdot t_{1,k}}{L} + \frac{R}{L}\int_0^{t_{1,k}} i_L(t)dt = \frac{v_{c2,k}\cdot (t_{2,k} - t_{1,k})}{L} - \frac{R}{L}\int_{t_{1,k}}^{t_{2,k}} i_L(t)dt, \tag{3.68}$$

where both integrals of inductor's current provides area of inductor's current form, which is equal to the average value of reference current, multiplied with the period:

$$\int_0^{t_{1,k}} i_L(t)dt + \int_{t_{1,k}}^{t_{2,k}} i_L(t)dt = T_{sw} \cdot i_{avg,k}. \tag{3.69}$$

Substituting inductor's current integrals in (3.68) with the definition above, the time function $t_2(t)$can be estimated as follows:

$$t_{2,k} = \frac{\left(v_{c1,k} + v_{c2,k}\right) \cdot t_{1,k} + R \cdot i_{avg,k} \cdot T_{sw}}{v_{c2,k}}. \tag{3.70}$$

In order to find the current raising and falling waveform functions, the equations (3.66) and (3.67) are rewritten substituting current functions with derivatives of unknown functions (y_1' and y_2'), current integrals with the unknown functions (y_1 and y_2), but time function is replaced with x - the argument of unknown functions:

$$y_1' = -\frac{v_{c1,k} \cdot x}{L} - \frac{R}{L} y_1, \tag{3.71}$$

$$y_2' = \frac{v_{c2,k} \cdot x}{L} - \cdot \frac{R}{L} y_2 + y_1'. \tag{3.72}$$

Both equations represent linear differential equations of the first order, which are solved substituting the unknown functions with $(\upsilon \cdot \nu)$, providing the following equations:

$$\upsilon_1' \cdot \nu_1 + \upsilon_1 \cdot \nu_1' + \frac{R}{L} \cdot \upsilon_1 \cdot \nu_1 = -\frac{\mathrm{v_{c1,k}} \cdot x}{L}, \tag{3.73}$$

$$\upsilon_2' \cdot \nu_2 + \upsilon_2 \cdot \nu_2' + \frac{R}{L} \cdot \upsilon_2 \cdot \nu_2 = \frac{\mathrm{v_{c2,k}} \cdot x}{L} + i_L\left(t_{1,k}\right), \tag{3.74}$$

where ν function is found from the equation $\upsilon \cdot \left(\nu' + \frac{R}{L} \cdot \nu\right) = 0$, giving the same result for both equations, that is $\nu = e^{-\frac{R}{L}x}$.

The υ_1 function is found by solving equation $\upsilon_1' \cdot \nu_1 = -\frac{\mathrm{v_{c1,k}} \cdot x}{L}$. After splitting differential variables and inserting value of function ν_1 , the equation of the function υ_1 looks as follows:

$$\upsilon_1 = -\frac{v_{c1,k}}{L} \cdot \int x \cdot e^{\frac{R}{L}x}\, dx + C_1, \tag{3.75}$$

where the integral is solved with the partial integration method ($\int \rho d\sigma = \rho\sigma - \int \sigma d\rho$), which provides the following answer:

$$v_1 = -\frac{v_{c1,k} \cdot L}{R^2} \cdot \left(\frac{R}{L} \cdot x - 1\right) \cdot e^{\frac{R}{L} \cdot x} + C_1. \tag{3.76}$$

The unknown function y_1 and its derivative are now defined as:

$$y_1 = -\frac{v_{c1,k} \cdot L}{R^2} \cdot \left(\frac{R}{L} \cdot x - 1\right) + C_1 \cdot e^{-\frac{R}{L}x}, \tag{3.77}$$

$$y_1' = -\frac{v_{c1,k}}{R} - C_1 \cdot \frac{R}{L} \cdot e^{-\frac{R}{L}x}. \tag{3.78}$$

The constant C_1 can be found by using initial condition $y_1'(0) = i_L(0) = 0$, that gives $C_1 = -\frac{v_{c1,k} \cdot L}{R^2}$. Thus, the final definition of the unknown function and its derivative are defined as:

$$y_1 = \int_0^{t_{1,k}} i_L(t)dt = -\frac{v_{c1,k} \cdot L}{R^2} \cdot \left(\frac{R}{L} \cdot t - 1 + e^{-\frac{R}{L}t}\right)\Big|_0^{t_{1,k}}, \tag{3.79}$$

$$y_1' = i_L(t) = -\frac{v_{c1,k}}{R}\left(1 - e^{-\frac{R}{L}t}\right), \quad t \in [0, t_{1,k}]. \tag{3.80}$$

The function, which describes the falling current form, is solved similarly, obtaining the constant value using current ending condition $i_L(t_{2,k}) = 0$. The final result for the current and its integral is as follows:

$$y_2 = \int_{t_{1,k}}^{t_{2,k}} i_L(t)dt = \frac{v_{c2,k} \cdot L}{R^2} \cdot \left(\frac{R}{L} \cdot t - 1 + e^{-\frac{R}{L}(t - t_{2,k})}\right)\Big|_{t_{1,k}}^{t_{2,k}} - \frac{v_{c1,k}}{R} \cdot \left(1 - e^{-\frac{R}{L}t_{1,k}}\right), \tag{3.81}$$

$$y_2' = i_L(t) = \frac{v_{c2,k}}{R}\left(1 - e^{-\frac{R}{L}(t - t_{2,k})}\right), \qquad t \in [t_{1,k}, t_{2,k}]. \tag{3.82}$$

In order to obtain inverter's control law, another condition is used, concerning that raising and falling current functions' crossing at time $t_{1,k}$, thus, currents' equations can be equalised at this point $\left(y_1'(t_{1,k}) = y_2'(t_{1,k})\right)$ that gives the following equation:

$$-\frac{v_{c1,k}}{R}\left(1 - e^{-\frac{R}{L}t_{1,k}}\right) = \frac{v_{c2,k}}{R}\left(1 - e^{-\frac{R}{L}(t_{1,k} - t_{2,k})}\right). \tag{3.83}$$

After rearranging the variables the equation looks like:

$$\frac{v_{c2,k}}{v_{c1,k}} e^{-\frac{R}{L} \cdot t_{1,k}} = \left(1 + \frac{v_{c2,k}}{v_{c1,k}}\right) e^{-\frac{R}{L}t_{2,k}} - e^{-\frac{R}{L}(t_{1,k} + t_{2,k})}, \tag{3.84}$$

which gives sense of a transcendental function, as trying to extract natural logarithms from both parts, the timing function $t_{1,k}$ will be defined by the natural logarithm that contains the same timing function. Thus, this equation has no algebraic solution,

however, it could be simplified, assuming that the ratio of voltages $\frac{v_{c2,k}}{v_{c1,k}}$ is approximately equal to 1, and, secondly, the last part $\left(e^{-\frac{R}{L}(t_{1,k}+t_{2,k})}\right)$ has the smallest contribution to the whole equation, because of the largest absolute value of the exponent, which, due to negative sign, tends to zero faster than other parts that contain exponent. So, the result of the performed simplification is written as:

$$e^{-\frac{R}{L}t_{1,k}} = 2 \cdot e^{-\frac{R}{L}t_{2,k}}. \tag{3.85}$$

This, in contrast to (3.84), can be solved. Considering the equation (3.70), simplified control function is defined as follows:

$$t_{1,k} = \left(\frac{R^2 \cdot i_{avg,k} \cdot T_{sw}}{L \cdot v_{c2,k}} - ln\frac{1}{2}\right) \cdot \frac{v_{c2,k} \cdot L}{v_{c1,k} \cdot R}. \tag{3.86}$$

The obtained control law is admissible at more or less equal capacitor voltages and relatively high resistance of the load. The timing function follows the sinusoidal form raised above zero line that can also be seen in the diagram below (see Fig. 3.36).

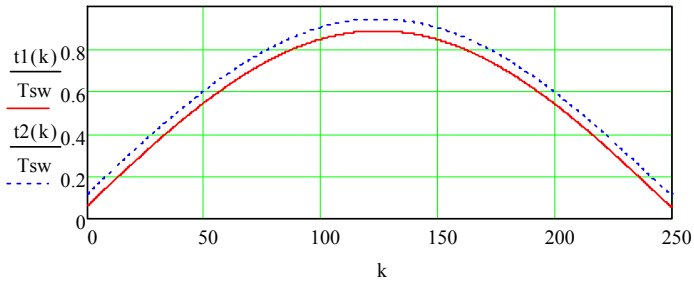

Fig. 3.36. Control law for stand-alone inverter mode operating in DCM

(I_m=-1 A,R=311 Ω,C=∞ mF)

The peak current values can be obtained for each switching period (Fig. 3.37) by using current rising and falling formulae ((3.80) and (3.82) correspondingly) and applying the control law (3.86) and definition of timing function $t_{2,k}$ by equation(3.70). The $i_{L1,k}$ represents current value at the time $t_{1,k}$, while $i_{L2,k}$ represents inductor's current value at the time $t_{2,k}$.

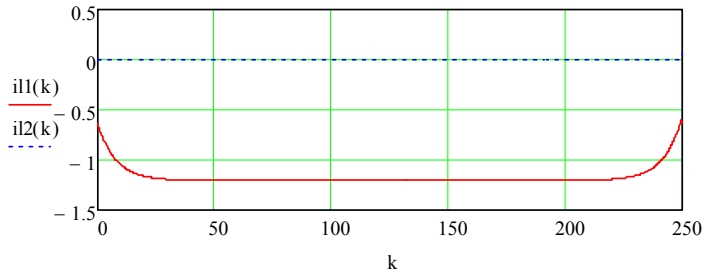

Fig. 3.37. Peak current values for stand-alone inverter mode operating in DCM (I_m=-1 A, R=311 Ω, $V_{C1}(0)=V_{C2}(0)$=375 V)

The simulation result of the obtained control law is observed in the Fig. 3.38. There is inductor's current shown in the upper graph, where it can be seen that the average inductor's current follows the reference signal, where peak current matches the analytical waveform observed in the Fig. 3.37; the middle graph shows load voltage, the average value of which follows the sinusoidal waveform with 311 V of the amplitude; the bottom graph represents the duty cycle of transistor *S1*.

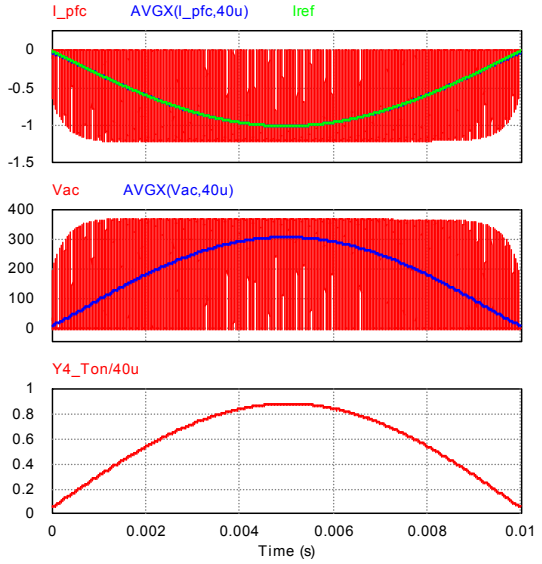

Fig. 3.38. Simulation results of stand-alone inverter mode in DCM (I_m=-1 A, R=311 Ω)

The simulations for higher loads revealed the imprecise averaged current form that deviate from the reference value near to zero crossing. Thus, in order to obtain precise control law the bisection method[75] of numerical approach for root estimation

was used for solving the transcendental equation (3.84). In the diagram Fig. 3.39. the*D1_1* graph represents a simplified control law, while *D1_2* corresponds to control law that was obtained numerically.

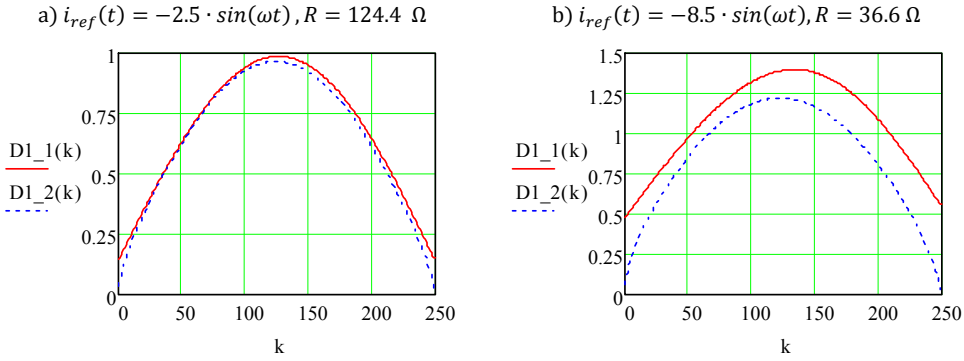

Fig. 3.39. Comparison of control laws for stand-alone inverter mode

As it was expected, the simplified control law is almost equal to the numerically solved one at lower loads, while it has a significant deviation from precise control law at a higher load.

3.6.2 Continuous conduction mode

The control of inductor's average current during CCM is performed by an approach similar to the one used before – the integral of inductor's voltages during one switching period is equalised to delta of reference current value that is written as follows:

$$\frac{-v_{c1,k} \cdot t_{1\_ccm,k}}{L} - \frac{R}{L} \cdot \int_0^{t_{1\_ccm,k}} i_L(t)dt + \frac{v_{c2,k} \cdot (T_{sw} - t_{1\_ccm,k})}{L} - \frac{R}{L} \cdot \int_{t_{1\_ccm,k}}^{T_{sw}} i_L(t)dt = \Delta i_{ref,k}. \quad (3.87)$$

The integrals of inductor's current can be replaced by using the equation (3.69) that will result in definition of control law for CCM:

$$t_{1\_ccm,k} = \frac{-\Delta i_{ref,k} \cdot L + (v_{C2,k} - R \cdot i_{avg,k}) \cdot T_{sw}}{v_{C1,k} + v_{C2,k}}. \quad (3.88)$$

Both control laws for DCM and CCM periods are observed in the Fig. 3.40., where the CCM control law crosses DCM control law at the same point, when timing function $t_{2,k}$ is equal to switching period length.

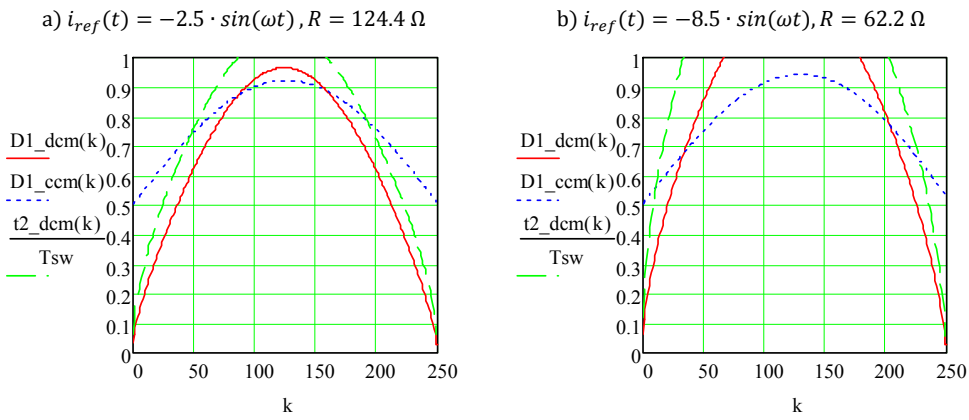

Fig. 3.40. Timing functions for operation in stand-alone inverter mode

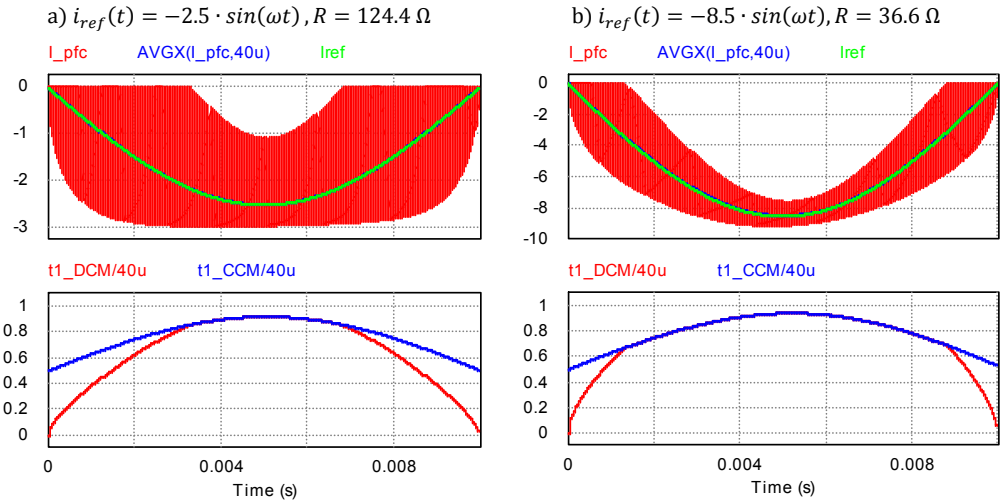

Fig. 3.41. Simulation result of stand-alone inverter mode with CCM

The simulation result of the obtained control laws for stand-alone inverter mode are shown in the Fig. 3.41., where the top diagram contains inductor's current, averaged inductor's current by period, and reference current graphs, where the last two matches precisely approve the analytical model. The bottom graph shows the control laws for DCM and CCM periods that were calculated in accordance with (3.84) and (3.88). The control algorithm is listed in Appendix C.

3.7 Capacitors' voltage balancing

The proposed converter needs a balancing circuit, since the output half-bridge mostly charges and discharges the capacitor *C1*. Thus, the balancing circuit should provide half of the power required by the output half-bridge. This balancing circuit can be implemented either as hard or soft switched as it is explained further.

3.7.1 Hard switched balancing circuit

The hard-switched balancing circuit uses two semiconductor switches and an additional inductor as an energy storage element. In order to provide energy from the capacitor *C2*, the S_{B2} switch is controlled. During S_{B2} conduction state the energy is stored in the inductor L_B and, when the S_{B2} is switched off, stored energy is released to the capacitor *C1* through a diode of S_{B1}.

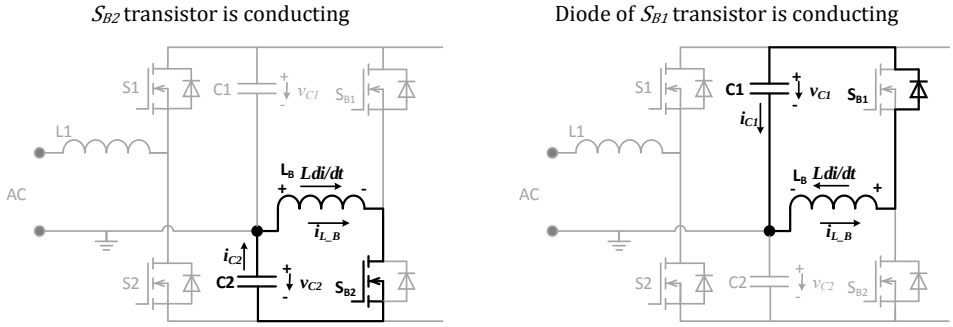

Fig. 3.42. Current paths in hard-switched capacitors' voltage balancing circuit

The current rising and falling slopes are described by the two equations below:

$$i_{max,k} = \frac{v_{C2,k}}{L_b} \cdot t_{b1,k}, \tag{3.89}$$

$$-i_{max,k} = -\frac{v_{C1,k}}{L_B} \cdot \left(t_{2,k} - t_{1,k}\right), \tag{3.90}$$

which can be used to define the *t2* time function in respect to time *t1* as follows:

$$t_{2,k} - t_{1,k} = \frac{v_{C2,k}}{v_{C1,k}} \cdot t_{1,k}. \tag{3.91}$$

The average current that is charging capacitor *C2*is defined by the equation below:

$$i_{\mathrm{C2\_avg},k} = \frac{i_{max,k} \cdot \left(t_{2,k} - t_{1,k}\right)}{2 \cdot T_{sw}}, \tag{3.92}$$

which can be used together with (3.89) and (3.91) to define the control law for hard switched balancing circuit during DCM inductor's mode:

$$t_{1\_DCM,k} = \frac{\sqrt{i_{C2\_avg.k} \cdot 2 \cdot L_B \cdot T_{sw} \cdot v_{C1,k}}}{v_{C2,k}}. \tag{3.93}$$

The time representing the boundary conduction time is obtained from (3.91) by substituting t_2 with the switching period T_{sw}:

$$t_{1cr,k} = \frac{v_{C1,\mathrm{k}}}{v_{C1,\mathrm{k}} + v_{C2,\mathrm{k}}} \cdot T_{sw}, \tag{3.94}$$

identifying critical time for the balancing circuit, above which inductor's current enters CCM, during which transistor's conduction time should be kept equal to the critical conduction time. In the moment, when reference value changes, another time calculation equation should be used in order to track the reference current:

$$t_{1\_CCM,k} = \frac{\Delta I_{B_{ref},k} \cdot L_B + v_{C1,k} \cdot T_{sw}}{v_{C1,k} + v_{C2,k}}. \tag{3.95}$$

The diagram below represents the performance of obtained algorithm for hard-switched balancing circuit, demonstrating precise step responses on reference signal changes.

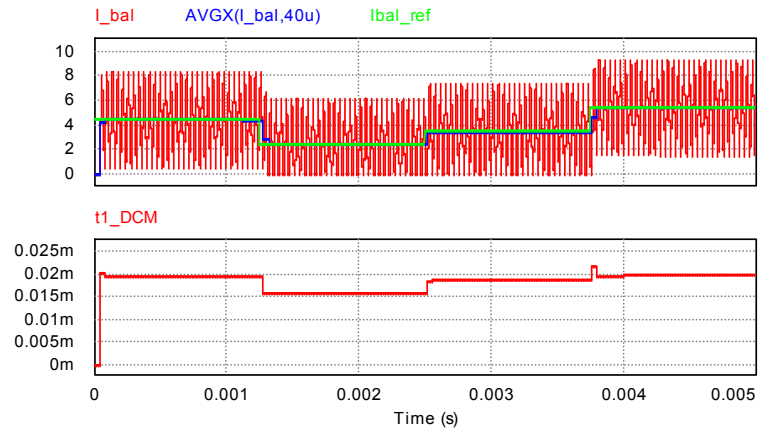

Fig. 3.43. Simulation results of control algorithm for hard-switched balancing circuit

3.7.2 Soft-switched balancing circuit

The soft-switched balancing circuit uses a resonant bank as energy storage and four semiconductor switches, controlling *SB3* and *SB4* during energy transfer from

capacitor *C2* to capacitor *C1*, while *SB1* and *SB2* are represented by their diodes (see Fig. 3.44). Reversed energy transfer is possible commutating the switches *SB1* and *SB2*.

SB4 transistor is conducting, resonant tank is being charged from *C2*

SB3 transistor is conducting, stored energy in resonant tank is released to *C1*

Fig. 3.44. Commutated current paths during direct power flow of converter discharging capacitor *C2* and charging capacitor *C1*

The energy stored in the resonant bank is equal to the energy of the charged resonant capacitor at the end of half-period:

$$E_{LC,k} = \frac{C \cdot v_{CB\_max,k}^2}{2}, \tag{3.96}$$

while resonant inductor should be selected in order to provide resonant frequency supplying half of the output load. The inductance of the resonant inductor can be obtained from:

$$f_{LC} = \frac{1}{2\pi\sqrt{LC}}. \tag{3.97}$$

The table below contains parameters of resonant balancing circuit with calculated values of maximal power flow, amplitude current, and resonant frequency.

Table 3.1

Parameter of resonant balancing circuitry

Combination of passive components	C_B [nF]	L_B [uH]	f_{res}[kHz]	*I_M [A]	*P [W]
I	75	540	25	4.7	600
II	68	560	25.8	4.4	544
III	82	470	25.6	5.3	656

* - calculated for 25 kHz operation, $V_{C2}(0)$=400 V

The first combination of passive components was calculated for 600 W of balancing power, while second and third combinations were selected out of standard nominal values for passive components. Slightly higher resonant frequency is admissible, as time reservation for dead-band should be taken into account.

The diagrams below demonstrate the performance of balancing circuit for the second solution from the Table 3.1, showing almost linear growth of transferred power depending on the voltage of discharging capacitor – the higher is the voltage, the higher power is transferred. Thus, the regulation of transferred energy depends on delays that are inserted between the switching periods and by controlling the voltage of discharging capacitor.

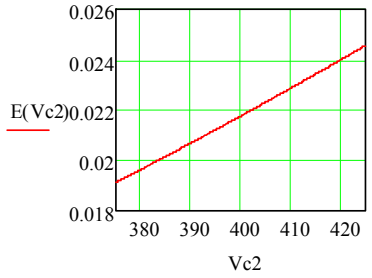

Energy transferred during single switching period as a function of capacitor *C2* voltage

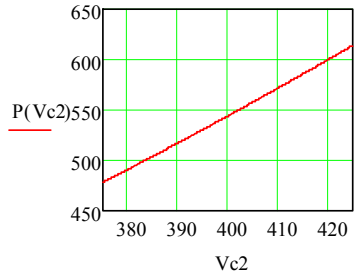

Rated power as a function of capacitor *C2* voltage

Fig. 3.45. Performance of resonant balancing circuit (C_B=68 nF, L_B=560 uH, f_{sw}=25 kHz)

3.7.3 Controller for balancing circuit

During the operation of front-end half-bridge converter the capacitors' voltages change in accordance with (3.22), meaning that during the period of input voltage the capacitors' voltages difference is proportional to front-end reference signal amplitude scaled by capacitance, angle speed, and cosine function raised above zero. Thus, the compensation of these changes should be taken into account in balancing circuit controller (see Fig. 3.46).

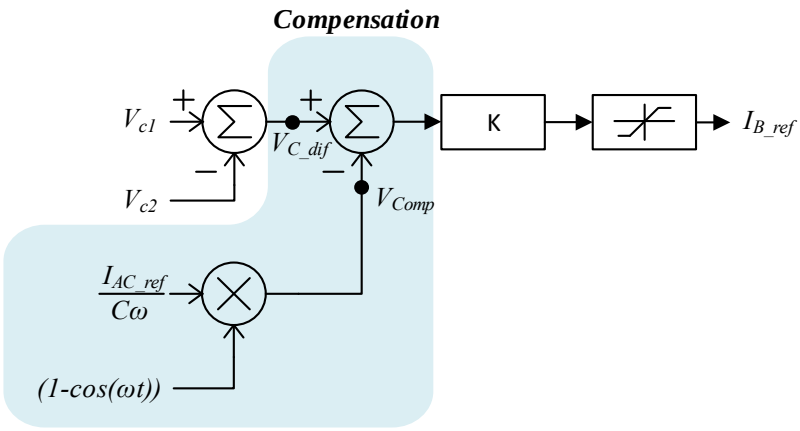

Fig. 3.46. Schematic of controller for balancing circuit

The performance of designed balancing circuit controller is seen in the Fig. 3.47, where the top graph contains the converter-side inductor's current controlled by PI regulator, which controls internal DC link voltage set to 800 V. The second graph from the top contains capacitors' *C1* and *C2* voltages. The third graph demonstrates capacitors' voltages differences and value of compensator, which is equal to capacitors' voltages difference, while the input current has equal amplitude of positive and negative half-periods. When the internal DC link voltage approached the reference value, the PI regulator of front-end active rectifier decreased the control value, resulting in uneven amplitudes of consumed current by half-periods, that produced changes between compensator value and capacitors' voltages difference. As a result, the control value of balancing circuit (see bottom graph of Fig. 3.47) controller appeared at 0.04 s, starting to transfer energy from capacitor *C1* to *C2*.

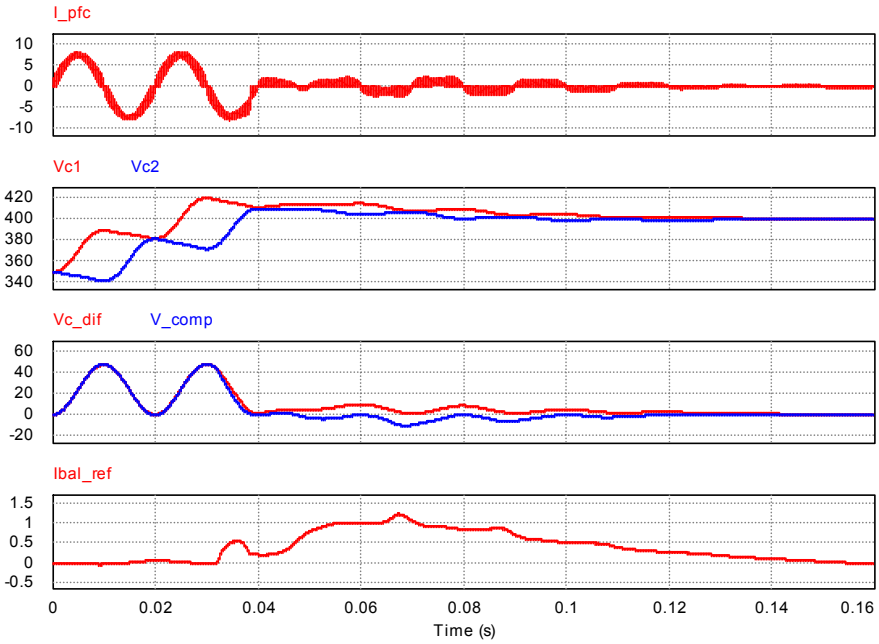

Fig. 3.47. Simulation result of balancing circuit controller

3.8 Output DC/DC converter

The output half-bridge DC/DC circuitry is controlled by two transistors – *S3,* which controls direct power flow from AC to DC side, and *S4*, which is responsible for reversed power flow. The current paths for direct power flow are presented in the Fig. 3.48.

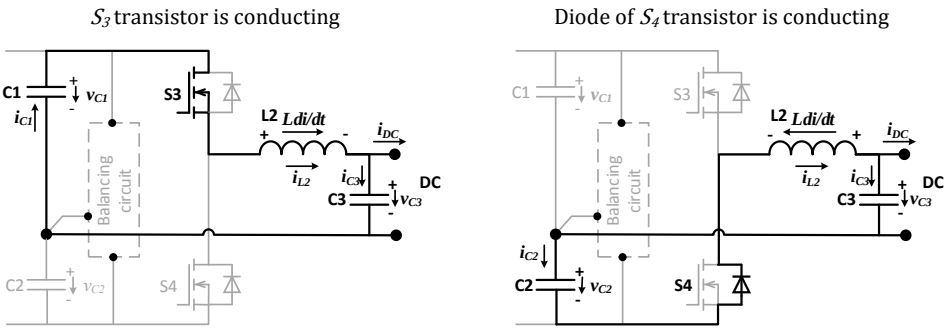

Fig. 3.48. Current paths in output DC/DC half-bridge for direct power flow

$$t_{1\_DCM,k} = \sqrt{\frac{I_{DC\_ref} \cdot 2 \cdot L_2 \cdot T_{sw} \cdot \left(v_{C2,k} + v_{DC,k}\right)}{\left(v_{C1,k} - v_{DC,k}\right) \cdot \left(v_{C1,k} + v_{C2,k}\right)}}. \tag{3.98}$$

In order to control the current during CCM period, the following time calculation equation should be used, where the second part represents the time, which corresponds to boundary conduction mode, but the first part has small contribution to transistor's conduction time, when the DC current reference value is being changed:

$$t_{1\_CCM,k} = \frac{\Delta I_{DC\_ref,k} \cdot L_2}{v_{C1,k} + v_{C2,k}} + \frac{\left(v_{C2,k} + v_{DC,k}\right) \cdot T_{sw}}{v_{C1,k} + v_{C2,k}}. \tag{3.99}$$

3.9 LCL filter calculation

As it was observed in the previously made simulations the current consumed or generated into the grid hardly reminds a sinusoid because of a high amount of higher harmonics located near converter's switching frequency. The LCL filter (see Fig. 3.49) commonly is used for reduction of harmonics that require special care of calculation keeping a trade-off between quality of input current and dimensions of the filter, which are also proportional to the filter's price.

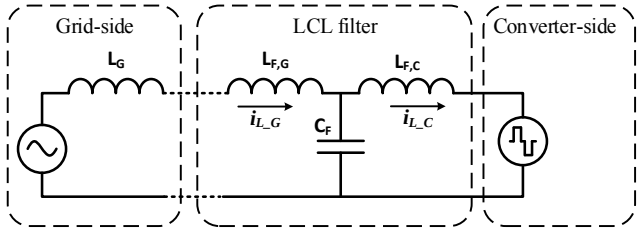

Fig. 3.49. Schematic of LCL filter

The converter-side inductor is selected in accordance with the admissible current ripple, which is defined by capacitor used in converter. The ALC10A471DF450 capacitor is considered to be used in AC/DC converter with 4.03 A of allowed current ripple [76]. Thus, the converter-side inductor can be selected by using boost converter's inductance selection equation [74]:

$$L_{F2} = \frac{\left(v_{C2,k} + v_{AC,k}\right) \cdot D_k}{f_{sw} \cdot \Delta I_{ripple}}. \tag{3.100}$$

The maximal duty cycle occurs between 40thand 50th switching periods (see Fig. 3.22), which is equal to 35% and results in the following:

$$L_C = \frac{\left(375 + 311\, sin\left(\frac{45}{250}\pi\right)\right) \cdot 0.35}{25000 \cdot 3.5} = 2.2\ mH. \tag{3.101}$$

The filter capacitor is selected in order to shunt higher harmonic currents with the capacitor branch, selecting impedance of the capacitor, which is lower than grid-side inductor's impedance (about 1/10 or 1/5 of X_{L_G}):

$$X_{CF} \approx \left(\frac{1}{10}\ to\ \frac{1}{5}\right) X_{L_G}. \tag{3.102}$$

If the constraint is not fulfilled and capacitor impedance is comparable with the grid side inductor's impedance, the filter capacitor will not be able to shunt enough the current ripple and more distorted current will be injected to the grid. On the other hand, the bigger capacitance will result in increased reactive power flow. The reactive power limit is usually selected below 5% of the system rated power[77]. Thus, the capacitance limitis defined as:

$$C_F \leq 0.05 \frac{P}{2\pi \cdot f_{AC} \cdot V_{AC}^2}, \tag{3.103}$$

where $V_{AC}$is RMS value of input voltage, $P$is rated power, f_{ac} grid's frequency. The $C_F$value of 1.6 μF is selected for 1 kW converter, which corresponds to 2.5% of rated converter's base impedance.

Another constraint is related to the self-resonance frequency of LCL filter [78], which is defined by the following equation:

$$f_{res} = \frac{1}{2\pi} \sqrt{\frac{L_G + L_C}{L_G \cdot L_C \cdot C_F}}. \tag{3.104}$$

The resonant frequency should match the following constraint:

$$10 \cdot f_{AC} < f_{res} < \frac{1}{2} f_{sw}. \tag{3.105}$$

Selection 0.2 mH for grid-side inductor both constraints ((3.102) and (3.105)) are fitted, as grid-side inductor's impedance is tenfold in comparison with the selected filter capacitor impedance and LCL filter's resonance frequency (6 kHz) is located within the defined range (10*50 Hz <f_{res}< 25/2 kHz).

Special consideration should given in order to use the previously obtained control laws for converter's operation with LCL filter. In the DCM mode only converter-side inductor should be taken into account to calculate the transistor's duty cycle for rectification and grid-tied inverter modes using equations (3.43) and (3.59)

correspondingly. During CCM the total inductance of the LCL filter should be considered in the equations (3.47) and (3.62), by which the transistor's conduction time is calculated for rectification and grid-tied inverter modes correspondingly. The stand-alone inverter's mode with LCL filter should be treated as grid-tied inverter mode, as the current waveforms are similar to grid-tied inverter mode due to filter capacitor.

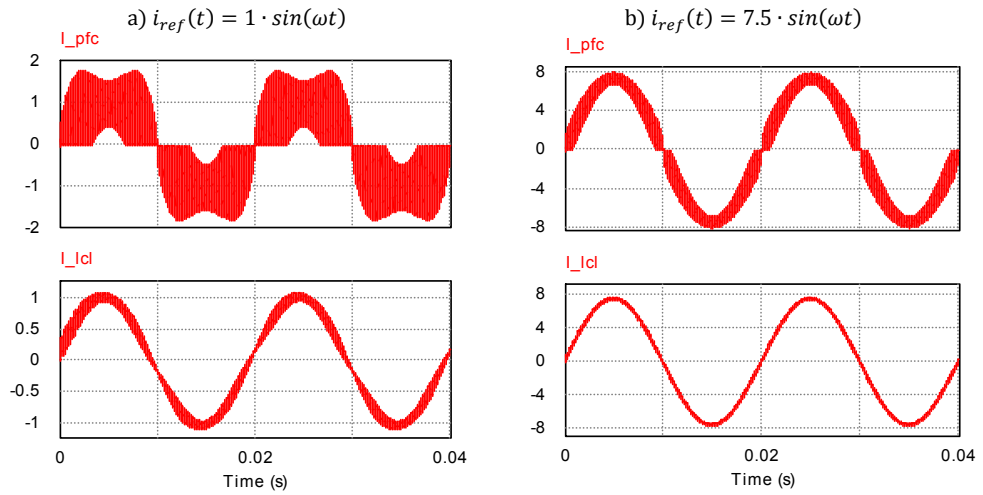

Fig. 3.50. Simulations results of LCL filter performance during converter's rectification mode (L_C=2.2mH, C_F=1.6uF, L_G=0.2mH)

The following table contains converter-side and grid-side inductors' current THD values obtained by the simulation in PSIM at different input current reference values.

Table 3.2

Performance of LCL filter

	I_M [A]	7.5	5	2.5	1	0.5
Rectification mode	THD(I_{L_C}) [%]	13.6	19.5	34.9	67.3	101.2
	THD(I_{L_G})[%]	1.8	2.7	4.5	8.2	11.5
Inverter mode	THD(I_{L_C}) [%]	12.1	17.7	32.4	63.8	96.1
	THD(I_{L_G})[%]	1.7	2.5	4.4	8.2	11.5

The data presented in Table 3.2 acknowledges the performance of LCL filter that operates with less than 11.5% starting with 10% of rated power. The selected values of LCL filter provide admissible THD values, also regulated by IEC61727 [79], which limits THD value for grid-tied inverters to be less than 5% at 75% of rated power.

3.10 Analysis of losses

In order to calculate the losses for the proposed converter the positive half-period of input voltage was analysed for front-end half-bridge converter in accordance with the methodology [80][81][82][83]. The balancing circuit and the output half-bridge were analysed by accumulating energy losses that occur in single switching period.

IGBT's and diodes' conduction losses were calculated by using RMS currents and linearized forward characteristics in accordance to parameters available from the datasheets. Switching losses were estimated proportionally to the current value at the moment of switching and energy losses at 100°C obtained from the technical notes[84][85][86]. Reverse recovery charge of the diode has been taken into account and multiplied by blocking voltage.

The diagrams below represent distribution of switching and conducting losses of transistor *S2* and reverse blocking diode of *S1* for front-end half-bridge over the half-period of input voltage.

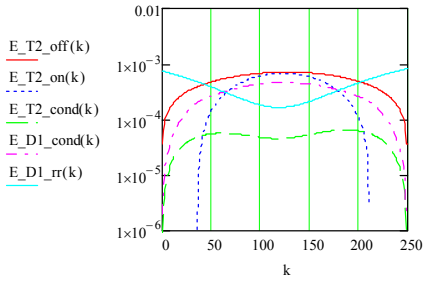

a) IGBT (IKW25N120H3)

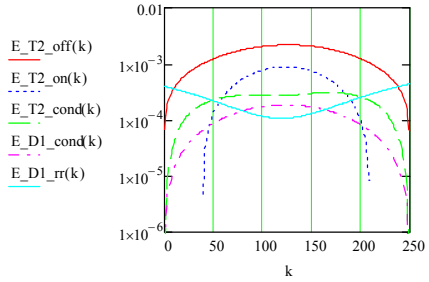

b) MOSFET (IXFH18N90P)

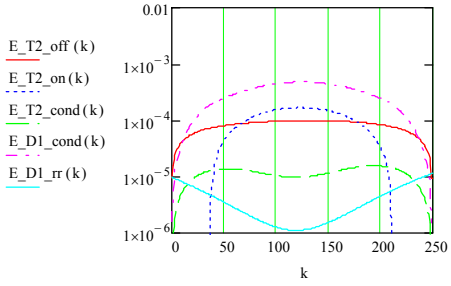

c) SJT (GA06JT12-247) and SiC Shotkey diode (C4D08120A)

Fig. 3.51. Graphical representation of energy losses for front-end AC/DC converter (I_M=7.5 A)

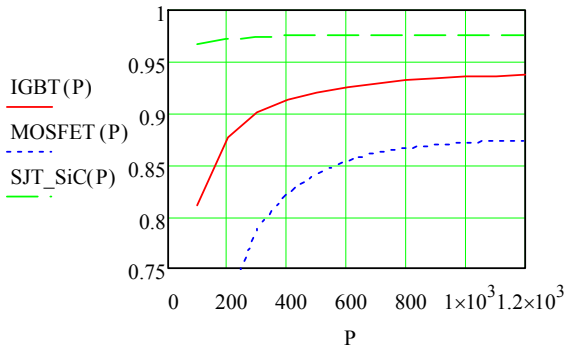

Fig. 3.52. Converter's overall efficiency estimated analytically for different types of transistors (IGBT - IKW25N120H3, MOSFET - IXFH18N90P, SJT_SiC - GA06JT12 and C4D08120A)

The performed loss analysis revealed IKW25N120H3 transistors as an optimal solution for initial tests, with a high potential to increase efficiency by using SJT GA06JT12-247 with C4D08120A SiC Shottkey diodes. Low reverse recovery charge helps to keep efficiency high at low power levels, as this type of energy losses remains almost constant at different power ratings. Relatively high reverse recovery charge is mainly responsible for efficiency drop for IGBT and MOSFET transistors at low power, as their diodes have tenfold reverse recovery charge in comparison with SiC diode.

3.11 Summary

In this chapter the following has been obtained:

1. Transformerless bidirectional AC/DC converter based on double half-bridge converter with non-commutated neutral wire has been proposed for intelligent grid applications as a common point interface between AC and DC grids;
2. Constant switching frequency average current sensorless control technique for converter's rectification, grid-tied, and stand-alone inverter modes both for DCM and CCM periods of converter-side inductor has been defined analytically and evaluated by PSIM simulations, showing identical results;
3. The definitions of current limits for adaptive hysteresis control during CCM period have been made, providing smooth transition of amplitude of peak

current between DCM and CCM periods operating at a nearly constant switching frequency;

4. LCL filter has been calculated for reduction of harmonic distortion that provides a good performance in a wide range of input power due to constant frequency of transistors' switching technique;
5. Defined switching technique has been adopted for use with LCL filter, defining that during DCM period only converter-side inductance should be taken into account, while during CCM period total filter inductance should be considered for control;
6. Stand-alone inverter mode with LCL input filter can be treated as grid-tied inverter mode, as filter capacitor helps converter-side inductor's current to raise and fall linearly, similarly like in grid-tied inverter mode;
7. Loss calculation approach based on a precise analytical model for evaluation of semiconductor components by its parameters available from the datasheets has been used for selection of semiconductor switches, where the SiC semiconductor components are the most promising ones due to fast switching performance and low reverse recovery charge of SiC diodes.

4 EXPERIMENTAL EVALUATION

In this chapter the experimental evaluation of the proposed control means is presented. The performance of multifunctional IS is described and bidirectional AC/DC is tested under different scenarios.

4.1 Experimental investigation of the proposed interconnection switch

Despite numerous publications covering non-intrusive load monitoring that describe different approaches to load identification, no descriptions deal with the problem of connected local generators, such as wind turbine or solar panels, and their generated power disaggregation and identification approaches, as they may be mismatched with loads variable in time.

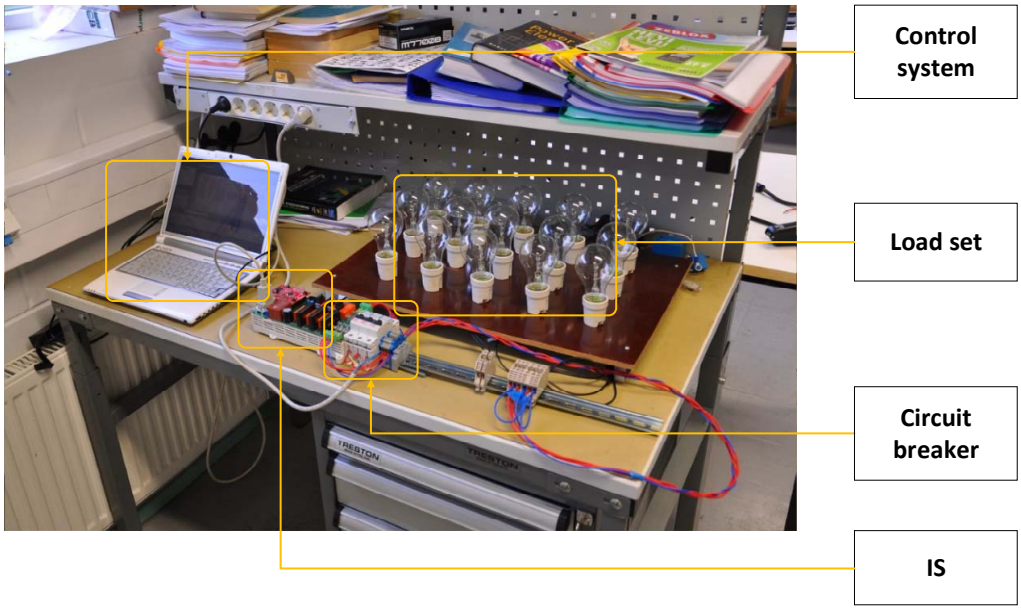

Fig. 4.1.Testbed for testing proposed IS

4.1.1 Testing NILM performance

Three approaches to electrical energy disaggregation, capable of extracting generated energy by a local renewable energy sources are described here.

Experiments with a meteorological sensor

The main challenge of this approach is to include the mathematical model of the renewable energy source and the corresponding converter reaction to the input parameter (solar radiation level or wind velocity) changes.

The experiment was held by using a controllable power source emulating a PV panel. The output power was controlled from LabVIEW in accordance to the transfer function (a simple PI regulator was used) of the PV panel and the converter under randomly generated solar radiation pattern.

, the disaggregation procedure, which is a result of inclusion of the set of loads and the transfer function of the PV panel into the IS internal logic, is presented in the table below.

Table 4.1

NILM performance with meteorological sensor

Element/Power	Real values	NILM values
Load 1 / 200 W	132,2 Wh	131,4 Wh
Load 2 / 100 W	76,1 Wh	74,7 Wh
Load 3 / 50-100 W	53,7 Wh	60,3 Wh
PV model / 250 W	-67,3Wh	-61,9 Wh

This approach requires precise definition of the transfer function of RES and the corresponding converter in order to obtain good disaggregation results.

Experiments with an additional current sensor

This approach is the easiest to implement as no software disaggregation algorithm is required, but hardware disaggregation is used to measure separate loads and sources. Assuming that a separate current sensor is used for each of the energy sources, there is no problem in implementation, except hardware limitation of the NILM device for connecting additional sensors. Energy disaggregation between the sources is required in case of multiple sources current monitoring with a single sensor. In this case combination of the present and the previous approach may help by defining separate transfer functions for each source and using additional meteorological sensors that have already proved their usability.

The proposed approach was evaluated by sensing current from a single source by an additional current sensor. The resulting disaggregation procedure is as precise as the measurement circuitry can ensure, having a total error less than 3% (see Table 4.2).

Table 4.2

NILM performance with spectral analysis

Element/Power	Real values	NILM values
Load 1 / 200 W	155,1Wh	158,4Wh
Load 2 / 100 W	99,5Wh	102,3Wh
Load 3 / 50-100 W	108,7Wh	110,8Wh
PV model / 250 W	-73,9Wh	-70,1Wh

Experiments with spectral analysis

The results of the experiment are presented in the table below. The error is higher – about 16% due to small THD changes at relatively high range of output power and limitation of the chosen CPU in calculation of THD. It should also be mentioned that connecting non-linear loads and additional sources will result in additional disturbances and complexity of the disaggregation procedure.

Table 4.3

NILM performance with spectral analysis

Element/Power	Real values	NILM values
Load 1 / 200 W	201,7Wh	197,8Wh
Load 2 / 100 W	139,5Wh	141,3Wh
Load 3 / 50-100 W	115,3Wh	139,4Wh
PV model / 250 W	-106,2Wh	-79,8Wh

4.1.2 Summary on NILM performance

Proposed solutions have different advantages and disadvantages summarized in the table below (see Table 4.4). The second approach (additional current sensors) may be the most attractive due to its highest disaggregation potential. Nevertheless, the last approach (spectral analysis) requires no additional hardware to be installed, but requires the highest computational performance, which may cause a change in the NILM device.

Table 4.4

Comparison of the proposed NILM solutions

Solution	Accuracy	Computational load	Additional hardware
Meteorological sensor	92%	Low	Yes
Current sensor	97%	Low	Yes
Spectral analysis	84%	High	No

4.2 Evaluation of short-term power balancing approaches

The short-term power balancing implements prioritized load supply that can be implemented either by DC bus signalling, or by means of communication, sending request to EMS.

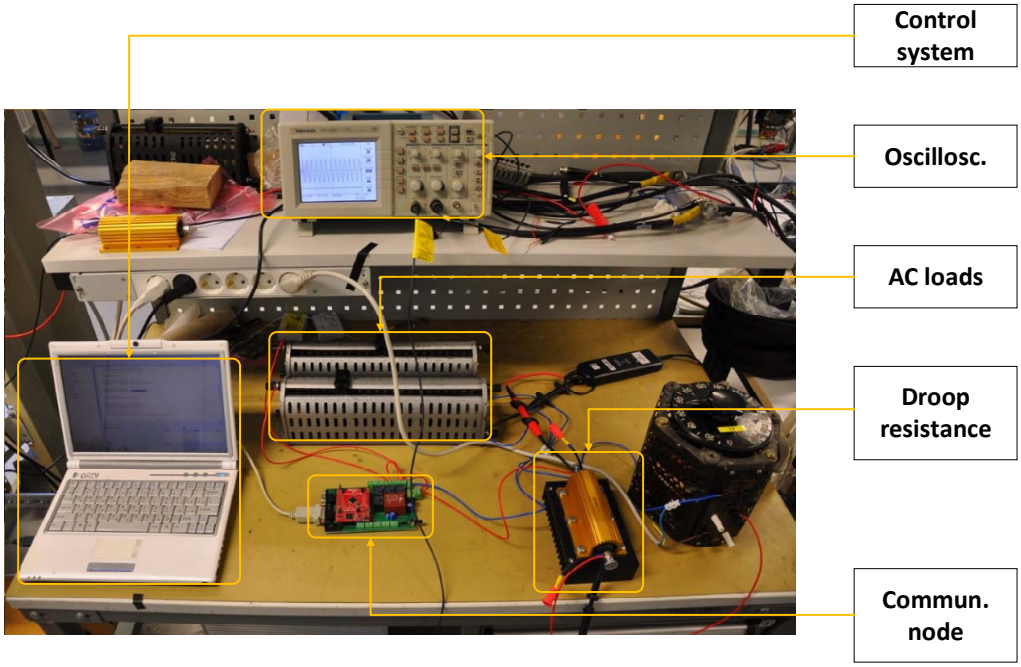

Fig. 4.2. Short-term power balancing testbed

AC bus signalling

The diagram below (see Fig. 4.3) demonstrates performance of the prioritized load supply using AC grid voltage levels, where the voltage amplitude 295 V is concerned as a threshold value.

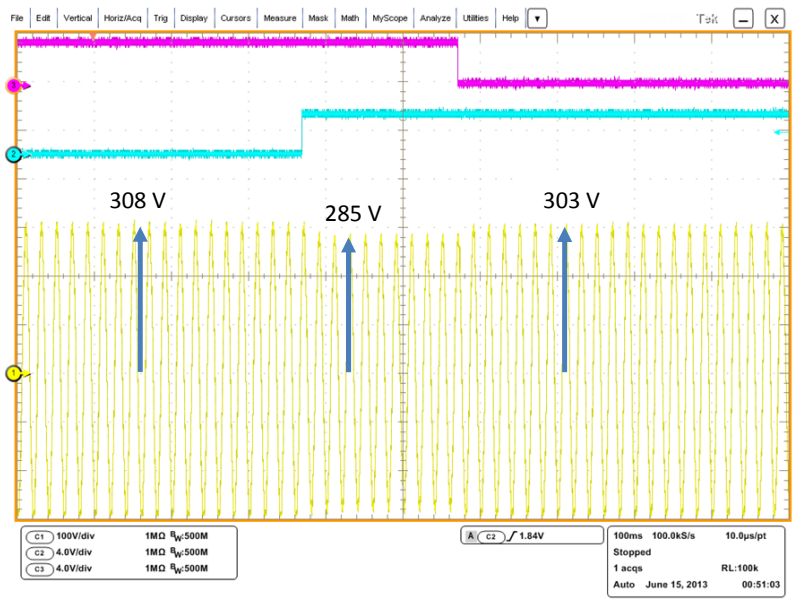

Fig. 4.3. Experimental waveforms of short-term power balancing with AC bus signalling

The low priority load was operating (channel 3), when voltage sag occurred by connecting higher priority load (channel 2), which initiated turn-off delay calculation. The communication node disconnected low priority load after turn-off delay had ended, which resulted in AC grid voltage normalization. The priority of the loads can be tuned by turn- off delays – the less important is the load, the shorter is the turn-off delay.

With communication

The prioritized load supply with enabled communication eliminates voltage sags by disconnecting low priority load before switching more critical load, as it is demonstrated in the diagram below (see Fig. 4.4).

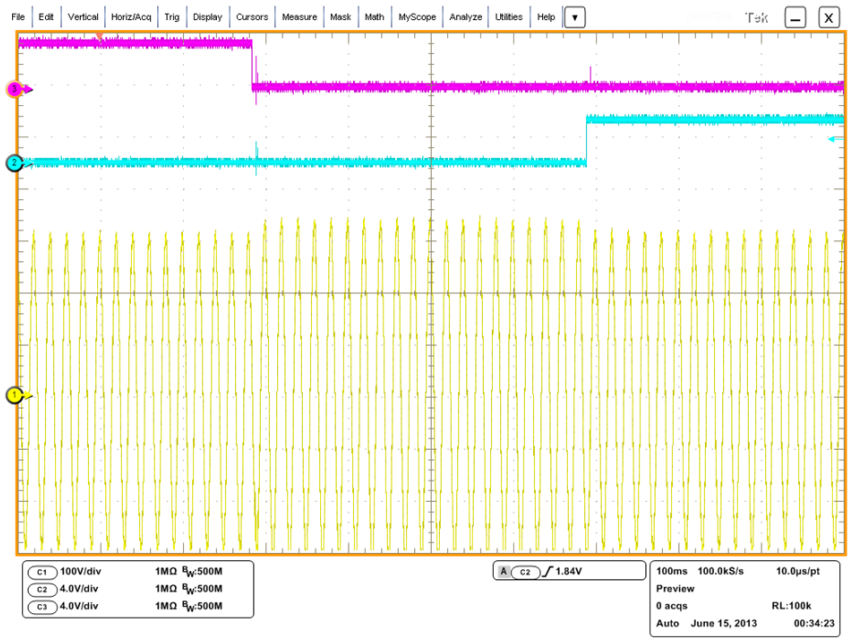

Fig. 4.4. Experimental waveforms of short-term balancing with communication

4.3 Experimental investigation of bidirectional AC/DC interface converter

The prototype of the proposed converter was built on two side PCB (70 µm of copper) with air cooling system represented by black radiator (250x200x25 mm), to which the transistors were attached using insulation sheet with improved thermal conductivity (see Appendix F). Each transistor's gate driver circuit had an isolated power supply (IK1215) and isolated driver integrated circuit (ACPL-H342) suitable for MOSFET and IGBT transistors. Four 560 µm inductors were connected in series in order to get 2 mH for grid-side inductor from the AC side. The balancing circuit was designed versatile, capable to test both hard-switched and soft-switched circuits.

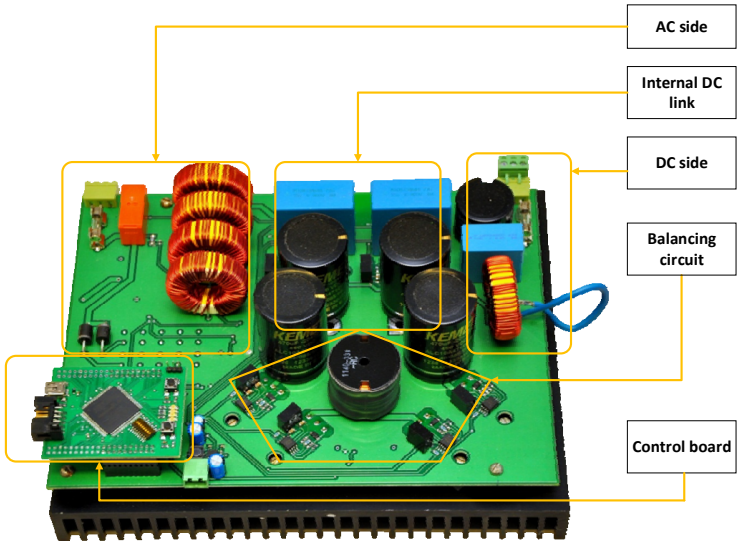

Fig. 4.5. Photo of proposed bidirectional AC/DC converter

The FPGA control board based on Altera Cyclone III family device (EP3C5E144C8N) (see Appendix G) is pin-to-pin compatible with LaunchPad Piccolo made by TI, which can be used as stack of control boards, where FPGA chip enhances computational performance of DSC.

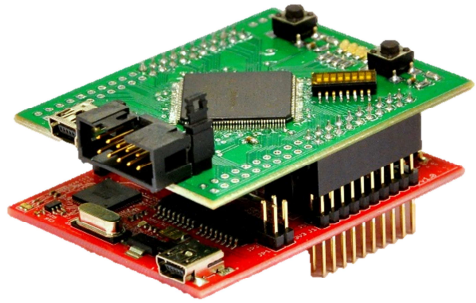

Fig. 4.6. FPGA-based control board

However, implementation of control law on Piccolo DSC was unacceptable due to limitation of built-in SPI interface, which resulted in reduction of practical ADC sample rate to about 25 kHz. That is why the custom SPI interface, as well as PWM modules for driving transistors accordingly to previously obtained control laws, was implemented on FPGA control board. Control algorithm calculated DCM and CCM conduction times choosing minimal value of both for driving transistors.

4.3.1 Testing PFC function

The performance of the elaborated bidirectional AC/DC converter was tested at a reduced input voltage to evaluate the proposed current sensorless control algorithm driven by FPGA control board (see Appendix H). The figure below (see Fig. 4.7) demonstrates the transition between disabled PFC function and enabled PFC function. As it can be noted, the current shape was improved with PF>0.97, however, the THD value (around 12%) was still poor, as the current sensorless control highly depended on calibration of analogue to digital converter measurements. To avoid hardware malfunctioning the following tests were performed by simulation.

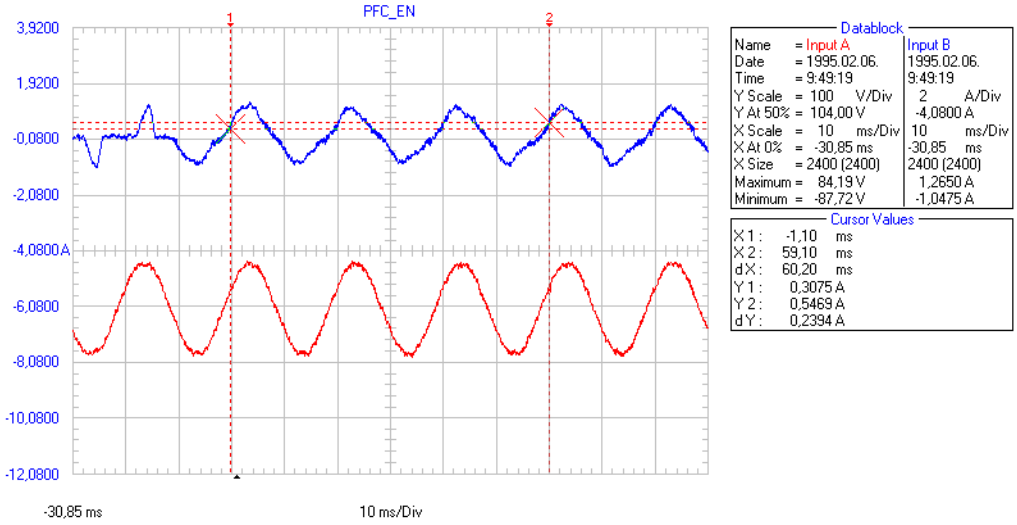

Fig. 4.7 Performance of the PFC function

4.3.2 Testing energy shortage

The energy flow direction from AC to DC grid was tested by connecting nominal load on DC grid. The figure below demonstrates the result of the simulation, demonstrating step response that occurred at time 0.01, resulting in DC bus voltage drop by 4% in relation to the reference value. The PI regulators of AC half-bridge, balancing circuit and output half-bridge circuits performed the action to stabilize the reference parameters, which are 800 V of internal DC link, 0 V capacitors' unbalance, and 300 V of output DC bus correspondingly. By the time 0.15 s all measured values were stabilized.

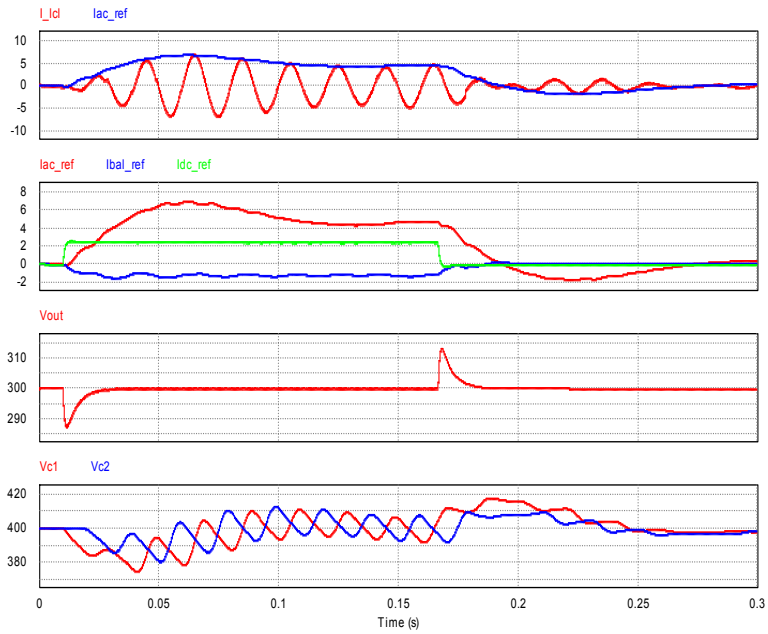

Fig. 4.8. Simulation results for energy shortage test

4.3.3 Testing energy excess

The energy flow direction from DC to AC grid was tested by connecting nominal 900 W source from DC grid side. The figure below demonstrates the result of the simulation, demonstrating step response, which occurred at the time 0.01, resulting in 3% DC bus voltage spike. Again, the all controllable parameters were stabilized in by the time 0.15 s. Then, the energy source was disconnected, resulting in DC bus voltage drop by 4%.

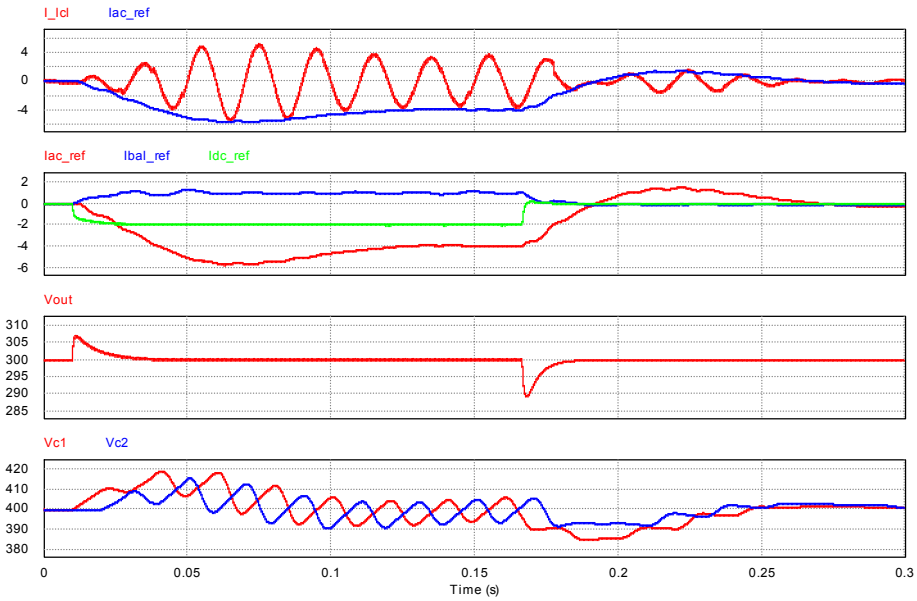

Fig. 4.9. Simulation results for energy excess test

4.3.4 Testing distorted input voltage condition

The simulation of distorted input voltage condition revealed resistance of the current control algorithm from input voltage harmonics, keeping to consume or generate (see Fig. 4.10 a) and b) respectively) sinusoidal current.

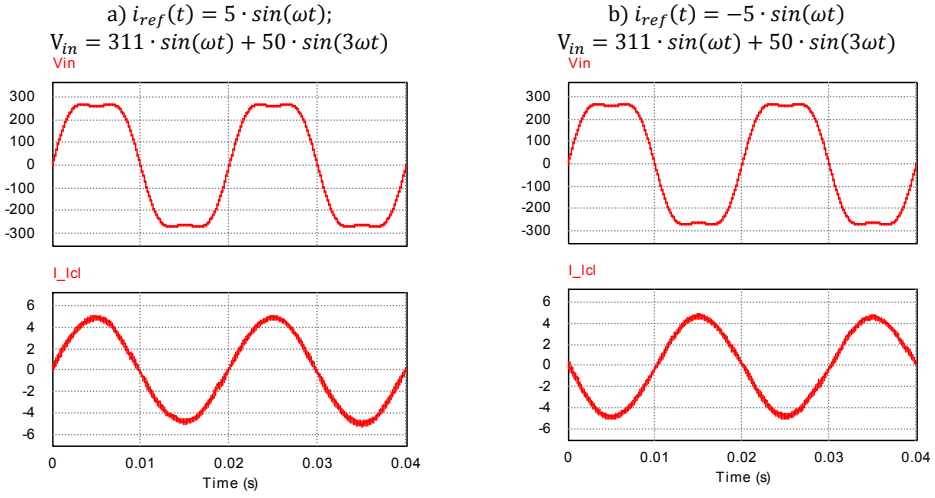

Fig. 4.10. Simulation results for distorted input voltage condition

The current form is shaped by means of internal sinusoidal reference signal, while instantaneous values of input voltage and capacitors' voltages are used to calculate required transistor conduction time that would properly shape the current. Thus, harmonic distortion on input voltage (THD_{Vin}=26.2%) did not influence the shape of the current (THD_{I_lcl}=3.5%).

This feature has a positive effect on the supply grid. The consumption of sinusoidal current during distorted input voltage increases the amplitude of base harmonic, consequently reducing THD of the utility grid's current. During inverter mode, the sinusoidal current form stabilizes grid's voltage.

4.4 Summary

In this chapter the following has been obtained:

1. Three NILM improvement algorithm approaches were proposed and evaluated in order to disaggregate the amount of energy generated by RES, where the additional current sensor provided the most accurate result.
2. The short-term power balancing responsible for the load prioritized supply has been implemented in two ways - with bus signaling approach and by means of communication equipment, where the last one performs without voltage sags.
3. The model of bidirectional AC/DC converter demonstrated good performance, stabilizing controlled parameters in 0.15 s at different step-responses.
4. Resistance from input voltage harmonic distortion was approved in rectifier and grid-connected inverter modes keeping current THD value at 3 % level, while THD of input voltage is above 26 %.
5. Comparison of the proposed switching algorithm to the other sensorless control methods is presented in the Table 4.5.It should be noted that none of the competitive methods define sensorless control in discontinuous current mode.

Table 4.5

Overview of different sensorless control techniques

		[87]	[88]	[89]	[90]	[91]	Proposed
Fixed switching frequency		√	√	√	√	√	√
Fixed-amplitude carrier		√	√	√			√
Current form	DCM						√
	CCM	√	√	√	√	√	√
Stable to harmonics distortion of input voltage			√			√	√
Current sensorless		√	√	√			√
Input voltage sensorless					√	√	

CONCLUSIONS

Analysis of an intelligent distribution grid (IDG) based on contemporary households that use renewable energy sources (RES) is made in the present thesis. The focus is made on improvement of control means that are used in the IDG for energy management. Finally, it can be concluded that defined hypothesis are confirmed, and objectives are achieved.

The multifunctional interconnection switch (IS) is being proposed for use. It combines functionality of multiple devices: an interconnection switch, a phase selector, and a non-intrusive load monitoring (NILM) device. The proposed product allows implementing the same functions with less electronic and mechanical switches, as well as less number of voltage and current sensors. In particular, the NILM function has been improved in order to enable disaggregation of energy generated by RES, having the best performance with 3% inaccuracy, if an additional current sensor is used for measurement of RES generated current.

New long-term energy management algorithm for IDG has been discussed. It was proposed to categorise electrical appliances into four groups: time-triggered, price-triggered, hybrid-triggered, and price-responsive loads. Based on that, scheduling of generators and energy storage components are obtained and load shifting and shedding is performed by defining the electricity price function, when IDG operates autonomously. In case if IDG is connected to a utility grid and the price function is defined by the network operator, the proposed algorithm enables demand-side management – desirable function for network operator to mitigate peak demand issues.

The use of DC subgrids has a significant impact on energy efficiency, reducing the losses to about 4-15% depending on power and grid configuration due to reduction of energy conversion count, as most of RES, energy storages, and most of the loads are DC by fact. For this reason, the bidirectional AC/DC interface converter based on dual half-bridge topology has been analysed. It uses 6 switches (twice less than DAB with full-bridge front-end rectifier) and does not use a transformer, as neutral wire does not commutate during proposed converter operation.

Average current sensorless control algorithm has been defined for half-bridge front-end bidirectional rectifier capable to operate at a constant switching frequency in different modes: rectification, grid-tied inverter and stand-alone inverter modes. It has

also been adopted for operation with LCL input filter. The proposed approach eliminates the need for input inductor's instantaneous current sensing that reduces the cost and size of the control system. Par excellence, the current form is resistant to input voltage harmonic distortion, improving THD of utility grid's current. The performance of the proposed current control algorithm with calculated LCL filter provided current THD value admissible for IEC61727 standard. More over, proposed current control method can be utilized in sensored application during low power modes, providing sinusoidal shape of averaged inductor current.

The future work will comprise the following activities: minimisation of the proposed communication node by integrating control and communication parts into a single device; adaptation of the proposed switching technique used in AC/DC converter supplying non-linear load; improvement of converter controller functionality with islanding detection and parallel inverter operation.

REFERENCES

[1] F. Birol, "Power to the people," *IAEA Bulletin*, vol. 46, no. June, pp. 9–12, 2004.

[2] Population Reference Bureau, "2012 World Population Data Sheet," pp. 1–20, 2012.

[3] A. McCrone, "Global Trends in Renewable Energy Investment 2012," 2012.

[4] S. Enkhardt, "Germany hits 32.6 GW cumulative PV capacity," 2013. [Online]. Available: http://www.pv-magazine.com/news/details/beitrag/germany-hits-326-gw-cumulative-pv-capacity_100010394/. [Accessed: 01-Jun-2013].

[5] M. Hoeven, "Technology Roadmap - Hydropower," CORLET, Paris, 2012.

[6] *PVPS Report A Snapshot of Global PV 1992-2012*. Paris, 2013, pp. 1–12.

[7] L. Fried, "Global wind statistics 2012," 2013.

[8] A. Lubbe, "Denmark reaches 2020-goal for solar energy before time," 2012. [Online]. Available: http://um.dk/en/news/newsdisplaypage/?newsID=25147B44-3DCE-4647-8788-AD9243C22DF2. [Accessed: 01-Dec-2012].

[9] L. Sollecito, "Smart Grid: The Road Ahead," *Protection and Control Journal*, pp. 15–19, 2009.

[10] R. H. Lasseter and P. Piagi, "Microgrid: A conceptual solution," *Power Electronics Specialists Conference, 2004. PESC 04. 2004 IEEE 35th Annual*, vol. 6, no. June, pp. 4285 – 4290, 2004.

[11] J. Schonberger, R. Duke, and S. D. Round, "DC-Bus Signaling: A Distributed Control Strategy for a Hybrid Renewable Nanogrid," *IEEE Transactions on Industrial Electronics*, vol. 53, no. 5, pp. 1453–1460, Oct. 2006.

[12] I. Cvetkovic, D. Dong, W. Zhang, L. Jiang, D. Boroyevich, F. C. Lee, and P. Mattavelli, "A testbed for experimental validation of a low-voltage DC nanogrid for buildings," in *2012 15th International Power Electronics and Motion Control Conference (EPE/PEMC)*, 2012, pp. LS7c.5–1–LS7c.5–8.

[13] P. Bertoldi and B. Atanasiu, "Electricity Consumption and Efficiency Trends in European Union," 2009.

[14] J. A. Jardini, C. M. V. Tahan, M. R. Gouvea, S. U. Ahn, and F. M. Figueiredo, "Daily load profiles for residential, commercial and industrial low voltage consumers," *IEEE Transactions on Power Delivery*, vol. 15, no. 1, pp. 375–380, 2000.

[15] R. H. Lasseter, “Smart Distribution: Coupled Microgrids,” *Proceedings of the IEEE*, vol. 99, no. 6, pp. 1074–1082, Jun. 2011.

[16] B. Droste-Franke, B. P. Paal, C. Rehtanz, D. U. Sauer, J.-P. Schneider, M. Schreurs, and T. Ziesemer, *Balancing Renewable Electricity*, 1 edition., vol. 40. Berlin, Heidelberg: Springer Berlin Heidelberg, 2012, p. 301.

[17] P. Palensky and D. Dietrich, “Demand Side Management: Demand Response, Intelligent Energy Systems, and Smart Loads,” *IEEE Transactions on Industrial Informatics*, vol. 7, no. 3, pp. 381–388, Aug. 2011.

[18] R. Bründlinger, “Inverter Technology enabling high penetration PV,” 2010.

[19] A. Suzdalenko, A. Stepanov, and I. Galkin, “Choice of power factor corrector for effective operation of MicroGrid and its elements,” in *2010 International School on Nonsinusoidal Currents and Compensation*, 2010, pp. 234–238.

[20] G.-S. Seo, J. Baek, K. Choi, H. Bae, and B. Cho, “Modeling and analysis of DC distribution systems,” in *8th International Conference on Power Electronics - ECCE Asia*, 2011, pp. 223–227.

[21] K. Shenai and K. Shah, “Smart DC micro-grid for efficient utilization of distributed renewable energy,” in *IEEE 2011 EnergyTech*, 2011, pp. 1–6.

[22] A. Suzdalenko and I. Galkin, “Advantages of enhancement of Street Lighting Infrastructure with DC link,” in *2012 13th Biennial Baltic Electronics Conference*, 2012, pp. 235–238.

[23] H. Kakigano, M. Nomura, and T. Ise, “Loss evaluation of DC distribution for residential houses compared with AC system,” *The 2010 International Power Electronics Conference - ECCE ASIA -*, pp. 480–486, Jun. 2010.

[24] S. Darby, “The Effectiveness of Feedback on Energy Consumption - A Review for DEFRA of the Literature on Metering, Billing and Direct Displays,” *Change*, vol. 22, no. April, pp. 33–35, Apr. 2006.

[25] K. Ehrhardt-Martinez, K. Donnelly, and S. Laitner, “Advanced metering initiatives and residential feedback programs: a meta-review for household electricity-saving opportunities,” *Energy*, 2010.

[26] H. Kim, M. Marwah, M. Arlitt, and G. Lyon, “Unsupervised disaggregation of low frequency power measurements,” *Conference on Data*, no. i, pp. 747–758, 2010.

[27] H. Kanchev, D. Lu, F. Colas, V. Lazarov, and B. Francois, “Energy Management and Operational Planning of a Microgrid With a PV-Based Active Generator for Smart

Grid Applications," *IEEE Transactions on Industrial Electronics*, vol. 58, no. 10, pp. 4583–4592, Oct. 2011.

[28] J. Bryan, R. Duke, and S. Round, "Decentralized generator scheduling in a nanogrid using DC bus signaling," in *Power Engineering Society General Meeting, 2004. IEEE*, 2004, pp. 977 – 982 Vol.1.

[29] J. Kemmerer and N. W. Biege, "Control system retrofits — The network is key," in *2012 IEEE-IAS/PCA 54th Cement Industry Technical Conference*, 2012, pp. 1–23.

[30] "Zigbee Alliance Home Page," 2008. [Online]. Available: http://www.zigbee.org/home.aspx. [Accessed: 01-Nov-2012].

[31] "Y-NET Protocol Stack Overview." Beer Sheva, p. 28, 2009.

[32] D. Olivares, "A centralized optimal energy management system for microgrids," *Power and Energy …*, pp. 1–6, 2011.

[33] "PL 3120 and PL 3150 Power Line Smart Transceivers." p. 13, 2005.

[34] A. Suzdalenko and I. Galkin, "Investigation of power supply methods for intelligent LED luminary," in *Proceedings of 14th International Power Electronics and Motion Control Conference EPE-PEMC 2010*, 2010, pp. 331–334.

[35] S. Bradbury, "HomePlug Command & Control (C&C) Overview White Paper," no. September 2008. pp. 1–9, 2008.

[36] A. Suzdalenko, M. Vorobyov, and I. Galkin, "Development of Distributed Energy Management System for Intelligent Household Electricity Distribution Grid," in *Proceedings of EuroCon 2013*, 2013, no. July, pp. 1474–1478.

[37] M. Mao, Y. Tao, L. Chang, Y. Zhao, and P. Jin, "An intelligent static switch based on embedded system and its control method for a microgrid," in *IEEE PES Innovative Smart Grid Technologies*, 2012, pp. 1–6.

[38] ABB, "The new SACE Emax 2 family of air circuit-breakers The evolution from circuit-breaker to power manager," *Power and productivity for a better world*. [Online]. Available: http://www05.abb.com/global/scot/scot209.nsf/veritydisplay/d01299d7e0bcb8d6c1257b48004f6674/$file/1SDC200025R0201.pdf. [Accessed: 01-Apr-2013].

[39] G. W. Hart, E. C. J. Kern, and F. C. Shweppe, "Non-intrusive appliance monitor apparatus," 48581411989.

[40] A. Suzdalenko and I. Galkin, “Case Study on Using Non-intrusive Load Monitoring System with Renewable Energy Sources in Intelligent Grid Applications,” in *Compatibility and Power ELectronics, 2013 8th International*, 2013, pp. 115–119.

[41] J. F. Martins, R. Lopes, C. Lima, E. Romero-Cadaval, and D. Vinnikov, “A novel nonintrusive load monitoring system based on the S-Transform,” in *2012 13th International Conference on Optimization of Electrical and Electronic Equipment (OPTIM)*, 2012, pp. 973–978.

[42] Z. Remscrim, J. Paris, S. B. Leeb, S. R. Shaw, S. Neuman, C. Schantz, S. Muller, and S. Page, “FPGA-based spectral envelope preprocessor for power monitoring and control,” in *2010 Twenty-Fifth Annual IEEE Applied Power Electronics Conference and Exposition (APEC)*, 2010, pp. 2194–2201.

[43] S. B. Leeb, S. R. Shaw, and J. L. Kirtley, “Transient event detection in spectral envelope estimates for nonintrusive load monitoring,” *IEEE Transactions on Power Delivery*, vol. 10, no. 3, pp. 1200–1210, Jul. 1995.

[44] C. Laughman, R. Cox, S. Shaw, S. Leeb, L. Norford, and P. Armstrong, “Power signature analysis,” *IEEE Power and Energy Magazine*, vol. 1, no. 2, pp. 56–63, Mar. 2003.

[45] S. P. Kamat, “Fuzzy logic based pattern recognition technique for non-intrusive load monitoring,” in *2004 IEEE Region 10 Conference TENCON 2004.*, 2004, vol. C, pp. 528–530 Vol. 3.

[46] K. Suzuki, S. Inagaki, T. Suzuki, H. Nakamura, and K. Ito, “Nonintrusive appliance load monitoring based on integer programming,” in *2008 SICE Annual Conference*, 2008, vol. 174, no. 2, pp. 2742–2747.

[47] M. Baranski and J. Voss, “Detecting Patterns of Appliances from Total Load Data Using a Dynamic Programming Approach,” in *Fourth IEEE International Conference on Data Mining (ICDM’04)*, 2004, pp. 327–330.

[48] H.-H. Chang, P.-C. Chien, L.-S. Lin, and N. Chen, “Feature Extraction of Non-intrusive Load-Monitoring System Using Genetic Algorithm in Smart Meters,” in *2011 IEEE 8th International Conference on e-Business Engineering*, 2011, pp. 299–304.

[49] A. Suzdalenko and I. Galkin, “Evaluation of Power Consumption Minimization Approaches for Autonomous Electronic Equipment,” *Scientific Journal of Riga*

Technical University. Power and Electrical Engineering, vol. 29, no. 1, pp. 101–104, Jan. 2011.

[50] P. Piagi and R. H. Lasseter, "Autonomous control of microgrids," in *2006 IEEE Power Engineering Society General Meeting*, 2006, p. 8 pp.

[51] J. M. Guerrero, J. C. Vasquez, J. Matas, L. G. de Vicuna, and M. Castilla, "Hierarchical Control of Droop-Controlled AC and DC Microgrids—A General Approach Toward Standardization," *IEEE Transactions on Industrial Electronics*, vol. 58, no. 1, pp. 158–172, Jan. 2011.

[52] J. Schonberger, S. Round, and R. Duke, "Autonomous Load Shedding in a Nanogrid using DC Bus Signalling," in *IECON 2006 - 32nd Annual Conference on IEEE Industrial Electronics*, 2006, pp. 5155–5160.

[53] Y. Jaganmohan Reddy, Y. V Pavan Kumar, V. Sunil Kumar, and K. Padma Raju, "Distributed ANNs in a layered architecture for energy management and maintenance scheduling of renewable energy HPS microgrids," in *2012 International Conference on Advances in Power Conversion and Energy Technologies (APCET)*, 2012, no. 1, pp. 1–6.

[54] T. Logenthiran and D. Srinivasan, "Short term generation scheduling of a Microgrid," in *TENCON 2009 - 2009 IEEE Region 10 Conference*, 2009, pp. 1–6.

[55] T. Ikegami, Y. Iwafune, and K. Ogimoto, "Optimum operation scheduling model of domestic electric appliances for balancing power supply and demand," in *2010 International Conference on Power System Technology*, 2010, pp. 1–8.

[56] "35kV and below Interconnection Requirements for Power Generators," no. May, 2010.

[57] A. Suzdalenko and I. Galkin, "Comparison of two power electronic schemes for 3 kW Li-Ion battery charger," in *2011 7th International Conference-Workshop Compatibility and Power Electronics (CPE)*, 2011, pp. 400–403.

[58] A. Suzdalenko, I. Milashevski, and I. Galkin, "Comparative study of smart lighting grids with LEDs operated with concentrated, localized or distributed control," in *International Symposium on Power Electronics Power Electronics, Electrical Drives, Automation and Motion*, 2012, pp. 1437–1441.

[59] A. Suzdalenko and I. Galkin, "Instantaneous, Short-Term and Predictive Long-Term Power Balancing Techniques in Intelligent Distribution Grids," in in *Technological Innovation for the Internet of Things SE - 37*, vol. 394, L.

Camarinha-Matos, S. Tomic, and P. Graça, Eds. Lisbon: Springer Berlin Heidelberg, 2013, pp. 343–350.

[60] J.-H. Jung, H.-S. Kim, M.-H. Ryu, and J.-W. Baek, "Design Methodology of Bidirectional CLLC Resonant Converter for High-Frequency Isolation of DC Distribution Systems," *IEEE Transactions on Power Electronics*, vol. 28, no. 4, pp. 1741–1755, Apr. 2013.

[61] A. Suzdalenko and I. Galkin, "[accepted for publication]Current Sensorless Control of Front-end Bidirectional AC/DC Converter Based on Half-bridge Topology," *Electrical, Control and Communication Engineering*, vol. 4, no. 1, pp. 1–7, Jan. 2013.

[62] L. Rossetto, G. Spiazzi, and P. Tenti, "Control techniques for power factor correction converters," in *Proc. PEMC'94*, 1994, pp. 1–9.

[63] N. Mohan, T. M. Undeland, and W. P. Robbins, *Power Electronics: Converters, Applications, and Design*, 3 edition. Wiley, 2002, p. 824.

[64] M. P. Kazmierkowski and L. Malesani, "Current control techniques for three-phase voltage-source PWM converters: a survey," *IEEE Transactions on Industrial Electronics*, vol. 45, no. 5, pp. 691–703, 1998.

[65] T. Narongrit, K. Areerak, and K. Areerak, "The Comparison Study of Current Control Techniques for Active Power Filters," *Word Academy of Science, Engineering and Technology*, vol. 60, pp. 471–476, 2011.

[66] H. Choi, "Interleaved Boundary Conduction Mode (BCM) Buck Power Factor Correction (PFC) Converter," *IEEE Transactions on Power Electronics*, vol. 28, no. 6, pp. 2629–2634, Jun. 2013.

[67] T. Qi, L. Xing, and J. Sun, "Dual-Boost PFC Converter Control Without Input Current Sensing," in *2009 Twenty-Fourth Annual IEEE Applied Power Electronics Conference and Exposition*, 2009, pp. 1855–1861.

[68] F. Javier Azcondo, A. de Castro, V. M. Lopez, and O. Garcia, "Power Factor Correction Without Current Sensor Based on Digital Current Rebuilding," *IEEE Transactions on Power Electronics*, vol. 25, no. 6, pp. 1527–1536, Jun. 2010.

[69] A. Garcia, A. de Castro, O. Garcia, and F. J. Azcondo, "Pre-calculated duty cycle control implemented in FPGA for power factor correction," in *2009 35th Annual Conference of IEEE Industrial Electronics*, 2009, pp. 2955–2960.

[70] S. Sivakumar, K. Natarajan, and R. Gudelewicz, “Control of power factor correcting boost converter without instantaneous measurement of input current,” *IEEE Transactions on Power Electronics*, vol. 10, no. 4, pp. 435–445, Jul. 1995.

[71] M. Rodriguez, V. M. Lopez, F. J. Azcondo, J. Sebastian, and D. Maksimovic, “Average Inductor Current Sensor for Digitally Controlled Switched-Mode Power Supplies,” *IEEE Transactions on Power Electronics*, vol. 27, no. 8, pp. 3795–3806, Aug. 2012.

[72] H. Chen, “Single-Loop Current Sensorless Control for Single-Phase Boost-Type SMR,” *IEEE Transactions on Power Electronics*, vol. 24, no. 1, pp. 163–171, Jan. 2009.

[73] H. Vahedi, A. Sheikholeslami, M. Tavakoli Bina, and M. Vahedi, “Review and Simulation of Fixed and Adaptive Hysteresis Current Control Considering Switching Losses and High-Frequency Harmonics,” *Advances in Power Electronics*, vol. 2011, pp. 1–6, 2011.

[74] R. Erickson and D. Maksimovic, *Fundamentals of power electronics*, 2nd editio. Springer, 2001, p. 912.

[75] M. Moazzam, A. Chakraborty, and M. Bhuiyan, “A Robust Method for Solving Transcendental Equations,” *International Journal of Computer Science Issues*, vol. 9, no. 6, pp. 413–419, 2012.

[76] “Specification of ALC10 Series,” 2000. [Online]. Available: http://www.e-sonic.com/whatsnew/FeaturedProducts/KEMET/SnapIn-Alum/F3304_ALC10.pdf.

[77] M. Liserre, F. Blaabjerg, and S. Hansen, “Design and Control of an LCL-Filter-Based Three-Phase Active Rectifier,” *IEEE Transactions on Industry Applications*, vol. 41, no. 5, pp. 1281–1291, Sep. 2005.

[78] F. Liu, X. Zha, Y. Zhou, and S. Duan, “Design and research on parameter of LCL filter in three-phase grid-connected inverter,” in *2009 IEEE 6th International Power Electronics and Motion Control Conference*, 2009, vol. 3, pp. 2174–2177.

[79] IEC61727, *Photovoltaic (PV) systems –Characteristics of the utility interface*. 2004, p. 23.

[80] A. Wintrich, U. Nicolai, W. Tursky, and T. Reimann, *Application Manual Power Semiconductors*. Ilmenau: ISLE Verlag, 2011, p. 464.

[81] D. Graovac, M. Purschel, and A. Kiep, “MOSFET power losses calculation using the data-sheet parameters,” *Application …*, no. July. p. 23, 2006.

[82] D. Jauregui, B. Wang, and R. Chen, “Power Loss Calculation with Common Source Inductance consideration for Synchronous Buck Converters,” 2011.

[83] “Selection Guide of SiC Schottky Diode in CCM PFC Applications.” p. 4, 2001.

[84] “Power MOSFET s IXFH18N90P Characteristic Values.” p. 5, 2011.

[85] “High speed DuoPack: IKW25N120H3.” p. 14, 2010.

[86] “Normally – OFF Silicon Carbide Super Junction Transistor GA06JT12-247.” p. 6, 2013.

[87] H. Chen, “Single-Loop Current Sensorless Control for Single-Phase Boost-Type SMR,” *IEEE Transactions on Power Electronics*, vol. 24, no. 1, pp. 163–171, Jan. 2009.

[88] H.-C. Chen, C.-C. Lin, and J.-Y. Liao, “Modified Single-Loop Current Sensorless Control for Single-Phase Boost-Type SMR With Distorted Input Voltage,” *IEEE Transactions on Power Electronics*, vol. 26, no. 5, pp. 1322–1328, May 2011.

[89] V. M. Lopez, F. J. Azcondo, F. J. Diaz, and A. de Castro, “Autotuning digital controller for current sensorless power factor corrector stage in continuous conduction mode,” in *2010 IEEE 12th Workshop on Control and Modeling for Power Electronics (COMPEL)*, 2010, pp. 1–8.

[90] D. Maksimovic and R. W. Erickson, “Nonlinear-carrier control for high-power-factor boost rectifiers,” *IEEE Transactions on Power Electronics*, vol. 11, no. 4, pp. 578–584, Jul. 1996.

[91] J. Rajagopalan, F. C. Lee, and P. Nora, “A general technique for derivation of average current mode control laws for single-phase power-factor-correction circuits without input voltage sensing,” *IEEE Transactions on Power Electronics*, vol. 14, no. 4, pp. 663–672, Jul. 1999.

APPENDIXES

Listing of PSIM simplified C block for driving half-bridge in rectifier mode

```
//Iavg
y1 = x1*( sin (314.16*(x2+1)/25000) + sin (314.16*x2/25000)  )/2 ;
y2 = 375;
if (( x4 - x3 ) > 0 )
      y2 = ( x4 - x3 );
y3=7031250000;
if ( ( 25000 * (x3+x5)  * (x4+x5) ) > 0 )
      y3=( 25000 * (x3+x5) * (x4+x5) );

y4 = ( sqrt ( y1 * 2 * 0.001 * y2  / y3  ) );
y2=375+375;
if ((x4+x5) > 0)
      y2=x4+x5;
//t1_bcm
y2 = ( x1*( sin(314.1593*(x2+1)/25000) - sin(314.1593*(x2)/25000) ) - (x3-
x4)/(0.001*25000)) / (y2/0.001) ;
//Ist(n+1)
y5 = x1* sin(314.16*(x2+1)/25000) - ( ((x3+x5)/0.001) - x1*( sin(314.1593*
(x2+2)/25000) - sin(314.1593*(x2+1)/25000 )  )*25000 )*( y2/2) ;
//Vc2+Vc1
y6=375+375;
if ((x4 + x5) > 0 )
      y6 =x4 + x5;
//Vc1-Vin
y3= (375 - 0)/(25000*25000*2*0.001);
if (( x4 -x3 ) !=  0 )
      y3 = ( x4 - x3 ) / ( 25000*25000*2*0.001 );
if      ((   y3   +   (y5/25000)   -   (x1*sin(314.1593*x2/25000)/25000)   -
2*(1/2/25000*(               x1*sin(314.1593*(x2+1)/25000)               -
x1*sin(314.1593*x2/25000)  ) ) ) > 0 ) {
y6 = sqrt( 2*0.001     *(y3+(y5/25000) - ( x1*sin(314.1593*x2/25000)/25000)
–2*(1/2/25000*(x1*sin(314.1593*(x2+1)/25000)-
x1*sin(314.1593*x2/25000))))/y6 );
}
y4 = min(y4,y6);
//deltaF
y3=(        (x3+x5)*y2/0.001    -    x1*(    sin(314.1593*(x2+1)/25000)    -
sin(314.1593*(x2)/25000)  ) *y2*25000   ) /2;

//Imax_ccm
y3= x1*sin(314.1593*(x2+1)/25000) + y3 + x1*( sin(314.1593*(x2+1)/25000) -
sin(314.1593*(x2)/25000)  )  *y2*25000 ;
x6=0;
y2=((t-0.00002-x6)/0.00004)-round( (t-0.00002-x6)/0.00004);
y2=(y2+0.5)*0.00004;
```

Listing of PSIM simplified C block for driving half-bridge in hysteresis control

```
//Iavg
y1 = x1*( sin (314.16*(x2+1)/25000) + sin (314.16*x2/25000)  )/2 ;
y2 = 375;
if (( x4 - x3 ) > 0 )
      y2 = ( x4 - x3 );
y3=7031250000;
if ( ( 25000 * (x3+x5)  * (x4+x5) ) > 0 )
      y3=( 25000 * (x3+x5) * (x4+x5) );
y4 = ( sqrt ( y1 * 2 * 0.001 * y2  / y3  ) );
y2=375+375;
if ((x4+x5) > 0)
      y2=x4+x5;
//t1_bcm
y2 = ( x1*( sin(314.1593*(x2+1)/25000) - sin(314.1593*(x2)/25000) ) - (x3-
x4)/(0.001*25000)) / (y2/0.001) ;
//Ist(n+1)
y5    =    x1*    sin(314.16*(x2+1)/25000)    -    (    ((x3+x5)/0.001)    -
x1*( sin(314.1593*(x2+2)/25000) –
      sin(314.1593*(x2+1)/25000)  )*25000 )*( y2/2) ;
//Vc2+Vc1
y6=375+375;
if ((x4 + x5) > 0 )
      y6 =x4 + x5;
//Vc1-Vin
y3= (375 - 0)/(25000*25000*2*0.001);
if (( x4 -x3 ) !=  0 )
      y3 = ( x4 - x3 ) / ( 25000*25000*2*0.001 );
if     (   (   y3   +   (y5/25000)   -   (x1*sin(314.1593*x2/25000)/25000)   -
2*(1/2/25000*( x1*sin(314.1593*(x2+1)/25000) –
      x1*sin(314.1593*x2/25000)  ) ) ) > 0 ) {
y6 = sqrt( 2*0.001      *(         y3         +         (y5/25000)         -
(x1*sin(314.1593*x2/25000)/25000)                                          -
2*(1/2/25000*(                x1*sin(314.1593*(x2+1)/25000)                -
x1*sin(314.1593*x2/25000)  ) ) )/ y6 );
}
y4 = min(y4,y6);//+0.000000105+x2/25000/25000/7);
//deltaF
y3=(        (x3+x5)*y2/0.001    -    x1*(    sin(314.1593*(x2+1)/25000)    -
sin(314.1593*(x2)/25000)  ) *y2*25000   ) /2;
//Imax_ccm
y3= x1*sin(314.1593*(x2+1)/25000) + y3 + x1*( sin(314.1593*(x2+1)/25000) -
sin(314.1593*(x2)/25000)  )  *y2*25000 ;
y1=x6;
if ( (x2<125) & (y5<0.0) ) y1=0;
if ( y5>0.0) y1=1;
if ( (x6>0.9)&(x6<1.1) & (y5<=0.001) & (x7<=0.001)) y1=t;
y2=((t-0.00002-1*(x6))/0.00004)-round( (t-0.00002-1*x6)/0.00004);
y2=(y2+0.5)*0.00004;
if (y5>0.0) y2=0.00004;
//if ((y1>0.5) & (x7>=0.00001)) y2=0.00004;
y7=0;
if ((x2>10) & ( x7 <= y5 )& (y5>0)) y7=1;
```

Appendix C

Listing of PSIM simplified C block for driving half-bridge in stand-alone inverter mode with numerical estimation of DCM control law

```
//Iavg
y1 = x1*( sin (314.159254*(x2+1)/25000) + sin (314.159254*x2/25000)  )/2 ;

//R
y3=311/abs(x1);

//Hold previous t_dcm
y5=x7;

//if new switching period
if (x2>(x6+0.5)) {
      y6=0;
      y7=0.00004;
      //Bisection method
      while(abs(y6-y7) > 0.00000001) {
            y5=exp(-
y3/0.001*(y6+y7)/2)*(1+x5/x4*exp(y3/0.001*((x4+x5)*(y6+y7)/2+y3/25000*y1)/x
5))-(1+x5/x4);
            y2=exp(-
y3/0.001*(y6))*(1+x5/x4*exp(y3/0.001*((x4+x5)*(y6)+y3/25000*y1)/x5))-
(1+x5/x4);
            if (y5*y2>0)  {
                  y6=(y6+y7)/2;
            }
            if (y5*y2<0){
                  y7=(y6+y7)/2;
            }
      }
      //t1_dcm
      y5=(y6+y7)/2;
}

if ( (x5>0) & (x4>0) ) {
      //t1_ccm
      y2      =      (      -x1*(      sin(314.159254*(x2+1)/25000)      -
sin(314.159254*(x2)/25000) )*0.001 + (x5 -y3*y1)/25000 ) / (x4 + x5) ;
}
//choose minimal of t_dcm and t_ccm
y4 = min (y5, y2);
//Hold previous switching period number
y3=x2;
```

Interconnection switch – Capture – Power scheme

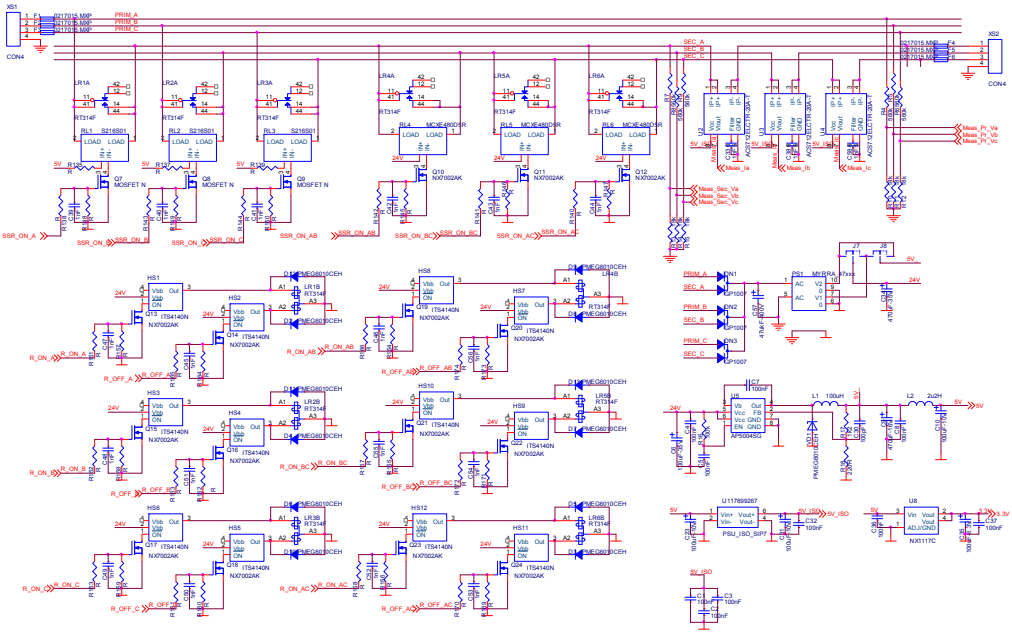

Interconnection switch – Capture – Control scheme

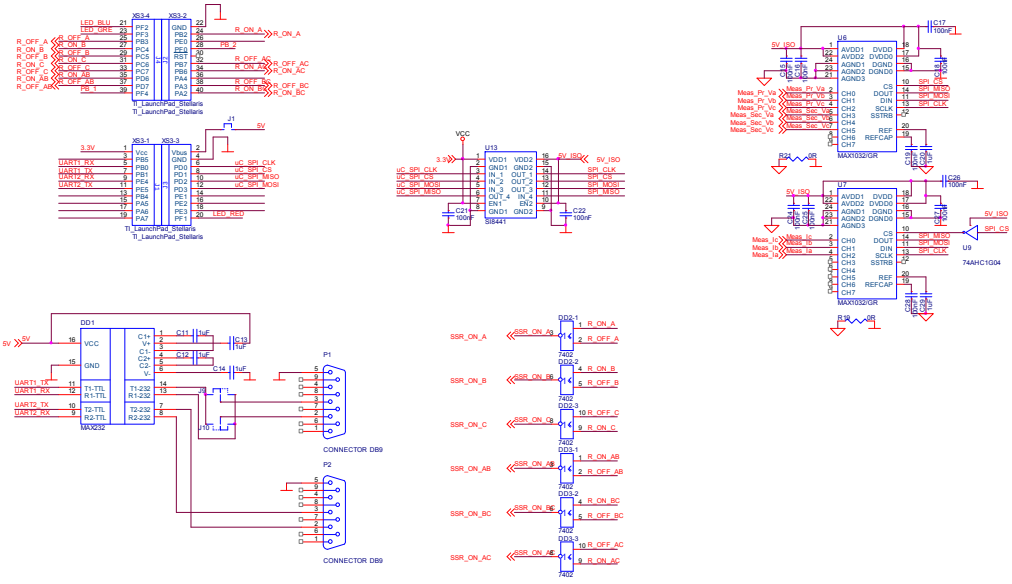

Interconnection switch – Layout - Top

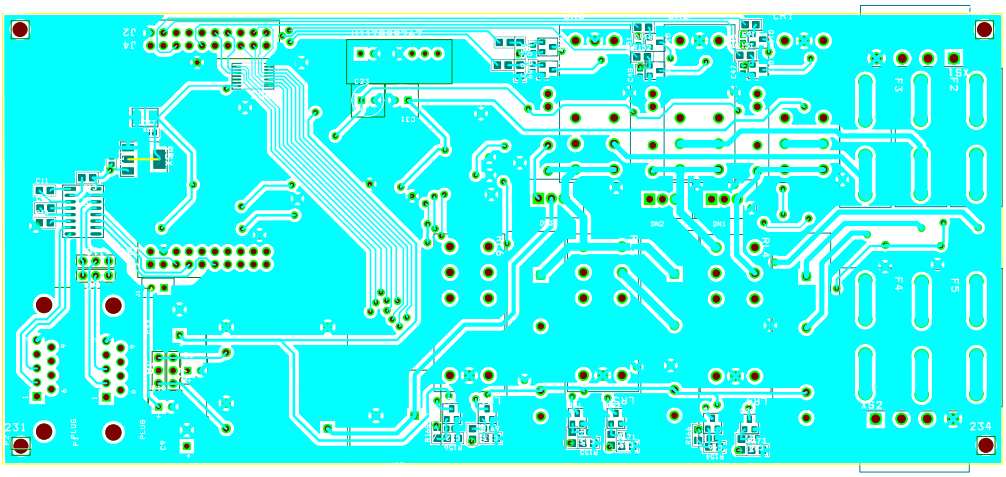

Interconnection switch – Layout – Bottom

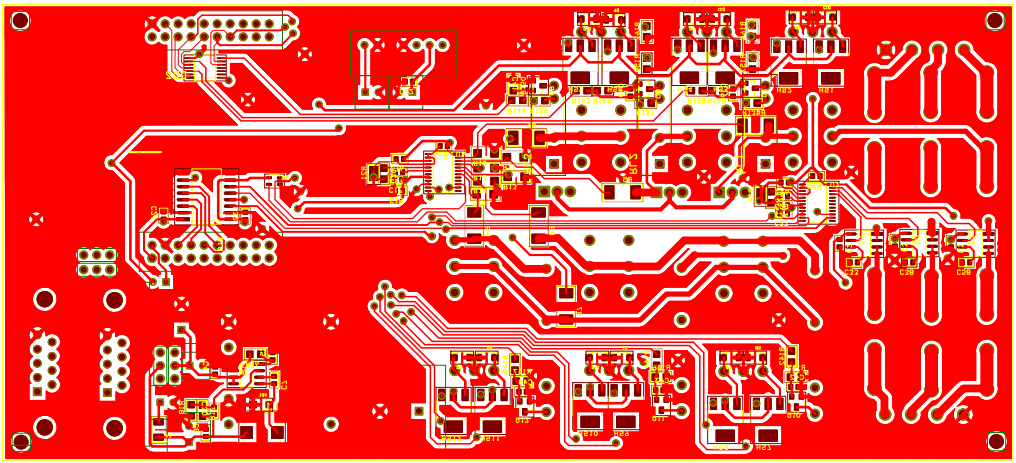

Communication node – Capture – Power scheme

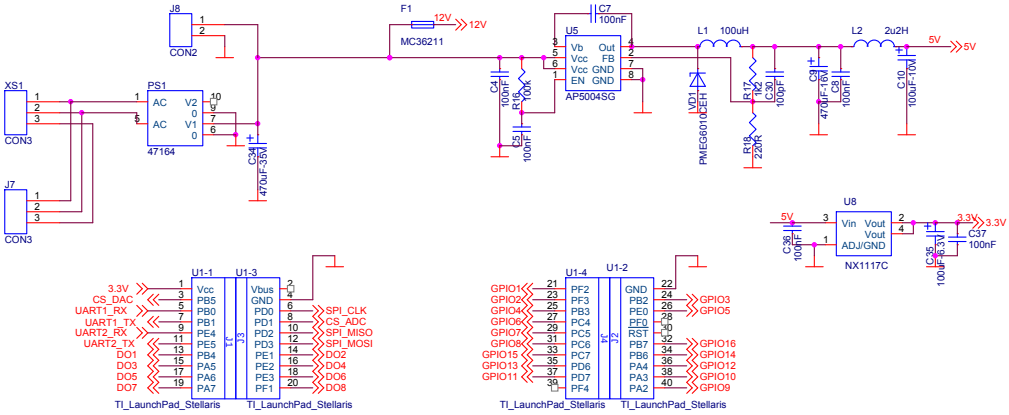

Communication node – Capture – IOs

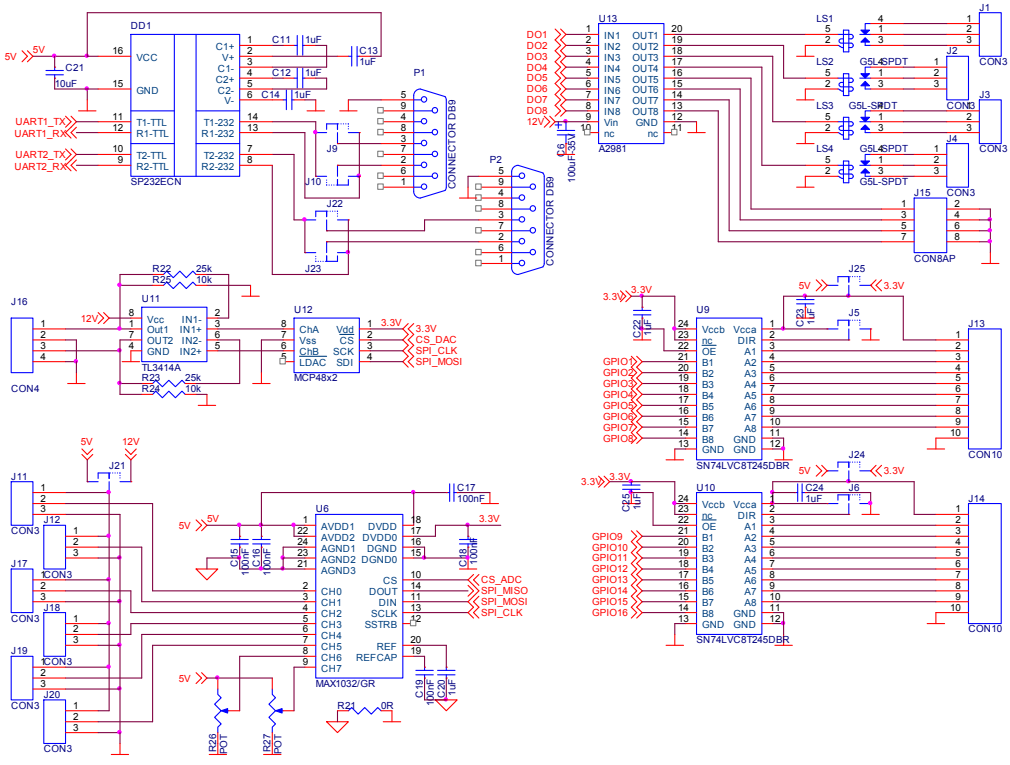

Communication node – Layout – Top

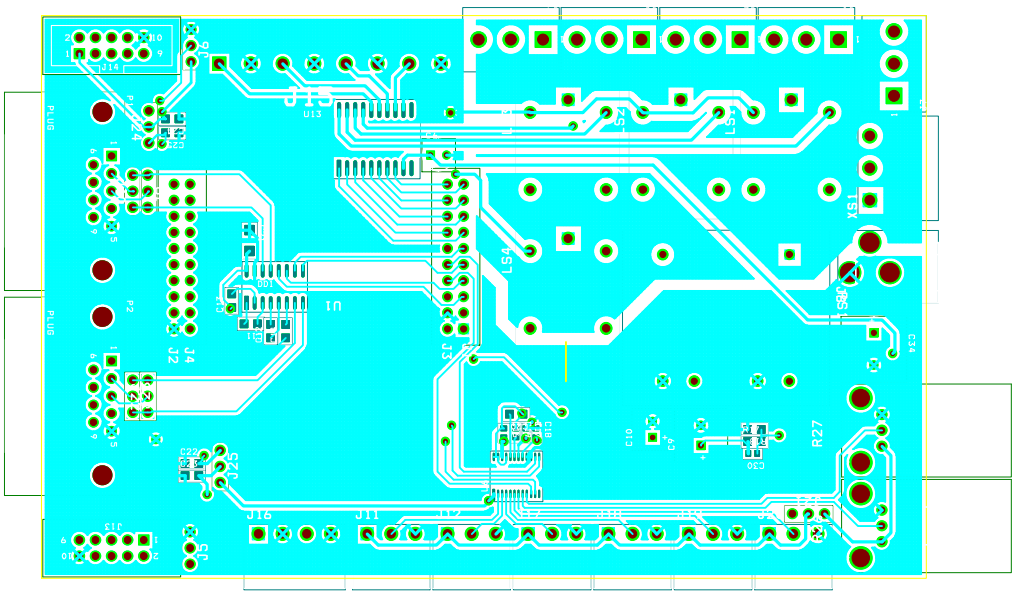

Communication node – Layout – Bottom

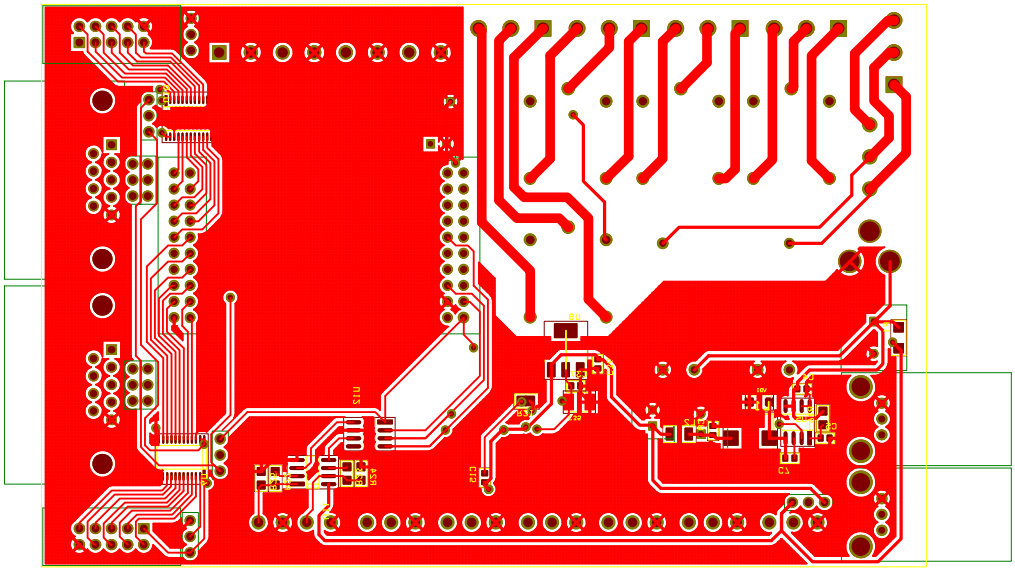

Bidirectional AC/DC converter – Capture - Power scheme

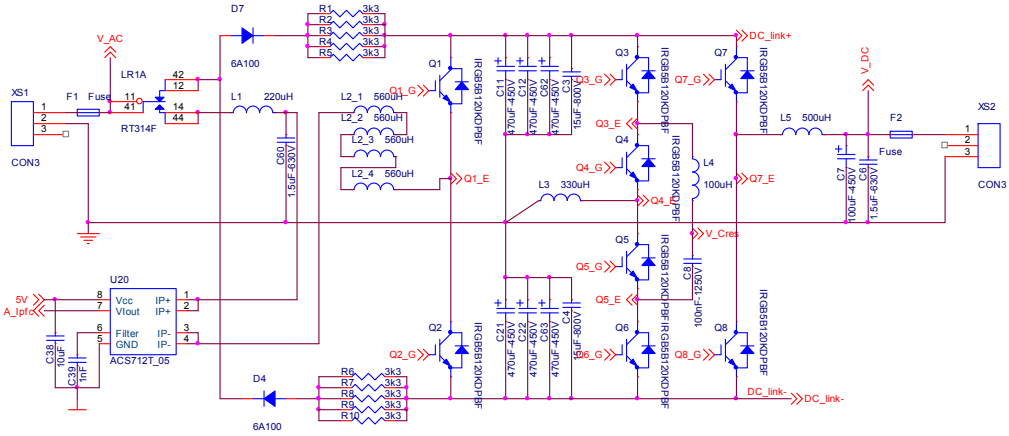

Bidirectional AC/DC converter – Layout - Top

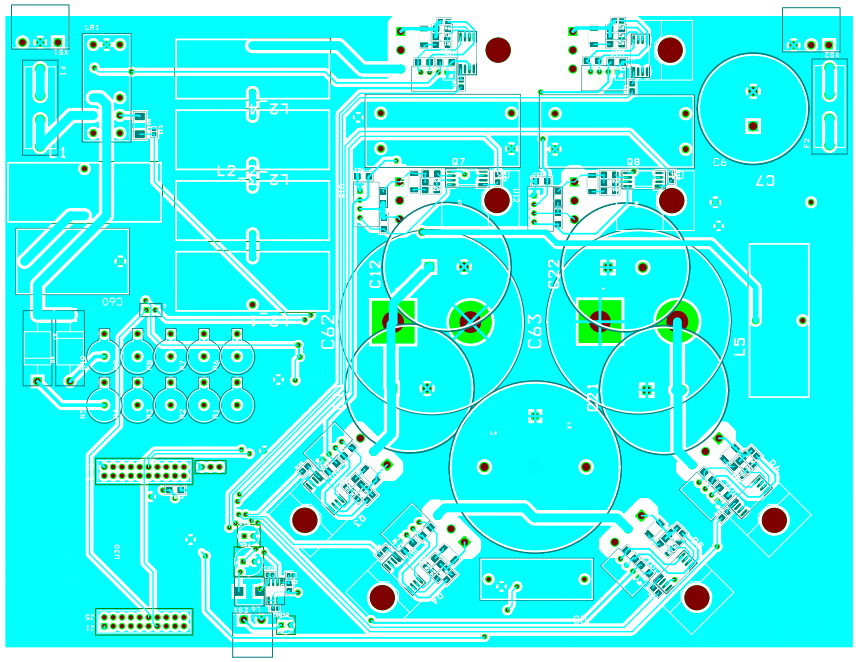

Bidirectional AC/DC converter –Layout - Bottom

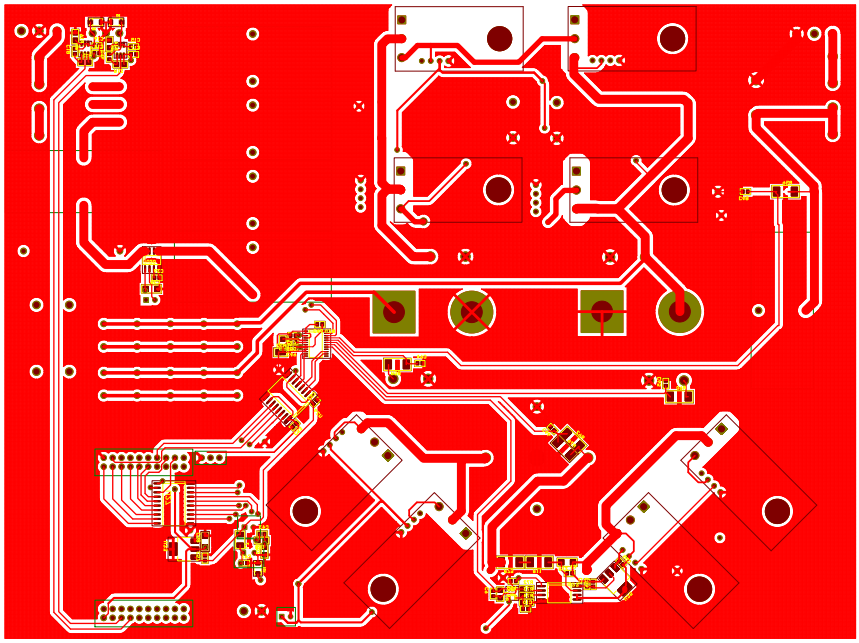

FPGA control board – Capture - Electrical scheme

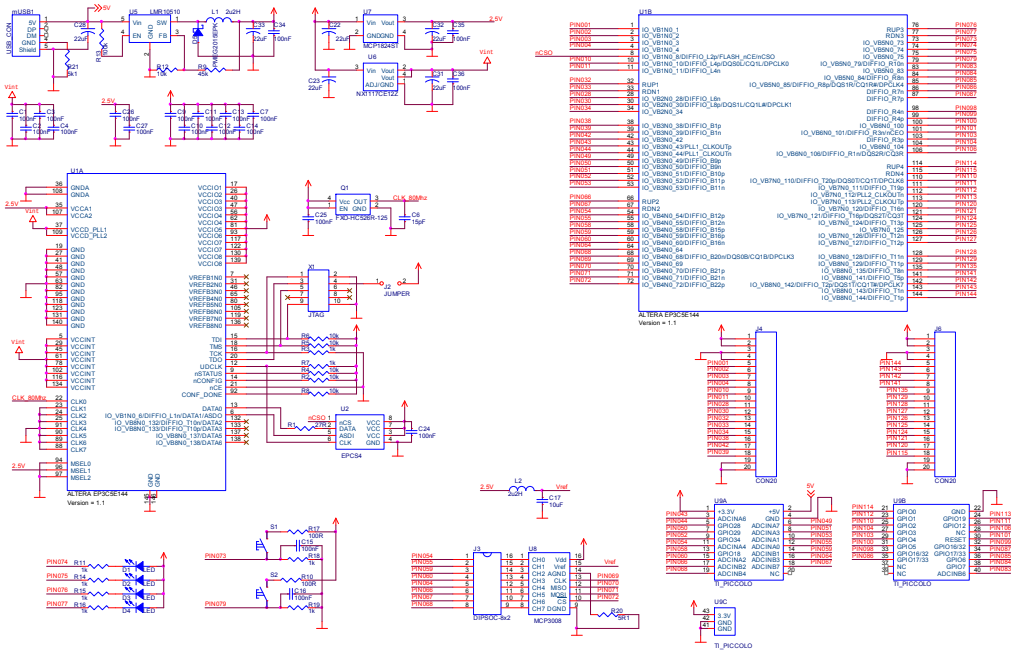

FPGA control board – Layout – Top

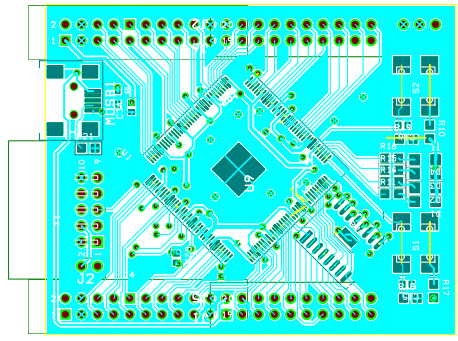

FPGA control board – Layout – Bottom

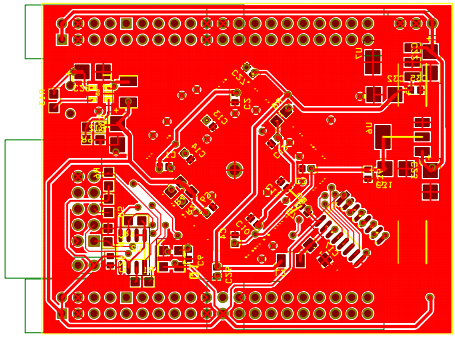

Appendix H

FPGA control board – Block diagram – Main control scheme

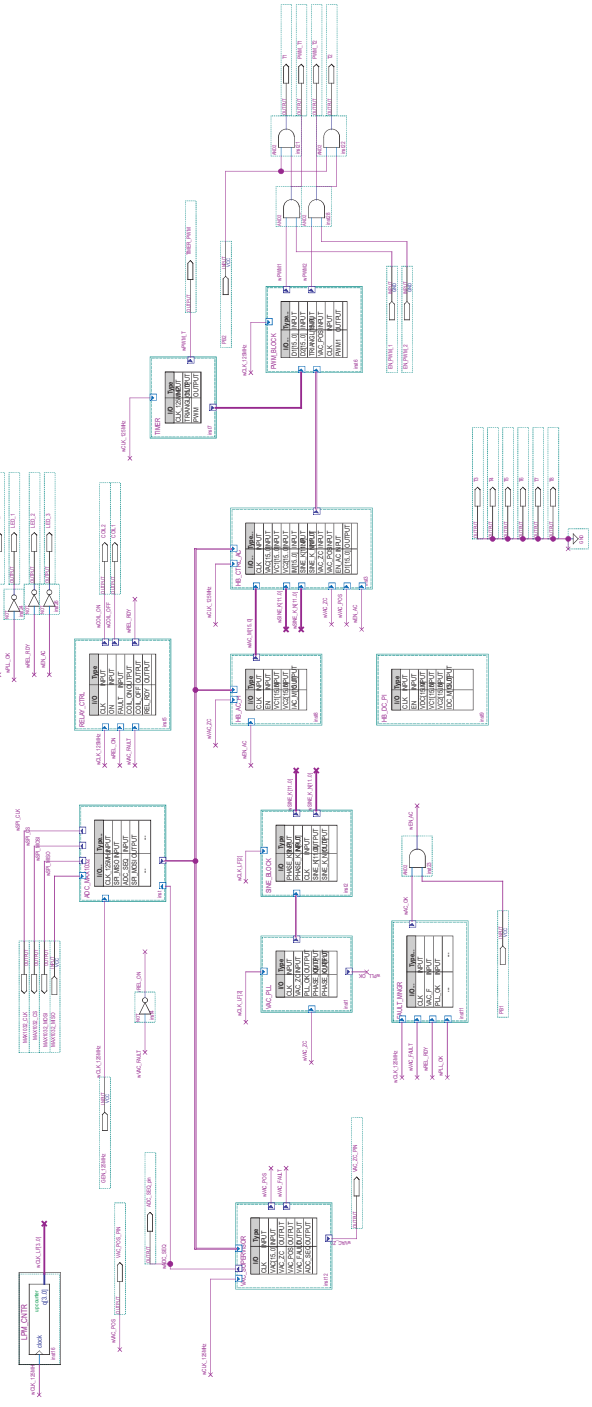

FPGA control board – Block diagram – Duty cycle calculation schematic